**FACULTY
OF MATHEMATICS
AND PHYSICS
Charles University**

MASTER THESIS

Bc. Václav Maixner

Development of Hydrogen Fuel Cells

Department of Surface and Plasma Science

Supervisor of the master thesis: prof. RNDr. Vladimír Matolín, DrSc.

Study programme: Physics of Surfaces and Ionized Media

Study branch: Physics of Surfaces and Interfaces

Prague 2020

I declare that I carried out this master thesis independently, and only with the cited sources, literature and other professional sources. It has not been used to obtain another or the same degree.

I understand that my work relates to the rights and obligations under the Act No. 121/2000 Sb., the Copyright Act, as amended, in particular the fact that the Charles University has the right to conclude a license agreement on the use of this work as a school work pursuant to Section 60 subsection 1 of the Copyright Act.

In Prague date 23. 7. 2020   Václav Maixner
                                                            Author's signature

Title: Development of Hydrogen Fuel Cells

Author: Bc. Václav Maixner

Department: Department of Surface and Plasma Science

Supervisor: prof. RNDr. Vladimír Matolín, DrSc., Department of Surface and Plasma Science

Abstract: Fuel cells are a popular power source, however, plagued by the problem of water management. To further investigate the performance of Nafion-like membranes in relation to water management, a novel system for humidity chamber electrochemical spectroscopy has been constructed and tested. The system allows for measurement of proton exchange membrane conductivity under well defined conditions, allowing for more insight into the behaviour of the membrane. Measurements of etched membranes have been performed, showing degradation of gold plated copper alloy electrodes caused by the etched membrane's surface. This behaviour has been hypothesised to arise from a formation of radicals due to the etching.

Keywords: Etched PEM Humidity chamber Water-management EIS

Contents

Introduction

When internal combustion engines became commercially widespread during the second half of 19th century, they brought a revolution with them. Instead of using human and animal labour, the chemical energy of petroleum and other fuels was converted in heat engines into mechanical movement or electricity. Since then the population boom caused us to realize, that using fossil fuels is not sustainable - both due to the limited amount and the impacts on the environment.

Thus there is a need to find a substitute for the heat engine. Batteries have recently had a strong progress in technology, resulting in viable cars driving around powered only by a battery stack. However batteries have several downsides, which make them non-viable for certain applications. One of these is low power density, making scaling with batteries non feasible after a certain point.

Recent advances it thin film catalysis has reintroduced an old technology in new light. Fuel cells have been around almost as long as heat engines. Their main strength being the conversion of chemical energy into electricity. Skipping the conversion of fuel into heat of heat engine cycle allows the fuel cell to achieve much higher efficiency, as well as much less harmful emissions.

Fuel cells enjoyed few spotlights throughout their history, most notably being used in NASA's space program. However, their extremely high price and low stability and low resistance to non-pure fuel hindered their commercial use. This has been vastly improved by recent advancements and renewed interest in this technology, partially thanks to the society looking for more environmentally responsible ways to power machines.

This progress has led to fuel cells being used in wide ranges of applications - from powering drones, cars, and trucks to serving as back-up power source for hospitals. Despite still being considered a young technology, fuel cells are able to compete with batteries and engines, even surpassing them in certain applications. Examples can be drones as described by González et al. [2014] or fuel cell electric vehicles with long driving range, as described by Gröger et al. [2015] and Ajanovic and Haas [2019]. Considering how fast modern fuel cells are able to push boundaries, it seems almost certain that fuel cells are going to overtake more roles of power source as the technology matures.

Fuel cells have 3 main areas of possible improvement that would ease their widespread commercial use: cost, performance, and stability. High cost comes from high price of components of fuel cells, especially the catalyst. Most of the modern catalysts use platinum, rare and expensive noble metal. Our research group focuses on this topic, with notable publications being Bruix et al. [2014] and Dvořák et al. [2016]. We try to mitigate the problem, creating thin catalyst layers, active nanostructures or using additives such as CeO_2 to lower the amount of Pt needed. These improvements might drive the cost of a fuel cell down or improve the performance, but the improved components have to be as stable as their predecessors. They have to be chemically stable long enough, resistant to impurities, and changes of operating conditions of the fuel cells.

To take a step back, the topic of this thesis is Development of Hydrogen Fuel Cells. This work started with testing fuel cells and improving the components they are constructed of. It soon became clear, that water management was the

biggest problem to solve when it came to performance improvement. This work therefore focuses mainly on water management and especially on the construction of a new measuring system and it's use in measuring proton exchange membranes under well defined conditions, which could yield new insights into the water balance's influence on membrane conductivity.
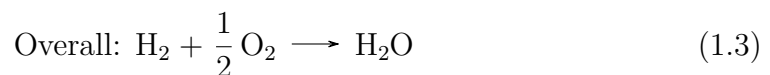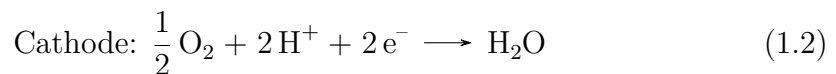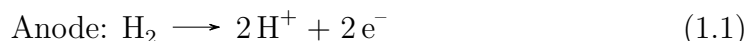
1. Theory

This work revolves around fuel cells. They were invented in 19th century, several decades after electrolysis (Andújar and Segura [2009]). Fuel cell can be thought of as a reversed process to electrolysis - recombining the elements split by electrical current in order to produce electric current. There are many types of modern fuel cells, however they share common underlying principle - fuel is brought to a catalyst at anode, where it gives off electrons. These electrons travel via outer circuit, supplying the connected load, while the rest of fuel travels through a medium to cathode. There it recombines with the relegated electron and the supplied oxidants.

In its principle, fuel cell can be thought of as a hybrid between a battery and a heat engine. Same as the battery, fuel cell relies on electrochemical process to create current, resulting in high efficiency due to it being a one-step process. However, battery stores its energy within itself, meaning once its depleted, it either has to be replaced, or charged. Fuel cell are only energy conversion devices, meaning they have an external reservoir of fuel, same as heat engines. This makes their refuelling fast, when compared to batteries. Fuel cells thus share some of good qualities of both worlds: high efficiency of batteries and fast refueling of heat engines.

1.1 Hydrogen fuel cells

One of the most popular designs of fuel cells is the hydrogen fuel cell. It uses hydrogen as the fuel and oxygen on the cathode side. The reaction then looks like this (Qi [2013]):

$$\text{Anode: } H_2 \longrightarrow 2\,H^+ + 2\,e^- \tag{1.1}$$

$$\text{Cathode: } \frac{1}{2}\,O_2 + 2\,H^+ + 2\,e^- \longrightarrow H_2O \tag{1.2}$$

$$\text{Overall: } H_2 + \frac{1}{2}\,O_2 \longrightarrow H_2O \tag{1.3}$$

The process in the context of the fuel cell can be seen in Figure 1.1. Here, hydrogen enters the anode side, reacts on catalyst and gives up electrons. These travel to a load via the external circuit. The hydrogen ion travels through the electrolyte to the cathode, reacting with the oxygen brought to the cathode side and the electron, creating water. From this we can see another advantage of fuel cells over heat engine - the main by-products are water and heat.

On the diagram we can also see the symmetrical, sandwich structure of a fuel cell. The individual components are assembled and then pressed together to create a single fuel cell. First, the cell is enclosed in base plates, which serve to press the cell together and keep a tight seal, so that the gases used as fuel do not leak easily. Then we have collector plates, used to collect current of the whole
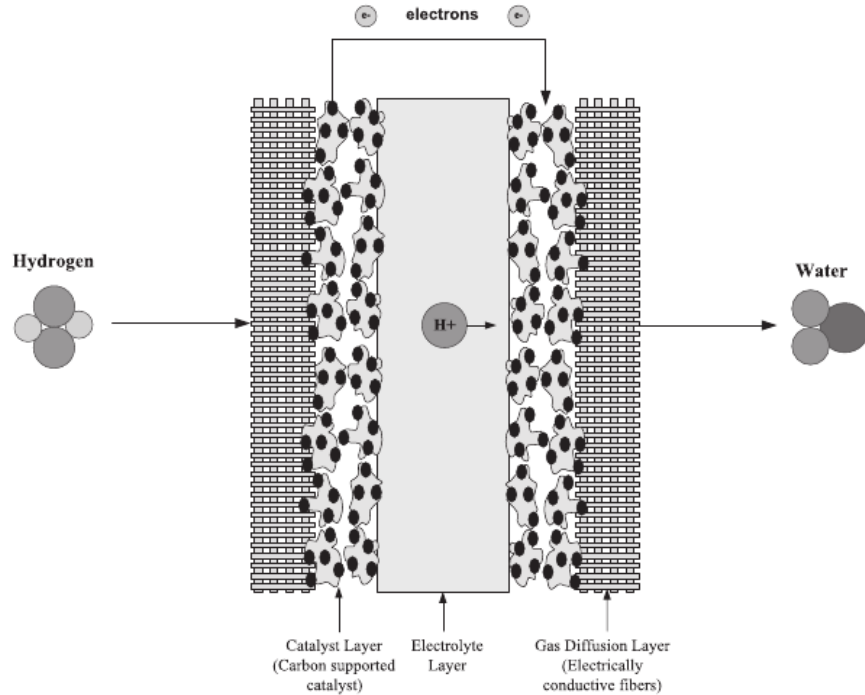
Figure 1.1: Hydrogen fuel cell diagram

cell - this is where we connect our external load. Next are the flow fields. These ensure that the gases are brought to the whole surface area of the catalyst, in order to best use the surface.

After the flow field is the gas diffusion layer (GDL) - usually a very porous material with high surface area, used to distribute the gases uniformly to the catalyst layer, where the reactions occur. The catalyst layer is sandwiched next to the heart of the fuel cell - the membrane. Called proton exchange membrane (PEM), it allows protons to travel from anode to cathode, whilst being a poor electron conductor - thus preventing major shorting across the membrane. The last 3 components described in this paragraph (GDL, catalyst, PEM) are collectively called the membrane electrode assembly (MEA). A single fuel cell has too low a voltage for most uses. The solution is to create a sandwich structure of many fuel cells connected in series, called a fuel cell stack.

1.2   Thermodynamics and kinetics

One of the reasons fuel cells are so appealing is their high efficiency. Let's investigate its efficiency and how we can describe the processes going on inside a fuel cell. Since fuel cell is a purely electrochemical process, we start by the definition equation of efficiency:

$$\mu = \frac{W_{out}}{W_{in}}, \tag{1.4}$$

where W_{out} is the work done by the system and W_{in} work supplied into the system. The work done by the system is the actual electrical energy produced,

which is equal to the change in Gibbs energy. The work supplied into the system is the maximum energy available from the fuel - in this case it is the higher heating value (HHV) of hydrogen. HHV is the heat produced by combustion of the fuel after it returns to 25 °C (this is called lower heating value - LHV) plus the latent heat from vaporization. It can be seen that HHV corresponds to water in liquid form, whilst LHV corresponds to water in gaseous form.

When we use the values provided by Qi [2013] of $\Delta H_{gas}^0 = -241.8\,\text{kJ}\,\text{mol}^{-1}$ and $\Delta G_{gas}^0 = -228.6\,\text{kJ}\,\text{mol}^{-1}$ for gaseous form (LHV) and $\Delta H_{liq}^0 = -285.8\,\text{kJ}\,\text{mol}^{-1}$ and $\Delta G_{liq}^0 = -237.1\,\text{kJ}\,\text{mol}^{-1}$ for liquid form (HHV), we get the corresponding efficiency as:

$$\mu_{gas} = \frac{\Delta G_{gas}^0}{\Delta H_{gas}^0} = \frac{-228.6}{-241.8} \approx 94.5\,\% \tag{1.5}$$

for efficiency of a fuel cell operating with water vapour and

$$\mu_{liq} = \frac{\Delta G_{liq}^0}{\Delta H_{liq}^0} = \frac{-237.1}{-285.8} \approx 83.0\,\% \tag{1.6}$$

for efficiency of a fuel cell operating with water in liquid form. Despite the fact that PEMFCs usually operate at temperatures below the 100 °C mark, the LHV value of efficiency is usually used, since the water formed at the cathode is in gaseous form and, if the stack operates well, mostly should not condense and leave the stack with the other gases. We can see that the theoretical efficiency of a fuel cell is very high, especially when compared to Carnot's cycle.

Next we review the potential of the fuel cell. The upper limit value of voltage can be deduced using simple thermodynamic definitions. We take the definition of electrical work W_{el}:

$$W_{el} = QE\,, \tag{1.7}$$

where Q is the charge moved in electrical field E. H_2 provides 2 electrons to the reaction and relates to charge per mole of H_2 by the Faraday constant F. We also realize that the work done by the system is by definition equal to the change in Gibbs free energy. When we use the standard of minus sign being assigned to work being done by the system, this yields:

$$\Delta G = -2FE\,. \tag{1.8}$$

If we consider standard temperature of 25 °C, substitute in values from above for ΔG_{liq}^0, and rearrange the equation, we get:

$$E_{liq} = -\frac{\Delta G_{liq}^0}{2F} = 1.23\,\text{V}\,. \tag{1.9}$$

In the same way, if we use ΔG_{gas}^0, we get $E_{gas} = 1.18\,\text{V}$. This value is called thermodynamic voltage and describes the relation between the two half reactions taking place on electrodes.

1.3 Fuel cell operation

The actual voltage of the cell can be vastly different from the theoretical value. One the main reasons for fuel cell output variability are its operating parameters. Changing of the operating parameters is a way of controlling the power output and the situation inside the fuel cell.

The operating parameters we can change are those of the gases supplied as fuel. The PEMFC, whether in testing setting or in real life use, is being supplied hydrogen and air/oxygen. The power output of the fuel cell depends on the following parameters of the supplied gases:

1. Temperature

2. Relative humidity

3. Stoichiometric ratio

4. Pressure

Well set parameters can lead to high and stable power output, whilst suboptimal parameters can lead to drastic decreases in performance and decrease of the fuel cell's lifetime. On top of these, the fuel cell's performance depends on it's physical structure. Mainly the shape of flow fields, which if sub-optimal, can lead to accumulation of water.

1.4 Relative humidity

This work revolves around water management and water vapour. In this section, the term relative humidity and other used in this work will be explored. The following equations are taken from Lide [2003] and Rotronic [2005]. In the temperature range from 25 °C to 80 °C, water vapour acts as an ideal gas, thus ideal gas law applies:

$$pV = nRT \,, \tag{1.10}$$

where p is pressure, V volume, and T temperature of the gas. n denotes number of moles of the glass and R is the molar gas constant. If we have gas composed of more components, we describe the component x by it's partial pressure p_x. Partial pressure of component x of a gas with total pressure p_t is defined as

$$p_x = p_t n_x \,, \tag{1.11}$$

where n_x is the mole fraction of gas component x, defined as number of moles of x divided by the number of all moles of the gas. Dalton's law states that the total pressure of a gas is a sum of partial pressures of all it's components:

$$p_t = p_1 n_1 + p_2 n_2 + ... + p_N n_N \,, \tag{1.12}$$

for $n \in \mathbb{N}$ number of components. Partial pressure can be thought of as the pressure of the gas component if it were to occupy the volume alone. In our work,

partial pressure of water vapour will be important to us. We can imagine the source of water vapour pressure inside a system coming from a droplet of water. The molecules in the water droplet have non-zero kinetic energy, which results in their evaporation into the surrounding gas. The reversed process is condensation, as in water molecules from the gas bump into the liquid droplet and stay there.

When the rate of evaporation and condensation is equal, the system is said to have achieved equilibrium vapour pressure. The equilibrium is designated by the inter-molecular forces and temperature. Higher temperature means higher kinetic energy and therefore higher rate of evaporation. Water vapour pressure depends strongly on temperature, as can be seen in Figure 1.2. The higher the curve, the more water vapour is in the gas. In order to prevent such formulations, let's define relative humidity.

Relative humidity RH is defined as:

$$RH[\%] = \frac{p_x}{p_s} \cdot 100\%\,, \tag{1.13}$$

where p_x is the partial pressure of water vapor in the gas and p_s the saturation pressure of water vapour in the gas at given temperature. Saturation pressure is the highest possible partial pressure of a component in a gas, meaning that at given temperature, the gas can hold no more of the component. The temperature to which the gas has to be cooled in order to achieve saturation pressure, is called the dew point. If the gas is cooled beyond the dew point, water starts to condense. Now we can say that the curves in Figure 1.2 respond to different levels of relative humidity (RH).

There are multiple empirical equations describing dependence of saturated water vapour pressure on temperature. For our range of temperature from 30 °C to 100 °C, the Arden-Buck equation is suitable. The equation, as described in Buck [1981], for saturation water pressure P_s is as follows:

$$P_s(T) = 6.1121 \exp\left[\left(18.678 - \frac{T}{234.5}\right)\left(\frac{T}{257.14 + T}\right)\right]\,, \tag{1.14}$$

where T is air temperature in °C. It has been shown by Dalton [1802] that vapour pressure is independent of the choice of gas.

1.5 Water management

We have talked about the problem of accumulating water inside the fuel cell. This problem falls into water management. The hydrogen fuel cell produces water itself and is supplied water via humidified reactants, either air or hydrogen, or both. If the stack doesn't have enough water, it dries up and if it has too much water, it floods. The target is to achieve water balance - a state in which there is enough water for the fuel cell to achieve high performance, whilst not blocking reactants.

In a stack, there are two sources of water: the incoming flow of humidified reactants and the water produced by the reaction 1.3. Reactants are humidified since the stack needs water to function properly. In our setting, the creation of water by the stack itself would not be enough to compensate for the drying out if non-humidified reactants would be used. The reactants are humidified by passing through a bubbler - a cylinder filled with water through which the gas is bubbled.
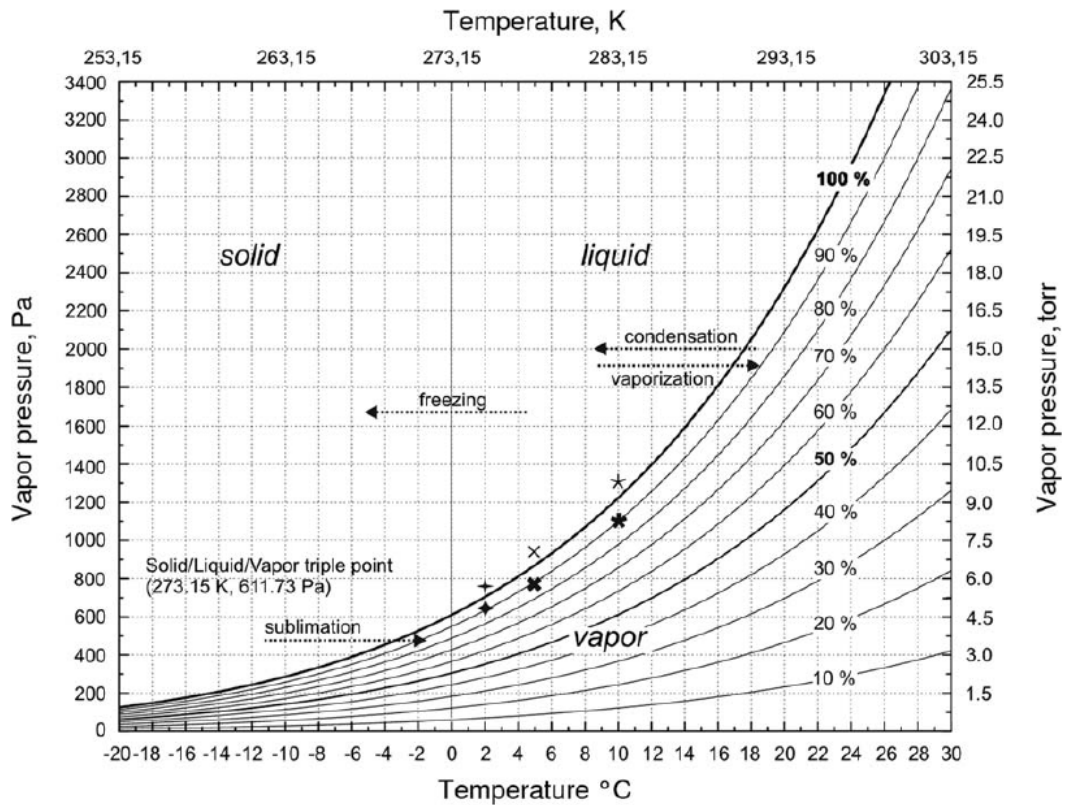
Figure 1.2: Water vapor pressure dependence on temperature and relative humidity from Nedela et al. [2015].

The bubbler can be heated to a defined temperature, resulting in different levels of relative humidity.

In the fuel cell itself, water is created at the cathode. Due to concentration gradient, the water will transport through the PEM to the anode side, resulting in transport of water from cathode to anode. This phenomenon is strengthened by the humidified air coming to cathode, since in usual fuel cell applications, larger flow of air is used, resulting in higher amount of water coming to cathode.

There is another contribution of water molecules movement across PEM. The membrane itself is proton conductive and the protons travel from anode to cathode, driven by the potential difference between electrodes. Inside the membrane there are pores with free volumes of water. The overall negative charge of membrane and molecules creates an electric double layer (EDL). The protons in EDL are then driven by Coulomb force due to the potential difference. This movement of protons causes bulk motion of water inside the pores caused by viscous drag (momentum transfer) as described by Wiley and Fimbres Weihs [2015] and schematically shown in Figure 1.3.

This drag is called the electroosmotic drag and it's magnitude is dependent on the hydration level of the membrane, with higher water content allowing for each proton to drag more water molecules. Proton conductivity inside membranes will be examined in further details in the following chapters. The last contribution to water displacement is purely mechanical - as the gases travel through flow fields, they can push droplets of water along the direction of gas flow. This can prevent accumulation of water at cathode side, if flows are high enough, and there is not
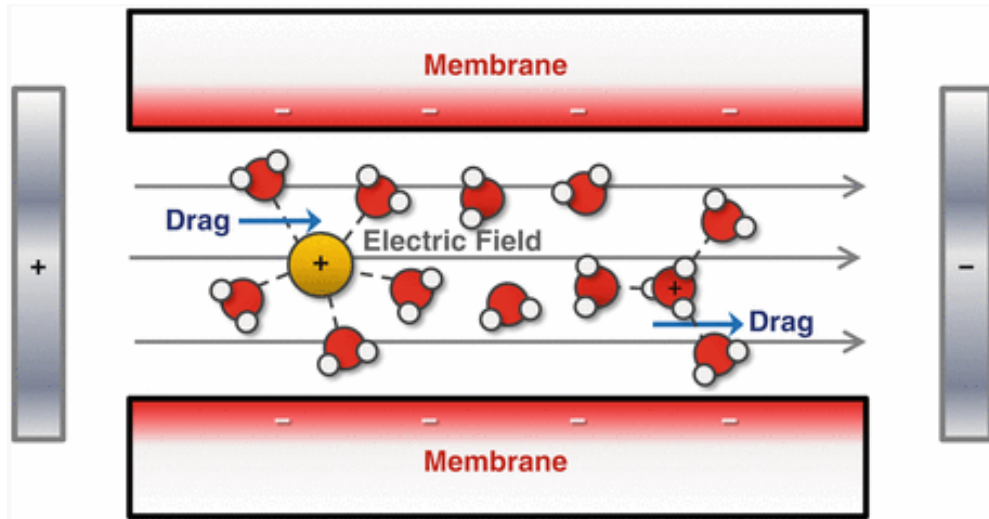
Figure 1.3: Schematic representation of electroosmotic drag of water molecules in a membrane pore, from Wiley and Fimbres Weihs [2015].

too much water.

If water balance is not achieved, two extremes can take place inside the fuel cell. First is membrane drying. Since the membrane needs to be humidified to conduct protons, lack of water leads to performance drop due to higher resistance. If the membrane is left dry for a longer period of time, it can lead to irreversible damage in the membrane performance, as shown by Canut et al. [2006]. Short-term exposure to dry environment may be reversible, as shown by Sone [1996]. Li and Pickup [2003] have shown that drying leads to shrinking of the pores, resulting in lower back diffusion rates, further worsening the membrane's performance.

The second extreme is fuel cell flooding. When too much water accumulates, usually at the cathode side, the reactants can't reach the electrode fast enough to supply the chemical reaction. This is called reactant starvation and is visible in the fuel cell's lowered potential. Flooding is typical for high current density operation and the cathode region, however it can happen at low current density operation, as shown by Schmittinger and Vahidi [2008] and can can also affect anode.

1.6 Membrane

Vital component of the fuel cell is the membrane. It serves 3 purposes:

- Conducting protons

- Electrons insulator

- Separating reactant gases

The industrial standard nowadays is Nafion from DuPont. It is a solid polymer with a Teflon main chain and a side chain containing a sulfonic acid group $-SO_3H$. Proton conductivity arises from these acidic groups and is the main parameter used to rate the quality of the membrane. For the membrane to be conductive, it

needs water and generally, the more water it has, the higher conductivity it can achieve.

The electron insulation arises from the negative charge of $-SO_3^-$ groups, causing electrons to be repelled from the membrane. Apart from electrochemical properties, we also require the membrane to be mechanically stable. Mechanical stability is usually described by 2 parameters of membrane - it's thickness and equivalent weight (EW). EW is defined as mass of the polymer repeating units per 1 mole of active site (in our case the $-SO_3H$ group). Higher value means more mechanically stable membrane with lower conductivity, lower EW yields higher conductivity and lower mechanical strength. Since these membranes are to be used in real life in fuel cells, there exists a certain threshold of strength required, since their damage usually results in permanent decrease of the fuel cell's performance.

Another factor is the thickness of the membrane. Due to the sandwich structure, thinner membrane means shorter mean path for protons, thus yielding lower resistivity. It also means faster rate of hydration, allowing for faster start-up of the system. Exception might be systems, where we want the membrane to be able to retain humidity to bridge short-term shortage of water supply. Generally thinner membranes have better performance, but we are again limited by their mechanical properties. This has been shown by modelling, with Gimba et al. [2016] accrediting worse performance to the rise of ohmic resistance and Kahroba et al. [2009] further claiming worse performance in the high current operating region.

1.7   Ionic conductivity of membranes

Membranes are good proton, or ionic conductors. Ionic conduction quite differs from electronic conduction. In metal, there is a low energy barrier for valence electrons to detach from the atom and move freely in the metal. Ions are, however, much heavier than electrons and thus less mobile. Their movement is more comparable to hopping motion in a lattice, where the lattice points are occupied by ions. This is especially true for solid state electrolytes, such as membranes. The hopping rate can by described by the material's diffusivity D[1]:

$$D = D_0 \exp(\frac{-\Delta G_{act}}{RT}),\qquad(1.15)$$

where D_0 is the hopping frequency constant, ΔG_{act} the activation energy barrier for one hop, R the universal gas constant, and T the temperature. Ionic mobility μ_i is described by Einstein relation:

$$\mu_i = \frac{q}{RT}D,\qquad(1.16)$$

where q is the charge of the ion, R the universal gas constant, T the temperature and D ionic diffusivity. Next, we describe the equation for conductivity of

---

[1]This section draws heavily from O'Hayre et al. [2016], which I found to be a very concise description of ionic conductivity in membranes and wholly recommend it for further reading.

charged particles σ:

$$\sigma_i = (|z_i|\, F) c_i \mu_i \,, \tag{1.17}$$

where z_i is the charge of the carrier, F the Faraday constant, c_i the molar concentration of ions. If we substitute the mobility μ_i from Equation 1.16 and consider that $q = |z_i|\, F$, we get for proton conductivity:

$$\sigma_i = \frac{(|z_i|\, F)^2 c_i D}{RT} \,, \tag{1.18}$$

Now substituting for diffusivity the expression 1.15 for hopping motion, we arrive at:

$$\sigma_i T = A_0 \exp\left(- \frac{E_a}{kT} \right), \tag{1.19}$$

where A_0 is the preexponential factor, E_a the activation energy per one atom ($E_a = \Delta G / F$) and k the Boltzmann constant. This equation holds well for polymer ion conductors, where hopping is the dominant means of proton conductivity.

1.8 Proton conduction mechanisms

If we look at the actual process of proton conductivity, we can start with 2 models. These describe the proton movements in a medium such as PEM. They are the Grotthuss mechanism (also known as "proton hopping mechanism", described above) and the Diffusion mechanism (also known as "vehicular mechanism"). In the Grotthuss mechanism, protons hop between $SO_3^-H_3O^+$ sites, due to vibrations of the Nafion backbone. The travel is accompanied by creation and breaking of hydrogen bonds (Zuo et al. [2012]).

In the diffusion mechanism, protons are dragged through the membrane by water molecules. The water serves as a "vehicle", bonding with the proton and forming H_3O^+. The proton moves due to the diffusion of its carrier. This was proposed by Kreuer et al. [1982] to explain ion exchanges with no proton transfer. Due to its nature, it is dependent on free water movement. This is achieved in Nafion thanks to its hydrophobic (perfluorinated) backbone and hydrophylic sulfonic acid side chains. This leads to separation between hydrophobic and hydrophilic domains with the sulfonic terminal groups forming well connected clusters and the hydrophobic domains giving them morphological stability. These hydrophylic domains can be imagined as pores of well connected sulfonic groups, allowing the water molecules to move freely across them. These pores contain local domains of water that in first approximation behave as bulk water and so the theory of proton conductivity from Kreuer [2000] in bulk water can be used.

In water, the dominant intermolecular interaction comes from hydrogen bonds. Introduction of extra protons into this system can be thought of as defects in the system. As these protons bond with water molecules, the bond energy of H_2O molecules around these defects is weakened. This decrease of energy barrier results in a more volatile system, with water molecules more prone to creating more complicated bonding structures and bonds quickly breaking and reforming. As a result, the extra protons form mostly 2 structures with water molecules, described by Eikerling et al. [2002]:
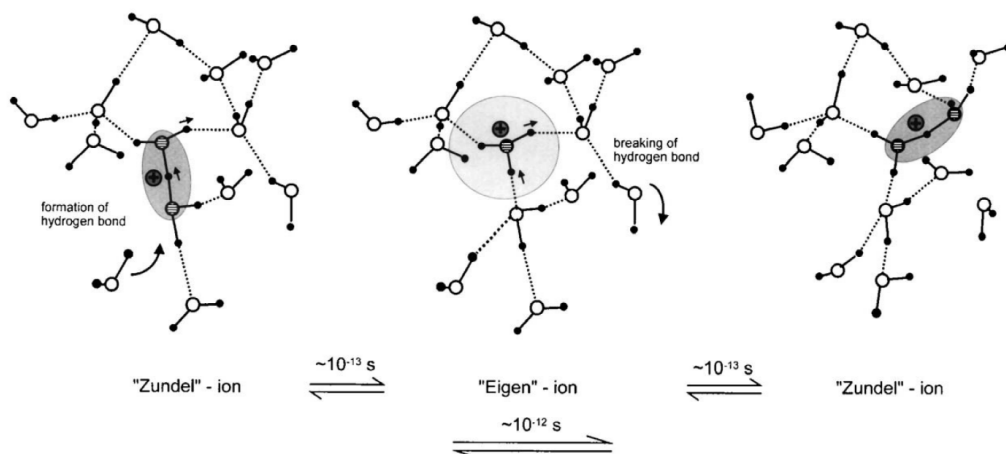
Figure 1.4: Diagram of water oscillating between Zundel and Eigen states by Kreuer [2000]. Areas of shortened bond length are shaded.

$H_5O_2^+$ (Zundel ion) The extra proton is in a shallow energy well between the two oxygen atoms.

$H_9O_4^+$ (Eigen ion) This cluster consists of one H_3O^+ molecule and 3 other H_2O molecules attached to each of the protons of H_3O^+.

Both of these structures have comparable probability of appearance in water and water molecules often quickly oscillate between them. A simple explanation of how the proton transfers has been described by Eikerling et al. [2002]: the positively charged molecule (donor) "polarizes" the neighbouring molecule to conform to its orientation. Let's imagine the H_3O^+ molecule and H_2O molecule close to it. Then the interaction would see them forming temporarily a Zundel ion and via molecular fluctuations transferring the proton through the low energy barrier $O-O$ bond.

However it has been shown by the authors that the H_3O^+ is less stable than the Zundel and Eigen ion, thus leaving this as a rather simplistic approach. The authors then describe the same approach of donor-acceptor pairs exchanging the extra proton via molecular fluctuations. In the case of $H_5O_2^+$ clusters, the authors describe this as the donor $H_5O_2^+$ forcing surrounding water to form the same cluster with the H_3O^+ of the original $H_5O_2^+$ molecule. The proton then usually transfers by oscillating between the Zundel and Eigen ion, which can be seen in Figure 1.4.

The take away message here is that Nafion provides mechanical strength and allows the H^+ to dissociate from its sulfonic group. These H^+ ions form aqueous complexes, which travel in free volumes of water in the membrane's pores as in bulk water. This mechanism is further enhanced by hydrophobicity of the backbone. The ions can also travel due to structural vibrations, however, the vehicular mechanism is dominant for Nafion-like membranes, especially at high membrane humidification.
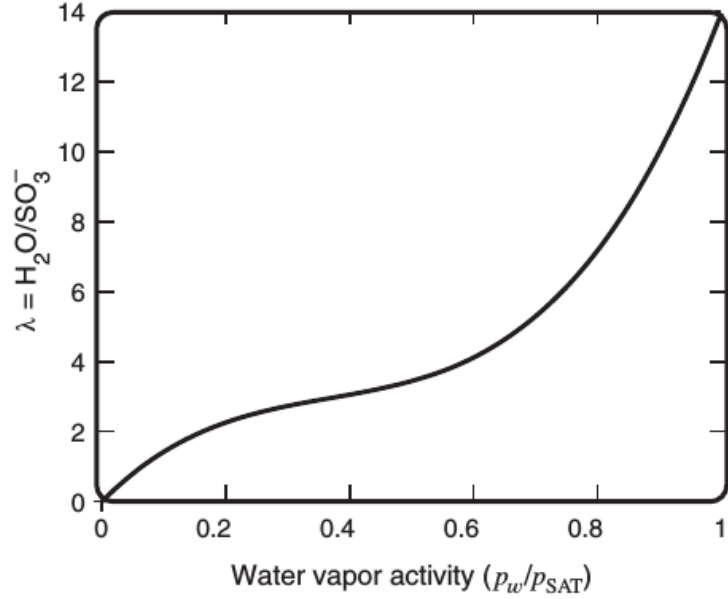
Figure 1.5: Dependence of water content of Nafion on water activity (from O'Hayre et al. [2016]).

1.9 Nafion conductivity

The aforementioned proton conductivity mechanism is highly dependent on the water content of the membrane. Nafion behaviour can be approximated as that of a solution electrolyte, if the membrane is well hydrated. Water content λ of Nafion is described as:

$$\lambda = \frac{n_{\text{water molecules}}}{n_{\text{number of SO}_3^-\text{H}^+ \text{ sites}}}. \tag{1.20}$$

The values of λ can range from $\lambda = 0$ (completely dry) to $\lambda = 22$ (fully hydrated). O'Hayre et al. [2016] describes the conductivity dependence using water vapor activity a_w, defined as

$$a_w = \frac{p_w}{p_{sat}}, \tag{1.21}$$

where p_w is the partial pressure of water and p_{sat} the saturation water pressure at given temperature. When compared to Lide [2003], we can see that this definition is equivalent to that of relative humidity sans the percentage conversion. Relationship between λ and a_w is described in O'Hayre et al. [2016] as:

$$\lambda = \begin{cases} 0.043 + 17.18a_w - 39.85a_w^2 + 36.0a_w^3 & \text{for } 0 < a_w \leq 1, \\ 14 + 4(a_w - 1) & \text{for } 1 < a_w \leq 3. \end{cases} \tag{1.22}$$

This equation doesn't include temperature dependence, it is accurate for temperatures near 80 °C. The same dependence has been reported by Sone [1996],
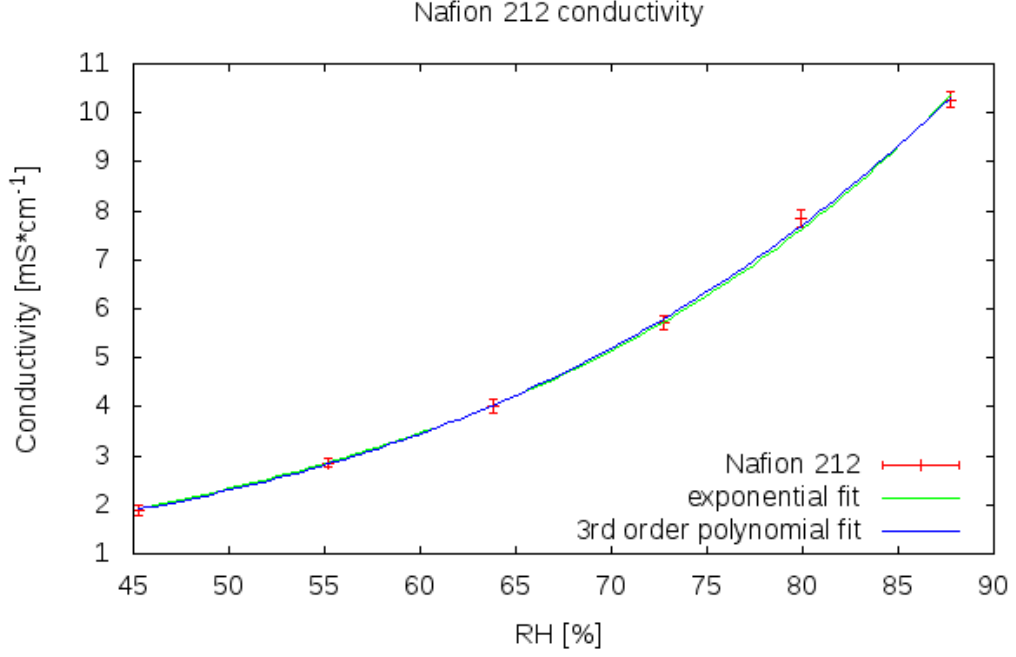
Figure 1.6: Fitting of Equations 1.23 and 1.25 to our measured conductivity of Nafion 212.

along with expanded coefficients for other temperatures. Overall, proton conductivity of Nafion can be described as

$$\sigma(T, \lambda) = \sigma_{300\,\mathrm{K}}(\lambda) \exp\left[1268\left(\frac{1}{303} - \frac{1}{T}\right)\right], \qquad (1.23)$$

where

$$\sigma_{300\,\mathrm{K}}(\lambda) = 0.005193\lambda - 0.00326\,. \qquad (1.24)$$

So far we have seen 2 ways of describing the conductivity of membranes - the Arrhenius equation and the empirical polynomial equation. The question of which is better to fit to experimental data has been posed by Liu et al. [2016], who proposed the following exponential equation:

$$\sigma_{fit}(RH, T) = \sigma_0 + C \exp\left(\frac{RH}{RH_{ref}}\right), \qquad (1.25)$$

where C and RH_{ref} are the fitting parameters, with $\sigma + C$ corresponding to conductivity of dry membrane. They show preference for fitting with the exponential equation 1.25, also claiming that the Arrhenius equation can be used up to $T_{sample} = 80\,°\mathrm{C}$, since higher temperatures cause the membrane to lose water and result in unpredicted drop of conductivity.

We have experimented with fitting both the polynomial and exponential conductivity and found that the polynomial fit has a value of χ^2 roughly 25 % lower than the polynomial fit. However, both fits are well within the error of measurement, as can be seen in Figure 1.6, where we fitted our measured data. We have chosen the exponential fit for this work, since it is based on physical deduction and thus more informative. It will be further denoted as `"fit exp"` in our figures.

2. Experimental methods

In this work, we focus on measurement of performance of fuel cells. Bellow are described the basics of the two popular methods, polarization curve measurement and electrochemical impedance spectroscopy, that were used in this work.

2.1 Polarization curve

Measuring of the polarization curve is considered as the baseline measurement to assess the performance of a fuel cell. Say we construct a new fuel cell and want to test how well the particular assembly performs. Measuring of polarization curve is going to be the first measurement we will do to give us information about the overall performance of the system.

Polarization denotes the shift of fuel cell's voltage from it's open voltage. We measure the curve by changing the electrical current output that the connected potentiostat draws from the fuel cell and measuring the cell's voltage. Plotting these measurements yields a polarization curve. On the x-axis it is customary to use current density instead of current, since fuel cells with larger MEA active surface will yield higher currents not representative of the used components.

Measuring polarization doesn't require an extra measuring device, we only need to connect the wires to the fuel cell's output and to a potentiostat. Another advantage is the speed of measurement - measurement of polarization curve can be used well as a supplementary method of the overall performance in degradation measurements. Measurement of polarization curve is often used as a simple method to find the operating parameters of a fuel cell by varying the operating parameters and comparing the polarization curves.

In the Theory chapter, we have discussed thermodynamic voltage. When describing fuel cell, open circuit voltage (OCV) is used. OCV will always be smaller than the thermodynamic voltage due to contamination, hydrogen and electron crossover, and power losses, as described in Qi [2013]. The power losses can be seen in the I-V curve in Figure 2.1. The curve has 3 areas, where the curve's behaviour corresponds to different dominating processes.

In the high voltage region, the fuel cell's performance is hindered by slow kinetics - this is called the activation loss region. It is connected mainly with the cathode's reaction, since oxygen reduction reaction (ORR) is slow when compared to hydrogen oxidation reaction (HOR) taking place at anode. The activation overpotential is denoted ΔE_A. With decreasing voltage output of the fuel cell, the activation loss is dominated by ohmic resistance. The ohmic loss is a result of all the resistances along the path of electrons and ions in the fuel cell and is called ohmic due to the resistance overpotential ΔE_R being linearly proportional to the current density, described in more detail in Carmo and Stolten [2019].

The last area is characteristic for low cell voltage. This area is characterized by high current density and fast reaction kinetics, which are however limited by mass transport speed. The molecules can't reach the electrode fast enough, resulting in depletion of reactants available at the electrode. We can observe this with water not leaving the cathode fast enough, however the transport loss predominantly arises from insufficient O_2 feed at the cathode side. Wang et al.
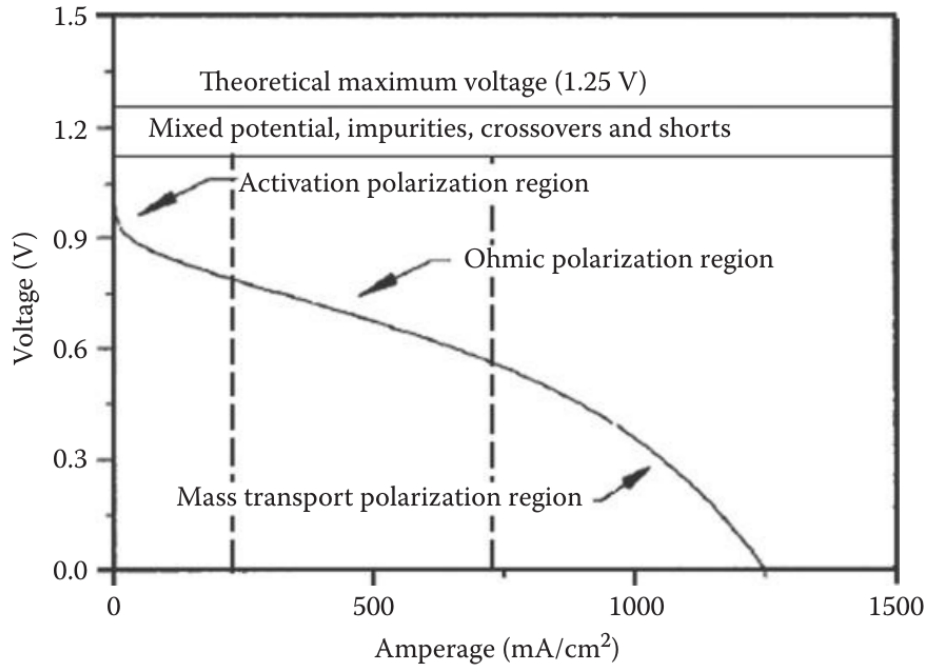
Figure 2.1: An example of a polarization curve from Wang et al. [2012b]

[2015] describe 3 processes driving mass transport inside fuel cell:

Diffusion Movement of species due to concentration gradient, can be described by Fick's law of diffusion.

Migration Movement of charged species due to potential gradient.

Convection Movement due to density gradient.

The end result is the surface concentration of oxygen approaching zero, causing a sharp decrease in the fuel cell's performance. The problem of mass transport is further worsened by mass transport in the other fuel cell's structures. All three of these power losses appear at all voltages, the areas named after them are merely dominated by their contribution to the decrease of the I-V curve.

2.2 Electrochemical impedance spectroscopy

We mentioned in the previous section, that the polarization curve measurement yields information about the overall performance of the fuel cell. It is an integral method, meaning that from physics point of view, the fuel cell is a black box to us. We can't distinguish why the performance is dropping or rising from only the change of the curve. Electrochemical impedance spectroscopy (EIS) is a way to further investigate this black box, giving us more information about why certain changes may be happening.

As the name implies, this method measures the impedance of a system. Impedance is a more general equivalent of resistance, used when talking about

alternating current. It is denoted as Z and defined as

$$Z = \frac{V(t)}{i(t)}, \qquad (2.1)$$

where $V(t)$ is potential at time t and $i(t)$ current at time t. EIS measurements work by introducing a small harmonic perturbation to the system and calculating impedance from the response. We can either apply voltage perturbation $V(t) = V_0 \cos(\omega t)$ or current perturbation $i(t) = i_0 \cos(\omega t)$, where V_0 and i_0 are amplitude constants of voltage and current respectively. The term ω denotes radial frequency of the perturbation.
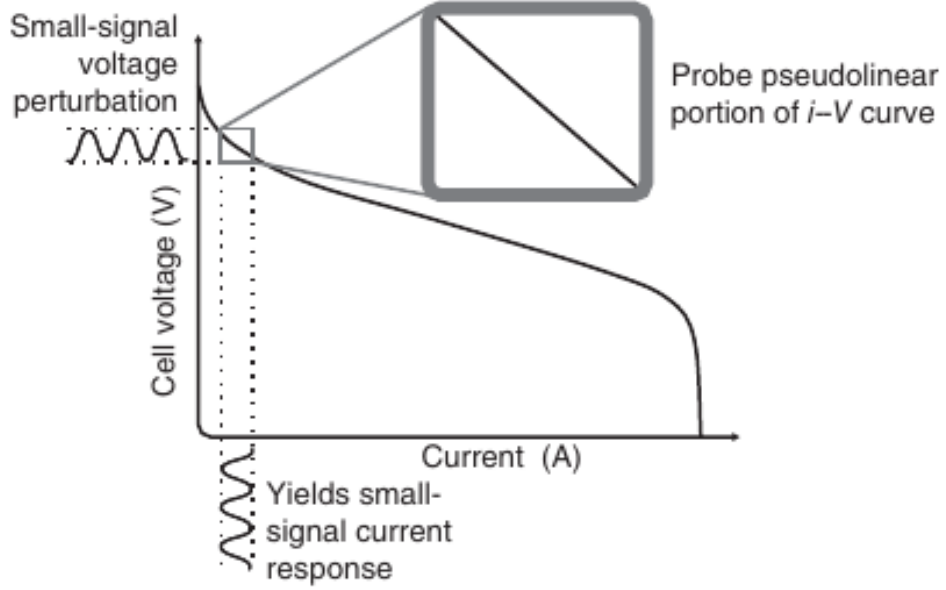
Figure 2.2: Schematic representation of harmonic perturbation response from O'Hayre et al. [2016].

Let's say we introduce potential disturbance V into the system and measure the i response, as shown in Figure 2.2. This response can have a phase shift ϕ compared to the original signal, but the frequency will remain the same, allowing us to distinguish it in the response. The impedance as described in O'Hayre et al. [2016] would then look like

$$Z = \frac{V_0 \cos(\omega t)}{i_0 \cos(\omega t - \phi)} = Z_0 \frac{\cos(\omega t)}{\cos(\omega t - \phi)}, \qquad (2.2)$$

where Z_0 denotes impedance magnitude. It is however more useful to describe impedance using complex numbers as in Horowitz and Hill [2015], which yields

$$Z = \frac{V_0 \exp(j\omega t)}{i_0 \exp(j\omega t - \phi)} = Z_0 \exp(j\phi), \qquad (2.3)$$

where j is the imaginary unit. This can be rewritten using Euler's formula as:

$$Z = Z_0(\cos(\phi) + j\sin(\phi)). \qquad (2.4)$$

The impedance of the system is thus described by its impedance amplitude and phase shift. The overall impedance can be split into real and imaginary part. When plotted against each other, they constitute the Nyquist plot, example of which can be seen in Figure 2.3. This plot has characteristic areas, corresponding to different physical processes.
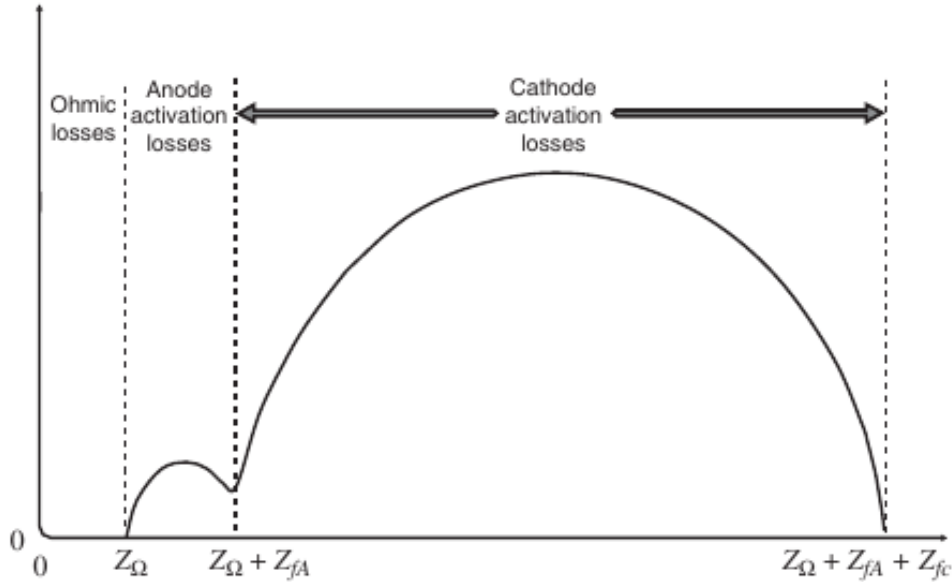

Figure 2.3: Example of a Nyquist plot from O'Hayre et al. [2016]. Z_Ω is equal to ohmic resistance, Z_{fA} denotes anode Faradaic impedance, and Z_{fc} denotes cathode Faradaic impedance.

The x-axis here is the real part of impedance $Re(Z)$ and the y-axis the imaginary part $Im(Z)$. Radial frequency is highest on the left side of the graph and decreases along the $Re(Z)$. To interpret the Nyquist plot, either physical insight or modelling can be used. In modelling, an equivalent circuit is constructed and it's impedance calculated. This impedance curve is then fitted to the measured impedance spectrum. This gives us the ability to distinguish contributions from different physical processes, as the equivalent circuit consists of elements directly representing individual physical and chemical processes that can take place in the fuel cell.

These equivalent circuits are constructed of blocks representing types of processes. These blocks are made up of elements connected in series or parallel to simulate well the process. The method of equivalent circuits is powerful, however it is quite difficult, not only to choose the correct model and fit it, but also because their interpretation is non trivial. This has been emphasized by the work of Danzer and Hofer [2009], showing that the models parameters do not necessarily correlate with the actual physical processes inside fuel cell. Malevich et al. [2019] have indicated that the involvement of processes at different frequencies may not be as simple as thought before. All this ties into the fact that equivalent circuits are non-trivial to construct, calculate, and interpret. As we will see, their use is not vital for our work, as using physical insight is sufficient. In our case this means that the overall value of resistance is taken as the low-frequency intercept of the measured curve, which corresponds to $Im(Z) = 0$ and thus $Z = R$, as

described by Yadav and Fedkiw [2012]. Using equivalent circuit, the overall resistance would be the intercept of the modelled curve in the low-frequency part of the graph.

Two techniques of measurement of the response are available - two-probe and four-probe. When two probes are used, the response of the system is measured by the same electrodes to which the harmonic perturbation is applied to. The four-probe method uses two pairs of electrodes, one to cause perturbation and the other to measure the response. This has the advantage of eliminating the resistance contribution of wires. Mikhailenko et al. [2008] have examined these two techniques and found comparable results. As described in Singh [2013], four-probe method is more appropriate when low resistance samples are measured. We have chosen the four-probe method due to better testing results when measuring etched membranes in the low conductivity region (dry conditions). An example of the arrangement of four probe measurement on a sheet sample can be seen in Figure 2.4.
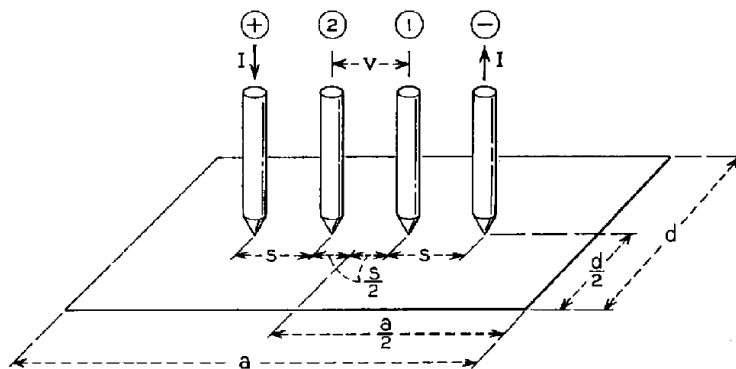
Figure 2.4: Arrangement of the 4-probe method on a sheet sample, schematic from Nedela et al. [2015].

Another choice that can be made is the geometry of probes when attached to the measured medium. The two most common are through-plane and in-plane impedance measurement. Through-plane configuration is in some cases more favourable, as it corresponds to the membrane's resistance inside the fuel cell. Soboleva et al. [2008] have shown anisotropy when comparing through-plane and in-plane measurement, which has been however negligible for Nafion 211. Furthermore, Cooper [2011] have shown that Nafion 212 behaves in an isotropic way. Since this work focuses mainly on these two membranes as the baseline for experiments, the measured conductivity should be comparable.

For our experiments, in-plane measurement technique has been chosen. This is because we wanted to measure etched membranes. Etching is mainly a surface phenomenon, leading us to choose the more surface sensitive in-plane configuration. For this configuration and at water vapour equilibrium, the measured in-plane resistance R of a membrane approximated as a uniform cuboid is

$$R = \frac{L}{\sigma A} = \frac{L}{\sigma WT},$$ (2.5)

where R is the measured resistance, L length between the voltage sensing probes, and A the approximated area the current can travel through, defined as

width W of the sample (perpendicular to the direction of current) times the dry thickness T of the membrane. Reorganizing we arrive at

$$\sigma = \frac{L}{RWT} \, ,\tag{2.6}$$

for conductivity σ. This approximation assumes homogeneous and isotropic electric field. Despite these non-negligible assumptions the formula is an industry standard and so we will use it. The units used with conductivity are usually $\mathrm{S\,cm^{-1}}$.

2.3   Supplementary methods

During this work, scanning electron microscopy (SEM) and energy-dispersive X-ray spectroscopy (EDX) have been used as supplementary methods to measure degradation of EIS electrodes to investigate measuring failure. In order to keep this work comprehensive, a brief description of the principle of these techniques is given below.

2.3.1   Scanning electron microscopy

SEM uses a beam of electrons to scan the surface of a sample. These electrons interact with the surface and the response is measured, producing images of the sample's surface. From the response, information about the sample's surface morphology and structure can be deduced. The resolution of scanning electron microscope can be in the order of nanometers.

The beam electrons are emitted from the cathode and accelerated by high positive anodic voltage in the order of 10 kV. The electrons then travel through a series of electromagnetic lenses, that focus the beam in order to achieve a beam diameter at the sample few nanometers wide. The lenses can also deflect the beam, allowing for the scanning of the sample. A schematic of SEM can be seen in Figure 2.5.

There are multiple interactions of the beam electrons, also called the primary electrons, with the sample. For our purposes, we well be interested in two of them. The first one is secondary electrons (SE) detection. Secondarily electrons are ejected from valence or conduction bands of the sample by the primary electrons. They have low energy (less than $50\,\mathrm{eV}$), which makes secondary electrons detection a surface sensitive method.

The second method is detection of backscattering electrons (BSE). These come from elastic interaction of the primary electrons with the sample's atoms. Atoms that are heavier backscatter more electrons, meaning that areas consisting of heavier atoms will be bright in the final image. On the other hand, lighter atoms backscatter less and will be thus visible as darker areas. When combined, these two methods give us the morphology of the surface (SE) and an insight into the composition of it (BSE). Whilst SE is very surface sensitive, the back scattered electrons can travel from deeper inside the sample, as is shown in the schematic Figure 2.6.
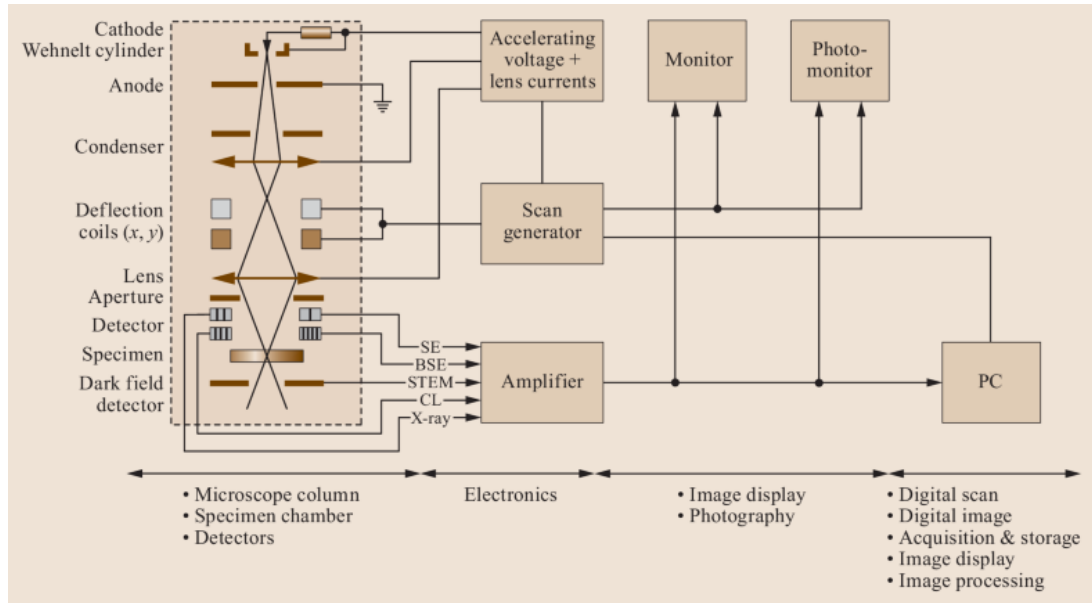
Figure 2.5: Schematic of scanning electron microscope, from Erdman et al. [2019].

2.3.2 Energy-dispersive X-ray spectroscopy

EDX is often a complementary method to scanning electron microscopy. As can be seen in Figure 2.6, the primary electrons produce x-rays from the sample. These x-rays are produced by inner-shell excitation of electrons. Lower energy electrons are excited by the primary electrons into higher energy levels and their subsequent relaxation causes the electron to emit it's extra energy by emitting x-rays. Due to discrete energy levels of atoms, the wavelength of these x-rays is characteristic to a specific element.

When the excited electron relaxes to a ground state, it can also emit an Auger electron instead of characteristic x-rays. The probability of characteristic x-rays emission is proportional to atomic number, meaning that EDX is more sensitive for the measurement of heavier elements. The results of EDX measurement is a spectrum, where peaks correspond to the characteristic transition in the measured sample, thus to a specific element. The advantage of EDX is the ability to map the sample, showing us which parts of the sample consist of what elements.
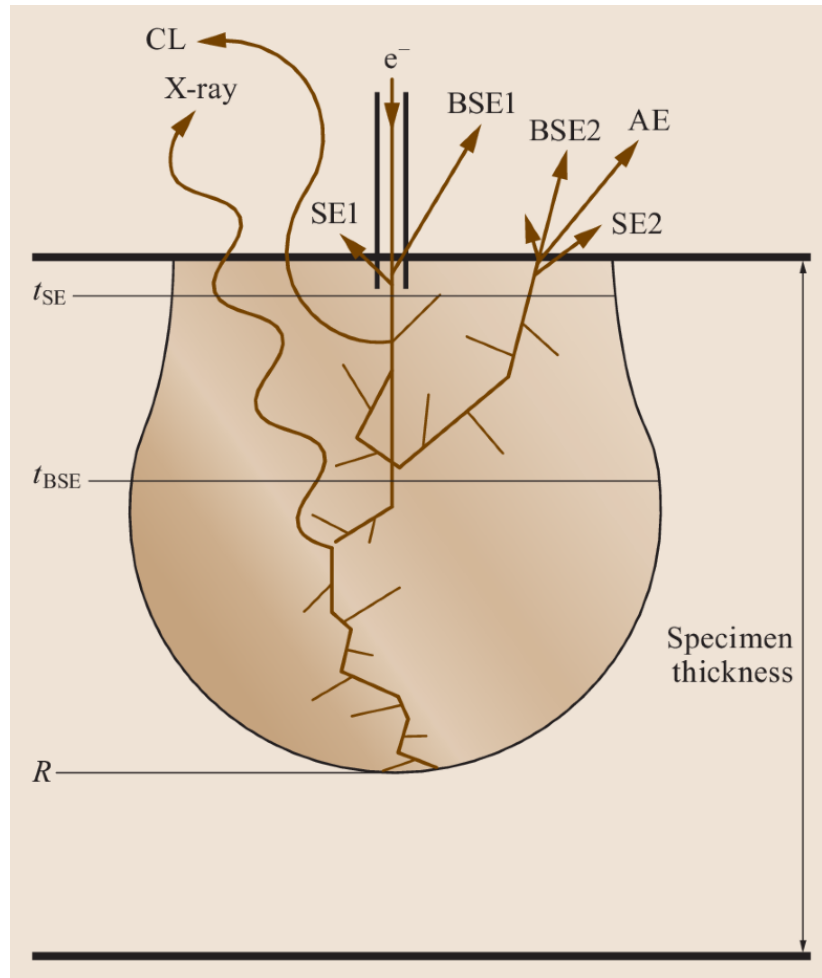
Figure 2.6: Schematic illustration of electron generation in sample, from Erdman et al. [2019]. t_{SE} and t_{BSE} indicate the escape depth for SE and BSE respectively, R is the range of electrons.

3. Humidity chamber PEIS

The main focus of this work has been a construction of a new measuring system to better understand altered membranes created at our department. A standard way of testing new membrane's performance is to construct a fuel cell with the new membrane and then measure the fuel cell's performance. This usually consists of polarization curve measurement for overall performance information and EIS for more information about the individual contributions to the fuel cell's resistance.

This approach is easy, since there is no need for extra infrastructure in order to measure the new membrane's performance. It also has the advantage of showing us the performance of the membrane when used in an actual fuel cell. But to distinguish the performance of the membrane alone, we have to interpret the EIS spectra measured from the fuel cell. From the performance measurements we get a good idea whether the membrane performs good, but we can't get any further information. When the membrane is inside a fuel cell, we can't define the conditions of the membrane.

Relative humidity inside the fuel cell is non-homogeneous and complicated. There are bound to be water droplets, which can rapidly change conductivity of the membrane. Similar problem is with temperature, which in general is non-homogeneous inside the fuel cell and can affect the measurement. Flooding and other processes unrelated to the membrane can greatly change the fuel cell's performance, making it difficult to distinguish the membrane's performance. Fuel cell's performance can also drop due to poor construction or faulty components.

The solution to this problem is simple - to measure the membrane by itself in a humidity chamber. Inside the chamber, precise levels of relative humidity and temperature can be achieved, allowing us to study the membrane's performance under well defined conditions. This is vital when we are interested in the performance of the membrane under different humidity conditions and allows the researcher to gain more insight into the membrane's behaviour. Due to the absence of the surrounding fuel cell, the measurements are easier to repeat and the error of measurement is much lower.

3.1   System design

The design of our measuring system has been influenced by the works of Matos et al. [2014] and Al-Madani et al. [2015]. Let's start with a rough outline of the system: we want to build a chamber inside which we can measure EIS on a proton exchange membrane with well defined humidity and temperature. In order to achieve stability of humidity inside, humidified gas will be brought into the chamber, where the membrane will be let to absorb water from the surrounding humidified gas and then EIS will be measured. In order to manipulate temperature inside the chamber, heating system also has to be incorporated.

Firstly, we have chosen nitrogen as our gas, since it can be used pure in laboratory conditions. This promotes reproducibility of experiment when compared to using air. Nitrogen is also relatively cheap and can therefore be used in large flows. Since nitrogen is non-toxic, the humidity chamber doesn't have to be sealed. This allows us to continually flow humidified nitrogen into the chamber,
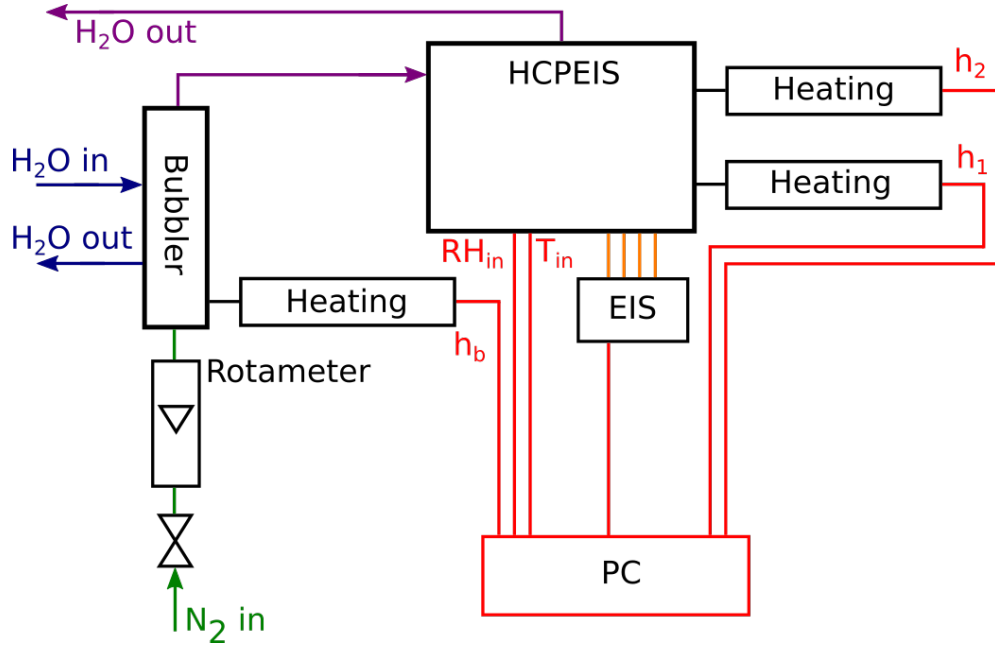
Figure 3.1: Diagram of the proposed HCPEIS system.

allowing the excess gases to exit the chamber via the chamber's water outlet.

This achieves dynamical stability inside the chamber, which is preferable. If we were to pump the chamber of humidified gas, seal and then measure, we would have to deal with cooling of the system and more importantly with condensation of water. When water droplets are formed, they create local disturbances in stability of the humidity inside. It is therefore preferable to continually flow humidified gas inside and flush any excess water out.

Since there is an outlet, the system won't pressurise, which greatly simplifies the choice of the chamber itself. For longevity reasons, the system has to be resistant to corrosion even in high temperatures and humidity. The ranges we want to measure with the membranes are $30\,°C$ to $80\,°C$ for temperature and $30\,\%RH$ to $90\,\%RH$ for relative humidity (RH). The temperature range represents typical operating range of a fuel cell.

In Figure 3.1 we can see a diagram of the system. At the bottom left corner, nitrogen is connected. There is a valve for shutting the system off, followed by rotameter, for measuring the flow of nitrogen into the chamber (Allcat MC 55 LPM flowmeter has been used instead of the proposed rotameter, as it can be connected to the automation unit and operated via the computer). The dry nitrogen then enters the bubbler. The bubbler can be refilled with water and is heated from the outside. The regulating temperature for heating is on the top of the bubbler, where the warm, humidified gas exits.

The humidified air then enters the humidity chamber, which is heated by two external heatings. There are temperature sensors on top of the heatings to prevent overheating of the walls. Two more heat sensors are inside the HC: one by the back wall where humidified air enters and one directly next to the sample holder. The excess water gets gradually flushed out of the system by a tube connected at the bottom of HC, with flow of air pushing it to the tube and gravity forcing it to an external reservoir, from which the bubbler is periodically refilled. All of the heatings are operated by PID regulators from an external computer.

3.2 Achieving stable humidity and temperature

The most important part of designing HCPEIS is the ability to achieve stable humidity and temperature conditions inside. This is more so important since temperature and humidity are not independent variables. We have already mentioned that dynamic stability is achieved inside the system, so let's examine this in more depth.

Firstly, we start with humidity. Humidity inside the chamber is regulated by the PID regulator measuring temperature at the outlet of the bubbler. As the dry nitrogen is bubbled into the water inside bubbler, it carries with itself a portion of water dependent on its temperature. The higher the temperature, the more humidity, as per Equation 1.14.

There are several unwanted scenarios that disturb the balance of humidity inside. First one is having the gas create bubbles inside the bubbler all the way to its top, resulting in the escaping gas carrying droplets of water with it into the chamber. We have mitigated this issue by using a long bubbler with low water level and lower flows of nitrogen. Despite these precautions, water can still reach the outlet, which is why we have installed a simple water trap, thus mostly eliminating water travel directly from bubbler into the chamber.

Another such scenario is water condensation inside the tubes. The air gets heated inside the bubbler and then travels into the water trap and then via a Teflon tube into the chamber. On this route the hot humidified nitrogen is cooled by the walls of the tube and water droplets condense. These get eventually pushed by the flow into the chamber. We have alleviated this by making the tube as short as possible and heat insulating it. If the system design doesn't allow for short distance, tube heating would have to be implemented.

Similar problem is the condensation of water inside the chamber itself. First, let's talk about how the humidity chamber is heated. The stainless steel walls get heated by 2 outer heating elements attached to its surface and conduct the heat throughout the hull by conduction. By convection the humidified air inside gets heated. Problem arises when the entering humidified gas is heated to a higher temperature than the surface of the chamber or the air inside. Water droplets then condense on the sides and are eventually forced by gravity to the collector at the bottom and flushed out.

This is highly undesirable scenario, since water droplets disturb the humidity balance inside the chamber and once created, are extremely difficult to eradicate from the chamber, usually forcing the user to vent and dry the chamber, compromising the measurement. However, if we want to measure at high humidity (meaning high bubbler temperature and consequently high temperature of nitrogen) and low sample temperature, the entering air would be hotter than the chamber and immediately start condensing and stable levels of RH would be difficult to achieve.

We have partially weakened this problem by using a larger chamber. This might seem counter-intuitive at first. Larger chamber means longer time to achieve desired conditions inside and larger temperature gradient inside. It also needs larger flows of humidified air to keep the dynamic stability inside, thus raising the risk of pushing water inside the system. However, larger system has the advantage of being less prone to disturbances. This allows us to measure

values even at high humidity levels even at low temperature, data which can be vital to the development of novel membranes.

Before the construction of our humidity chamber, we have summarized our requirements of the system into a short list:

Stability Temperature and RH levels inside the chamber should be stable for the duration of EIS measurements.

> **Temperature** Inside the chamber, there should be well defined temperature near the sample. Uniform heat distribution inside the chamber is optimal. There should not be a temperature gradient of such magnitude, that water condenses.

> **Humidity** The humidity levels inside should be stable and undisturbed by any droplets. This means prevention of condensation and prevention of humidified nitrogen carrying water droplets into the chamber.

Speed of measurement Membrane water adsorption should be the time limiting process.

No overshoot Since drying out of membranes is a slower process than humidification, no overshooting of humidity or temperature levels should take place.

Reproducibility Constant pressure to membrane should be applied regardless of it's thickness. Probes should not damage even wet membranes. Under the same operating parameters set, the conductivity measurement should be reproducible within the error of measurement.

3.3   Humidity chamber

For the humidity chamber itself, an autoclave has served as a basis. Used as a sterilization chamber for dentists, it is built to withstand temperatures exceeding $100\,°C$ and high humidity levels. It's tilted cylindrical design promotes the flow of condensed water droplets into the outlet. The volume of the autoclave is $13.5(2)\,L$.

The walls are covered with heating elements (strength of $1\,W$ at the top part and $2\,W$ on the bottom of the cylinder). Their power output is controlled by the main regulator according to the temperature inside the chamber. A limit of $130\,°C$ has been set to prevent overheating. This is especially important if the operator forgets to turn the regulator off before opening the chamber. The heating elements are covered in heating insulation, which has been a key element in reducing condensation and promoting more homogeneous distribution of heat.

For relative humidity measurements, Vaisala HMT337 Humidity and Temperature Meter was used. In the range from $0\,°C$ to $90\,°C$ it has guaranteed precision of $\pm1.5\,\%RH$ at $0\,\%RH$ in the environment and linearly grows to $\pm3\,\%RH$ at $100\,\%RH$ in the environment as described in the meter's datasheet (Vaisala [2019]).

3.4 Sample holder

Inside the chamber, the membrane is held by the sample holder. The model of our sample holder can be seen in Figure 3.2 and the actual sample holder in Figure 3.3. We have chosen the 4-probe method, measuring the membrane in in-plane configuration for the purpose of measuring difference in surface conductivity of the etched side of a membrane.
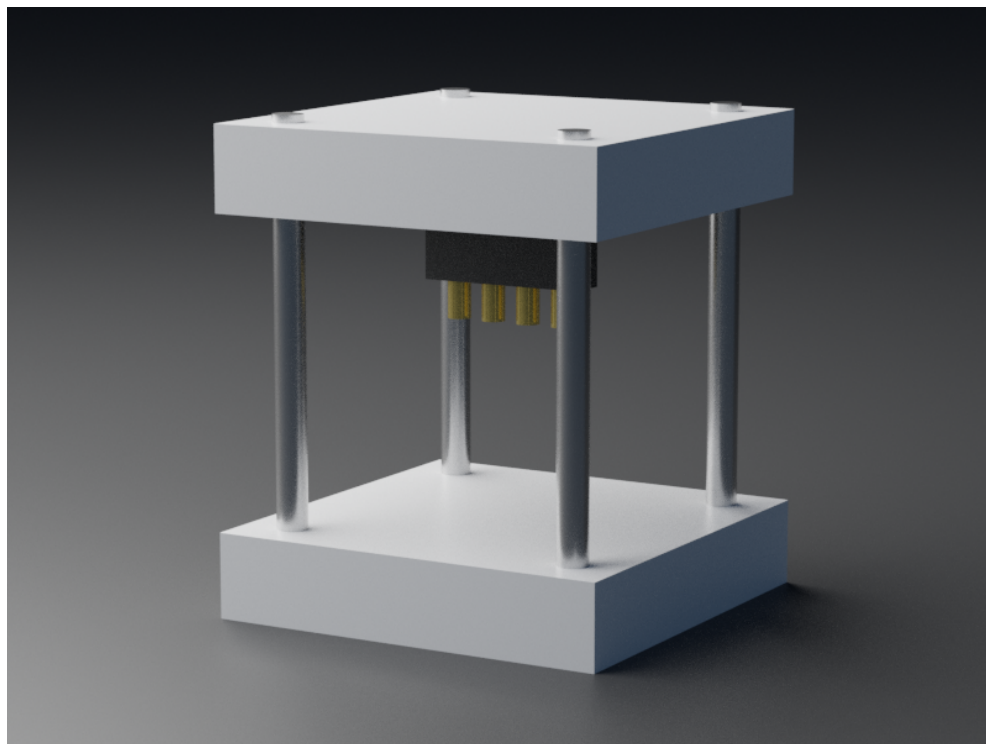

Figure 3.2: Model of our design of EIS 4 probe sample holder.

The sample holder itself is made of 2 Teflon pieces connected by 4 metal rods. Teflon has low thermal conductivity, isolating the sample from the walls, as they achieve much higher temperatures than the nitrogen inside. It is also an electrical insulator, thus preventing short-circuiting of the measurement. Another advantage is Teflon's hydrophobicity, which combined with it's smooth surface promotes flow of any accumulated water off of the holder.

There is another design of a 4-probe sample holder that can be found in the literature, for example in Yuan et al. [2010], which can be seen in Figure 3.4. For clarity, let's call the design Yuan et al. [2010] implemented the screw design, since this design uses 2 Teflon blocks that are screwed together to keep the membrane in contact with 4 platinum wires. Humidified air can reach the membrane by the cutouts in the Teflon pieces. We have constructed and tested our prototype of the screw design, which can be seen in Figure 3.5 and with connected EIS in Figure 3.6.

Our reproduction of the screw design worked and yielded expected results. However, we wanted to test a design that allows for future possible automation. This lead us to our design, which has also the advantage of greater surface of the membrane being exposed to humidified air. Our design also makes the change of sample much faster and can be comfortably done inside the chamber. This
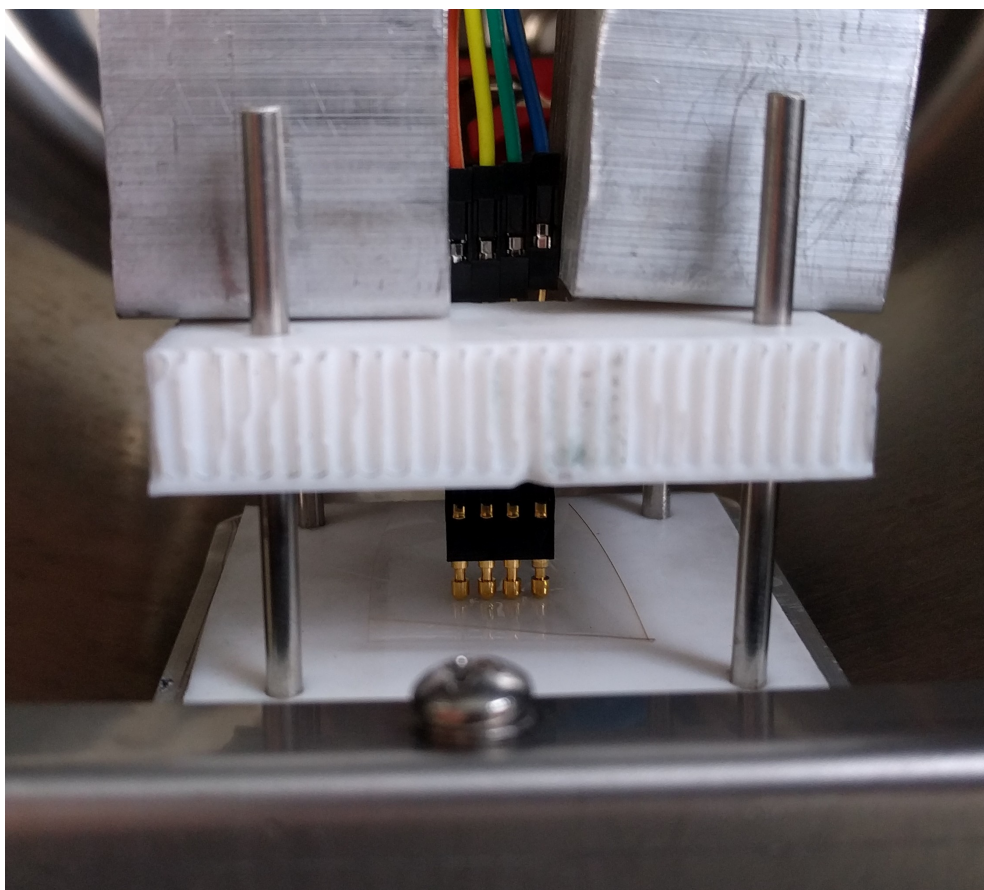
Figure 3.3: Final sample holder used in this work.

is important if we want to establish conditions inside and measure 2 different samples one after the other. With the screw design, the change of the membrane is more complicated, leading to more time when the chamber is open, prolonging the time it takes to again achieve the same conditions inside.

As we can see in the Figure 3.3, in our system the membrane is pressed by the EIS tips to the Teflon underneath. When compared to the screw design, in our case the membrane can move freely as it swells up, leaving smaller chance for tearing of the membrane. The membrane is pressed by weight resting on top of the top Teflon plane, which improves reproducibility of the experiment. This is due to the fact that pressure on the membrane influences the contact surface with electrodes, meaning the screw design should be screwed the same way. Having constant weight resting on top of the membrane is easier to achieve. In our case, the weight of the sample holder with the weights is 372(1) g.

Another advantage of our design is that the sample is covered from the top. When measuring in high humidity conditions, water may condense at the top of the chamber and fall onto the sample. A water droplet can drastically change the results, locally creating highly humidified area.

3.5 Electrodes

In our setup, the electrodes press on the membrane in perpendicular way. The probes used are semi-spherical P25-0423 Harwin Spring Probes with a diameter of
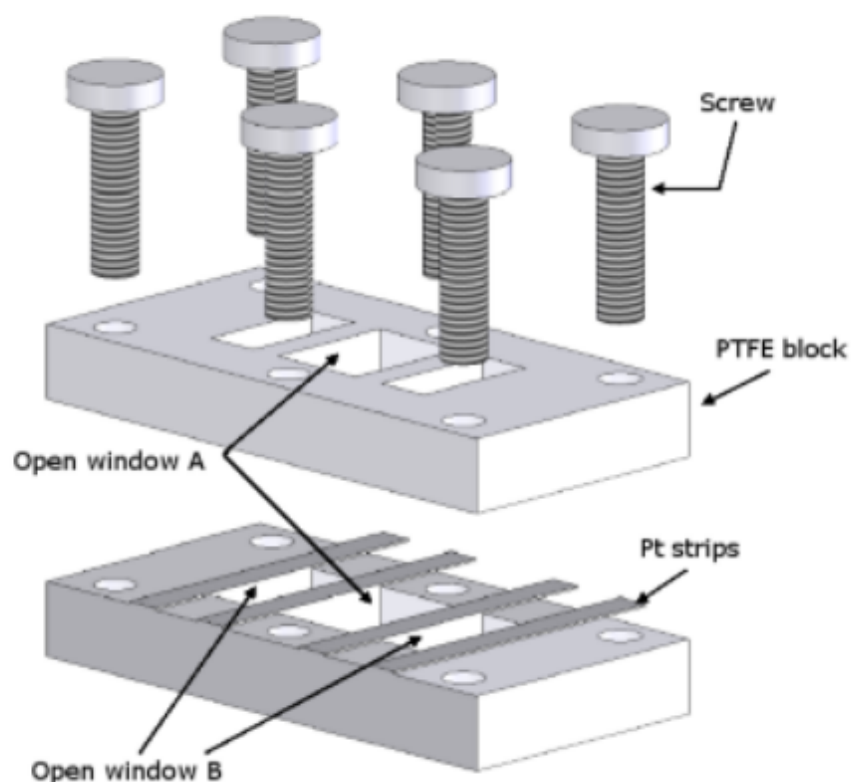
Figure 3.4: Sample holder proposed by Yuan et al. [2010]

Figure 3.5: Our prototype of a screw design sample holder.
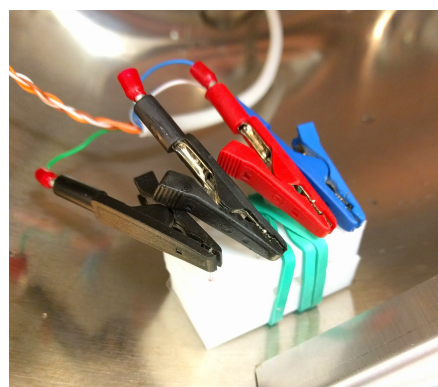
Figure 3.6: Our prototype of a screw design sample holder connected to EIS.

1.8 mm. They are made out of copper alloy plated with gold, an industry standard for electronic measurements. The semi-spherical ends, which come into contact with the membrane, are spring loaded, making them well suited for possible future automation of the measurement. The springs also help to achieve proper contact, when the sample holder is weighted. The four electrodes are in a plastic holder with 0.1 inch or 2.54 mm spacing in between them. The shape of the electrodes can be seen in Figure 3.7.
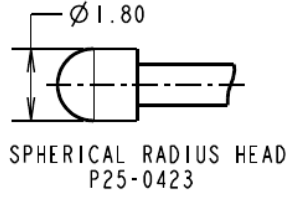
Figure 3.7: Shape of the used semi-spherical probes. Diameter is in mm.

3.6 Testing the system

Upon completion of the system, we have conducted tests to see if the system functions as desired. This consisted of checking all of the requirements we have set at the beginning of this chapter and running testing measurements to see if all worked well. First we reviewed if the changes of operating parameters worked well.

3.6.1 Humidity chamber operating parameters

The HC has to be able to achieve desired ranges of operating parameters and be able to change them. At first, many measurements have been conducted. These have shown that the system is able to achieve temperature ranging from room temperature to $75\,°C$. Higher temperatures can be achieved (especially with higher humidification, since heat conductivity rises), but upwards of $75\,°C$ it takes more time to heat up the chamber, than it takes Nafion to achieve equilibrium with new operating parameters.

This is mainly caused by the combination of the size of the system and the poor thermal conductivity of nitrogen. The temperature range could be improved by using smaller sized system or including heat conducting scaffolding inside. For our measurements, the upper temperature boundary has been satisfactory.

Relative humidity range is from $15\,\%RH$ to $95\,\%RH$. Measuring at lower $\%RH$ is very well possible, however Nafion's conductivity became too low for our impedance spectrometer to give well interpretable data. At higher relative humidity than $95\,\%RH$, measurement of RH becomes unstable, since water is very likely to condense.

We have further investigated all the operating parameters by counting correlation matrix from measurements throughout the viable ranges of operating conditions. Correlation is a statistics function describing relation between two functions - more specifically it describes how much they correlate. In layman's terms, if one function X grows on interval A, then function Y with high correlation also grows on interval A. Correlation is a well described indicator of dependence. It's definition (from James et al. [2013]) for discrete functions X and Y is:

$$\text{Cor}(X,Y) = \frac{\sum_{i=1}^{n}(x_i - \bar{x})(y_i - \bar{y})}{\sqrt{\sum_{i=1}^{n}(x_i - \bar{x})^2}\sqrt{\sum_{i=1}^{n}(y_i - \bar{y})^2}}\,, \tag{3.1}$$

where $\bar{x}$ and $\bar{y}$ denote mean values of X and Y respectively. The measured correlation matrix (Figure 3.8) is a graph of correlation values of functions belonging to all HC operating parameters. The values range from -1 to 1 and their meaning
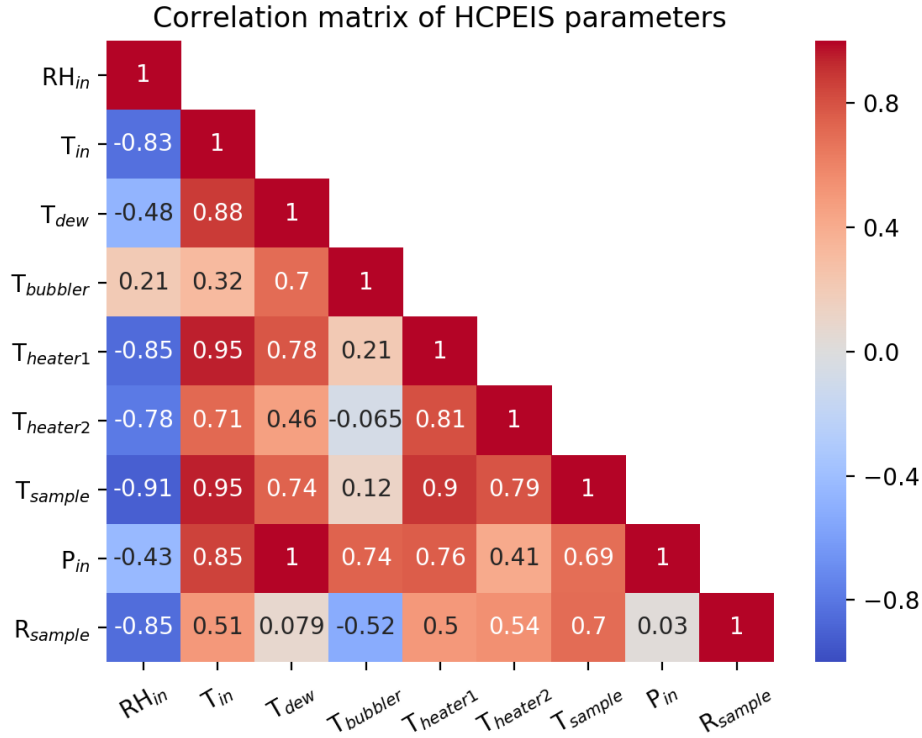
Figure 3.8: Correlation matrix of the operating parameters of HCPEIS.

Value	Meaning
1	correlation
0	no correlation
-1	anticorrelation

Table 3.1: Correlation matrix values.

is described in Table 3.1, with anticorrelation meaning that if X function rises on A, Y functions has exactly inverse behaviour on A. The reason for using correlation is to gain insight into the co-dependence of the operating parameters inside, possibly uncovering any undesired correlation of operating parameters which are supposed to be uncorrelated.

The abbreviations used in the correlation matrix are described below:

RH_{in} Sensor measuring RH. The sensor is located at the back wall of the chamber.

T_{in} Thermocouple measuring temperature at the back wall of the chamber.

T_{dew} Dew temperature calculated from measured RH_{in} and T_{in}.

$T_{bubbler}$ Temperature of humidified gas at the outlet of bubbler.

$T_{heater1}$ Temperature of the top heating of the chamber, measured between the chamber wall and the heating.

$T_{heater2}$ Temperature of the top heating of the chamber, measured between the chamber wall and the heating.

T_{sample} Thermocouple measuring directly next to measured sample.

P_{in} Pressure inside calculated from measured RH_{in} and T_{in}.

R_{sample} Resistance of the sample measured by EIS.

In describing the correlation matrix, we will start with the most anticorrelated and progress towards the highly correlated operating parameters. We can see that R_{sample} is highly anticorrelated with relative humidity inside the chamber, which perfectly obeys Equation 1.23. We can also see that the two heaters and temperature inside the chamber are anticorrelated - this is also in order, as higher temperature means that nitrogen has higher capacity for water uptake and thus smaller relative humidity. Relative humidity inside is also somewhat anticorrelated with pressure inside chamber, satisfying Equation 1.21, but with taking into account dependence on temperature (influence of temperature is visible from the correlation between P_{in} and T_{in}, the value of which is 0.85).

We can see weak correlation of pressure inside the chamber and the resistance of the sample - this is as expected. More interesting is correlation value of 0.12 between $T_{bubbler}$ and T_{sample}. This means that despite the large flow of humidified nitrogen, the hot gas doesn't strongly influence the temperature inside. This means our temperature regulation can compensate well the influx of hot or cold gas. However, we can see that the value of correlation between $T_{bubbler}$ and T_{in} is quite a bit higher at the value of 0.32. From this we can deduce that even though the local environment around the sample isn't strongly influenced by the temperature of entering gas, the area closer to the gas inlet is somewhat influenced. This indicates a temperature gradient inside the chamber. This presumption turned out to be true, as will be seen later. Despite this we can see high correlation between the 2 values, which is satisfactory for us considering the size of the system.

We can see high correlation values of sample temperature and the temperature of heatings, which was expected. We can see that the 2 heaters have a slightly different correlation with temperature inside - this is due to the lower heating having both higher power output and being closer to the sample, but isn't a flaw.

3.6.2 Measuring range

Typical fuel cell operating conditions range from room temperature to 80 °C (Qi [2013]). We would want the same with our humidity chamber, as well as a large range of RH achievable inside. For this purpose wide range of values has been measured, which are shown in Figure 3.9. The HC has no trouble achieving any combination of relative humidity and temperature that a hydrogen fuel cell might achieve apart from two areas. Let's start with the left bottom one, which will be called the low-temperature limit. If the temperature inside is too low, the water vapour capacity of the gas inside is also low. This means that the limiting factor here is the usage of a bubbler - which, even if not heated, saturates the flowing nitrogen with enough water, that at these low temperatures, low

RH measurements are unobtainable. A solution might be mixing the humidified nitrogen with dry nitrogen at the outlet of the bubbler, thus enabling for lower RH values to be measured.

The other unobtainable region is the high temperature, low RH region. This will be called the high temperature limit. We have found two factors that enforce this high temperature limit. First one is the fact that the low relative humidity nitrogen has to travel through a cold bubbler. Due to our system's lack of cooling mechanism, the lowest temperature possible of the nitrogen is room temperature, which for some values would mean the temperature difference of more than 50 °C. This means that cooler air is coming into the chamber, effectively cooling it.

The second factor is low thermal conductivity of dry nitrogen. This is no small contribution, the effect of which can be seen in the temperature difference changing with RH in Figure 3.10, where temperature was measured at two points inside the chamber, indicating temperature difference dependent on relative humidity. These factors tie in with the problem of insulation, inherent to the chosen size of the chamber and the difficulty of insulating certain parts of the chamber, such as the opening.
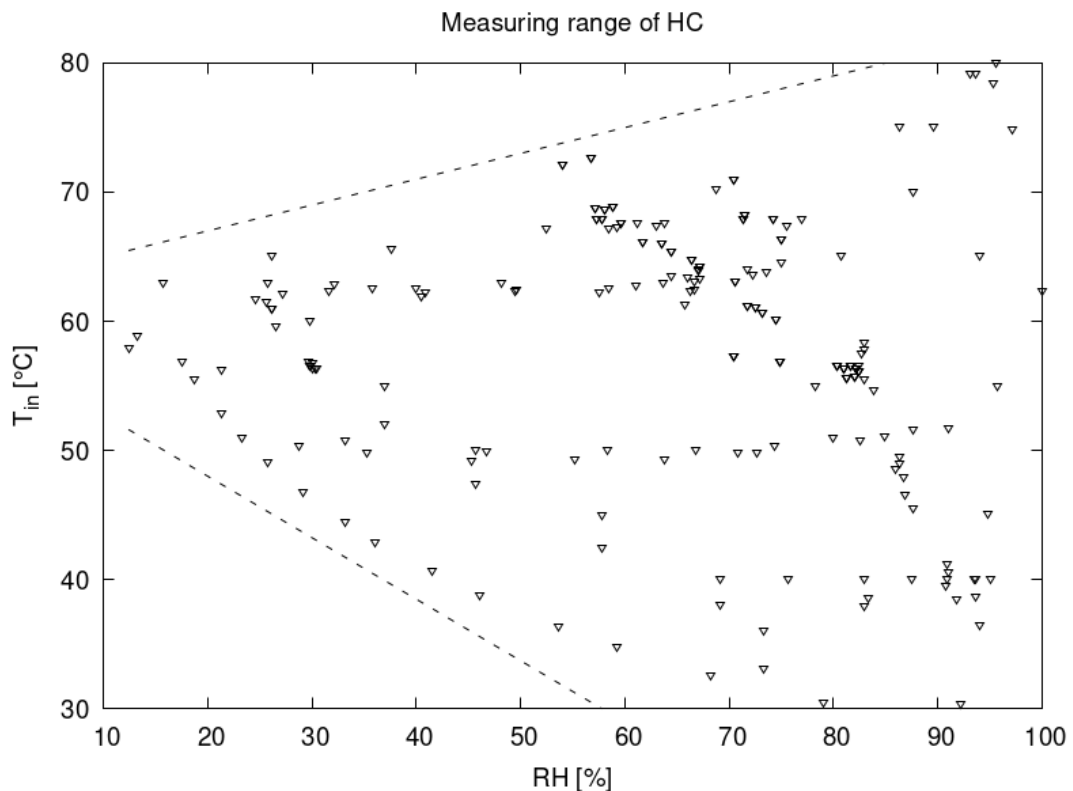
Figure 3.9: Measuring range of the constructed HC.

3.6.3 Environmental stability

Vital property of the humidity chamber is it's ability to achieve stable well defined conditions inside. In the previous chapter, we have shown how the operating parameters influence each other and found indication of temperature gradient inside the chamber. We have confirmed this by direct measurement, comparing

the values T_{sample} and T_{in}. An example of one measurement can be seen in Figure 3.10, where temperature has been measured in approximately 5 min long intervals. We can see high correlation of the two curves, except the area from $Time = 120$ to $Time = 140$, where T_{in} had a distinctly lower values.

This has been caused by refilling of the bubbler with recirculated water. The water is replenished when the water level inside bubbler reaches a low enough value. For refilling, the water that exits the HC is used, which however had time to cool down. When additional colder water is filled in into the bubbler, for a short time (depending on the amount of water filled, in this case $\approx 20\,\text{min}$) the outgoing humidified air has lower temperature. Due to the large size of our chamber, this change of temperature of the incoming air is not registered by the thermocouple near the sample.
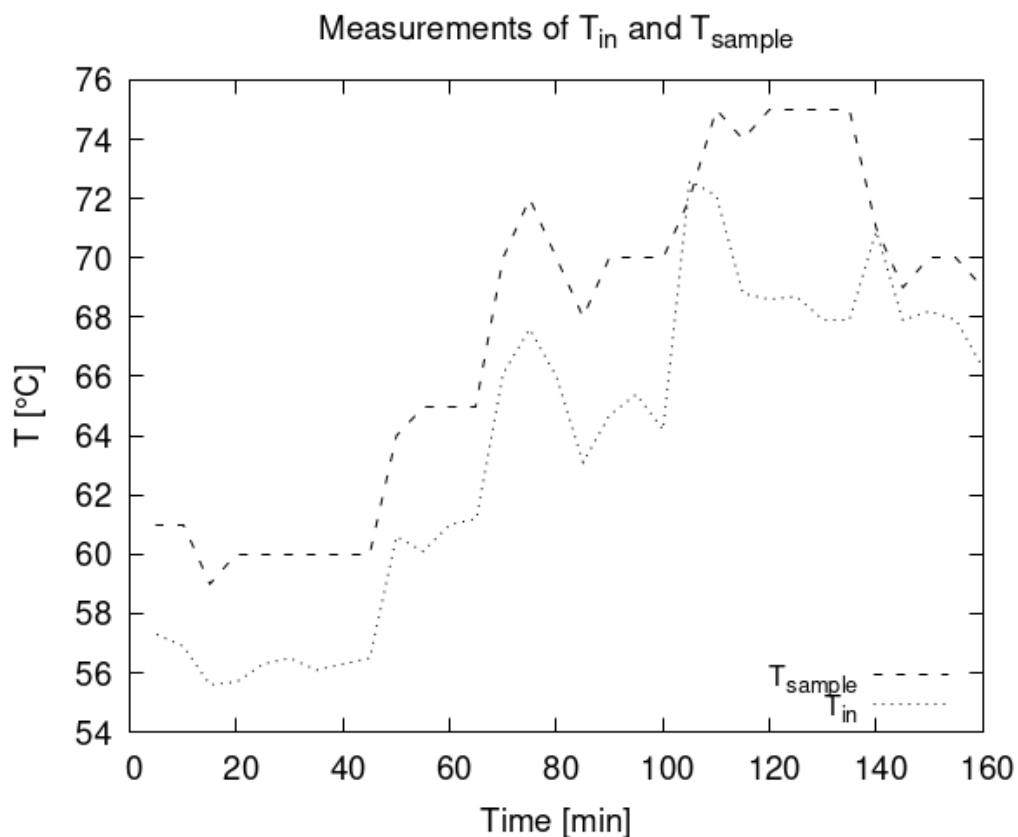
Figure 3.10: Temperature inside the chamber as measured by the two thermocouples.

In Figure 3.10, we can see there is a roughly constant difference between the two measured values. This difference has been investigated further, using measurements across wide range of temperatures, arriving at an average temperature difference equal to $\Delta T_{avg} = 6(2)\,°\text{C}$. The temperature difference is a function of temperature and relative humidity. Higher temperature inside the chamber leads to higher temperature difference, as the gas inside is not capable of conducting the heat well enough. On the other hand, higher relative humidity is inversely proportional to temperature difference, due to higher thermal conductivity of humidified air (described well by Beirão et al. [2012]). These results can be seen in Figure 3.11 for two chosen temperatures.
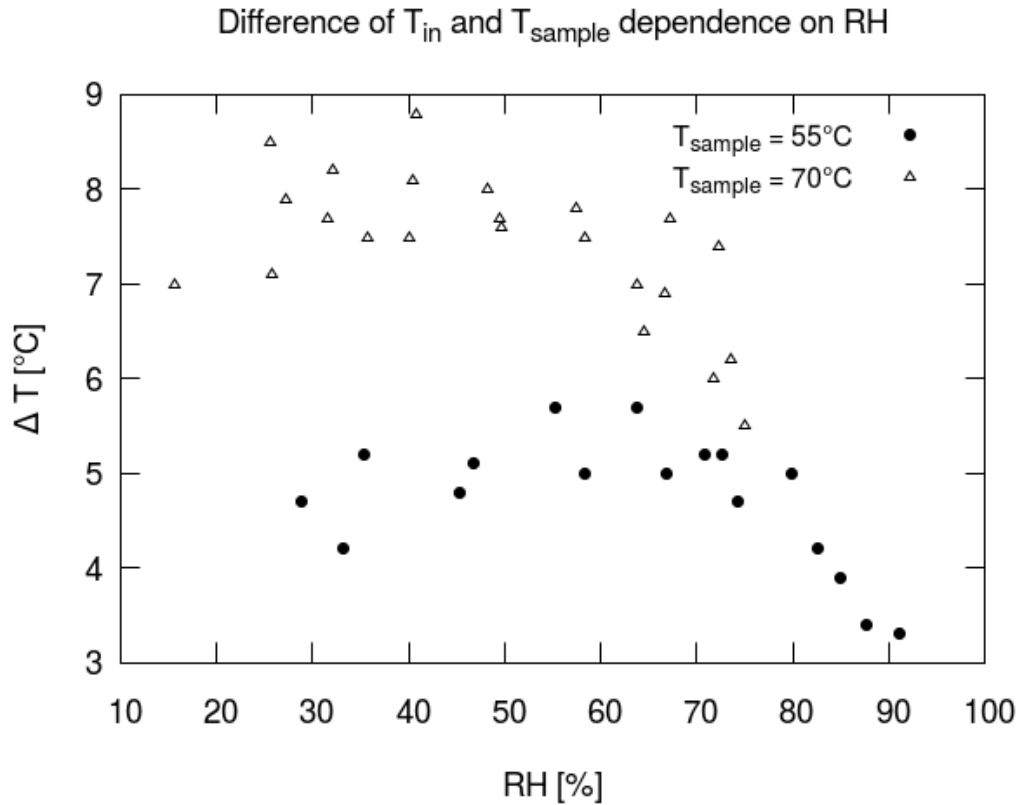
Figure 3.11: Dependence of temperature gradient inside the HC on RH.

For the stability of operating parameters, input values were set and the resulting ability of the system to keep the corresponding parameters constant was observed. The results can be seen in Figure 3.12, where at time equal to 0 the operating values of both the bubbler temperature and chamber temperature have been changed to a new value. The measured values represent measurements of temperature, RH, and calculated conductivity of a Nafion 211 sample. Dashed lines denote the regions of values that can be considered stable. It can be seen that it takes approximately 15 min to achieve stable temperature and RH levels inside the chamber. Stable conductivity corresponds to the membrane being in equilibrium with the surrounding water vapor, with the process taking approximately 30 min. For conductivity measurements, the measurement of 3 consecutive values within the error margin of EIS measurement has been chosen as stable, with 30 min being the standard time interval between measurements. All the measured conductivity values in this work have been measured this way.

Last but not least, we have tested the linearity of humidity increasing inside the chamber due to bubbler temperature change. The results can be seen in Figure 3.13. It can be seen that while the RH inside the chamber is below 80 %RH, the dependence is linear. Above the threshold, higher relative humidity levels require non-linearly higher bubbler temperature.
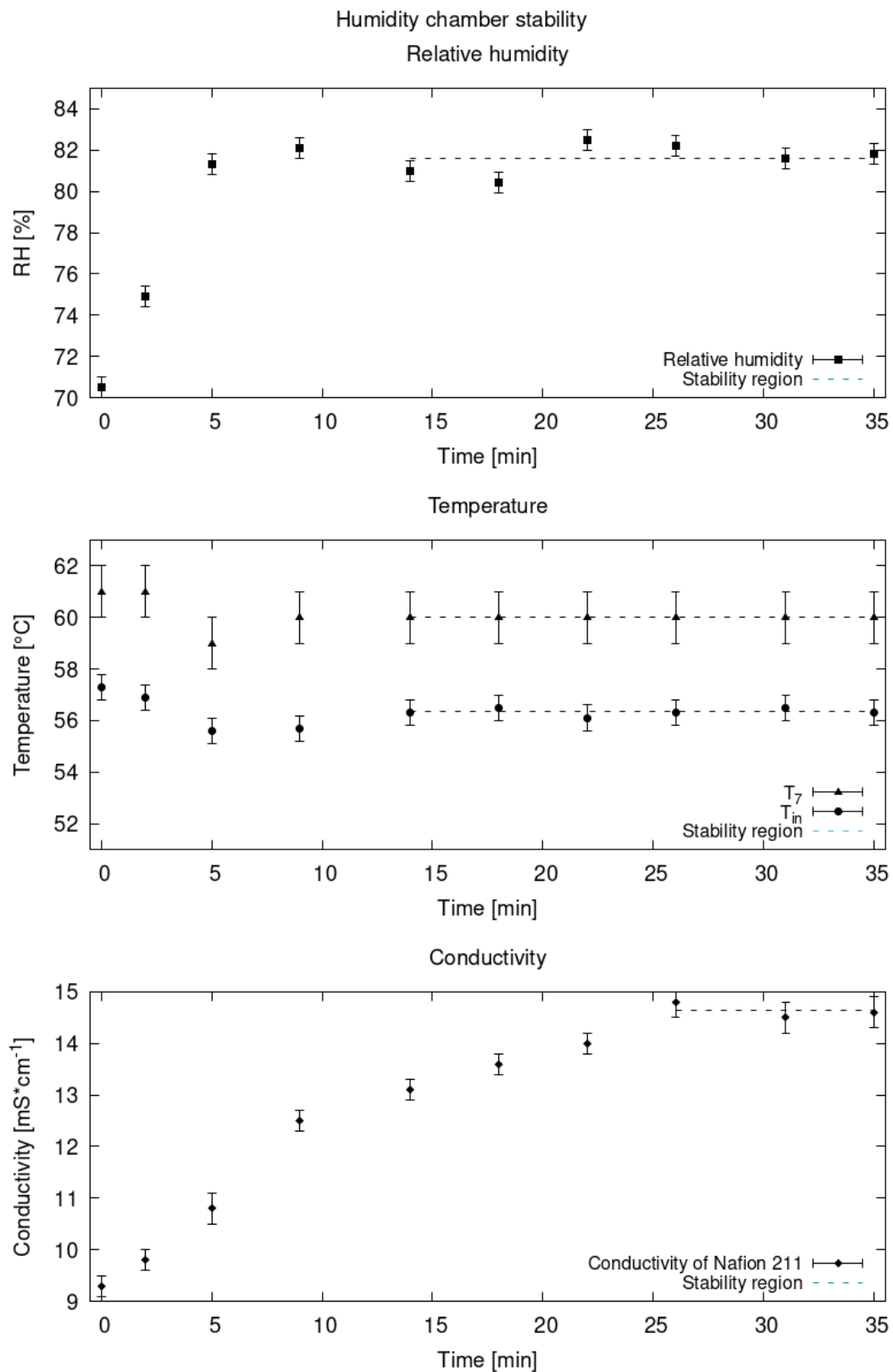
Figure 3.12: Stability of temperature, relative humidity, and conductivity measurement in the humidity chamber.
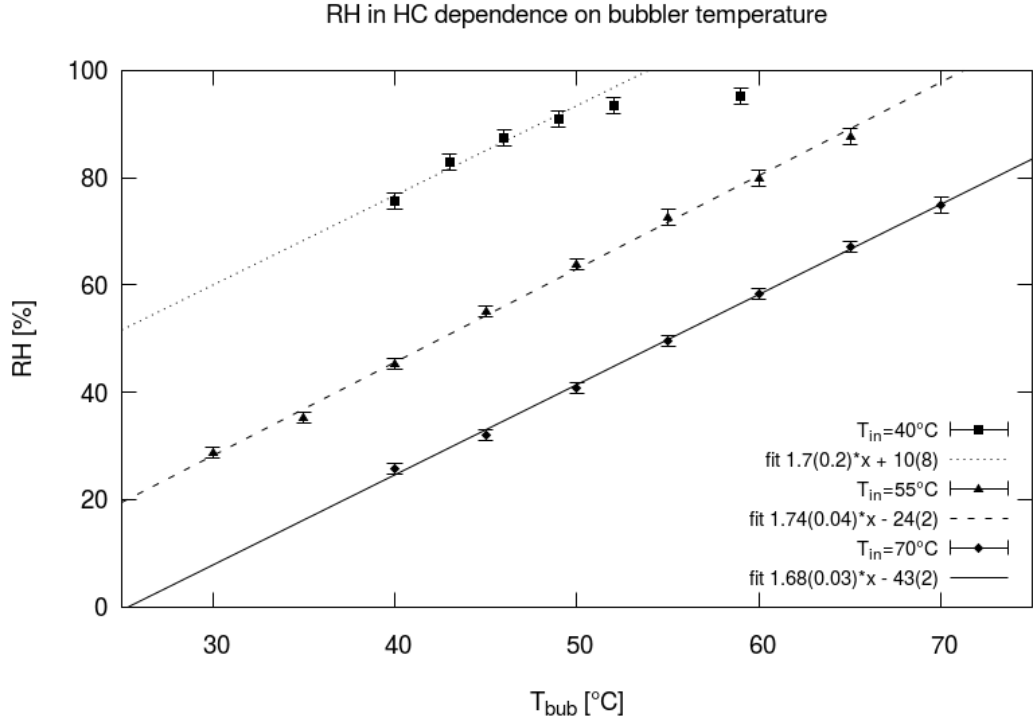
Figure 3.13: Dependence of RH inside the humidity chamber on bubbler temperature.

3.6.4 Geometric factors

In design of the electrode position, we have to take into account finite size of the sample when calculating the sample's resistance. Smits [1958] have described correction factors for using finite size sheet-like sample with finite thickness. The correction factor f_{11} can be seen in Figure 3.14. As the thickness to probe distance ratio approaches 0, the correction factor, used to multiply the measured resistance value, approaches unity. In our case we measure Nafion 212 membrane with thickness $t = 50.8\,\mu m$ and have chosen a probe distance of $s = 2.54\,mm$. For $f_1 1$ we then use formula

$$f_{11} = \frac{\ln(2)}{\ln\left[\frac{\sinh(t/s)}{\sinh(t/2s)}\right]}, \tag{3.2}$$

which for our values yields

$$f_{11} = 0.99993, \tag{3.3}$$

translating to $0.007\,\%$ lower value due to finite size sample. This is well bellow the error of measurement and was thus deemed negligible. Another source of error might arise from the size of the sample as a whole. We have chosen a rectangular sample with side size of $2.5\,cm$, which is roughly $10\times$ the distance probe, making any error arising from finite size of sample also negligible.

When Nafion is humidified, it increases size. Swelling of Nafion 212 has been well documented by Shi et al. [2016], showing that the swelling is almost isotropic

(swelling ratio of thickness to plane difference equal to 1.10) and is dependent on temperature. For the highest measured temperature (highest amount of swelling) of 80 °C, the swelling at 100 %RH has been less than 20 %. This change in size leading to change of correction factor is thus also negligible.
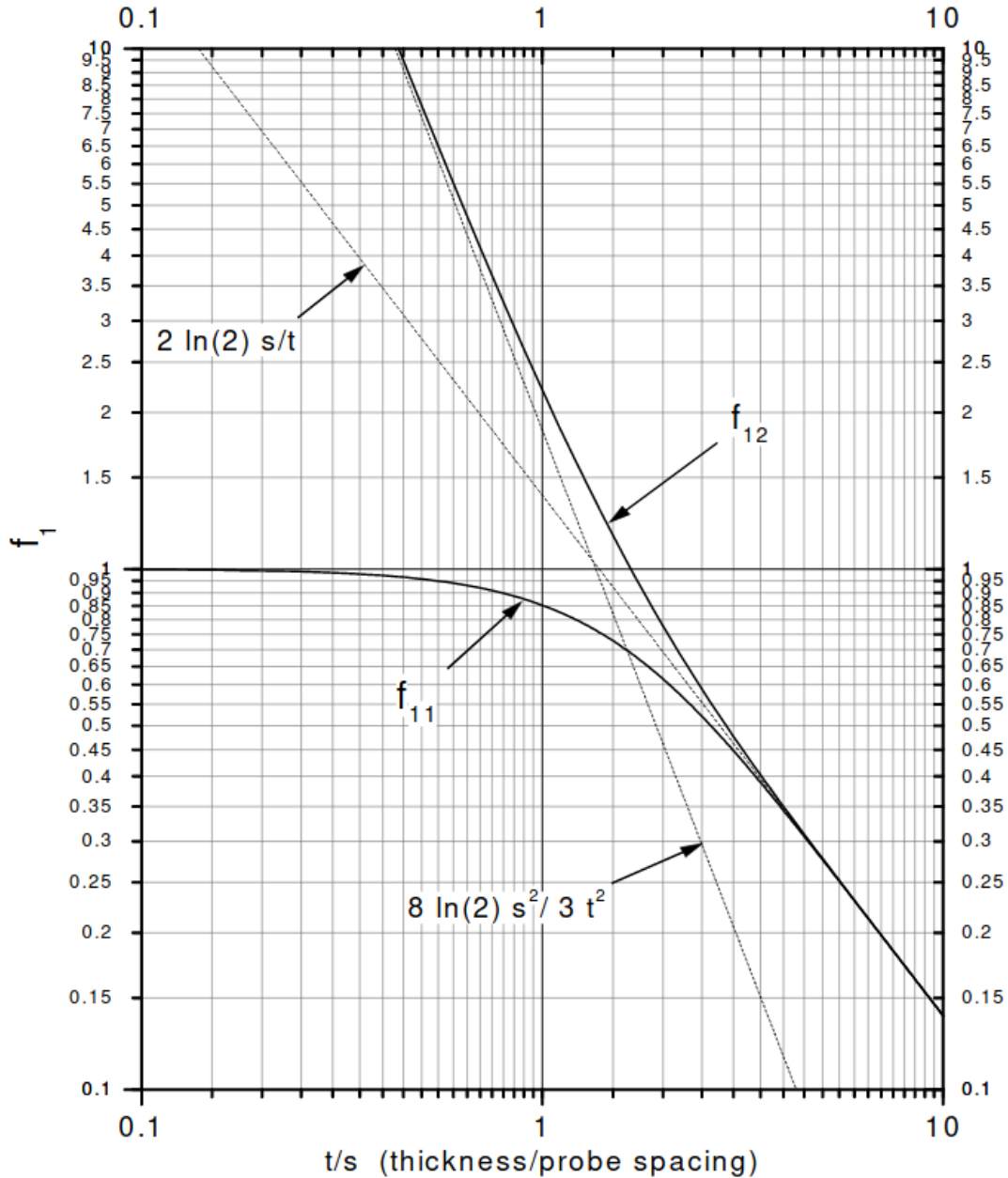
Figure 3.14: Correction factor for resistance measurement of a finite size sample using 4-probe measurement from Smits [1958]. f_{11} denotes sample on a non-conductive surface.

To verify reproducibility of measurement in the sample holder, we have done 10 repeated measurements of the same control sample - a rectangular sheet of steel. We have measured configurations shown in Figure 3.15, the resistance values can be seen in Table 3.2. As long as the sample was measured in the centre, the resistance value was within the error margin. The error for center position measurement was done by taking the sample out and putting it back in for every

sequential measurement, thus being a compound error of EIS measurement and the position of the sample inside the sample holder, which is not fixed. This has been repeated 10 times, leaving us with overall error of measurement equal to 1.8 %. This is the same error when measuring the steel sample without taking in out and reinserting into the sample holder 5 times, which yielded resistance value of $11.2(2)$ mΩ. This error is also equal to 1.8 %, indicating that the measurement of EIS in our sample holder is unaffected by repeated reinserting of the sample, if the conditions of measurement are the same. The measurement of misalignment has been inspired by the work of Thorsteinsson et al. [2009], who have calculated the allowable misalignment for microsamples.
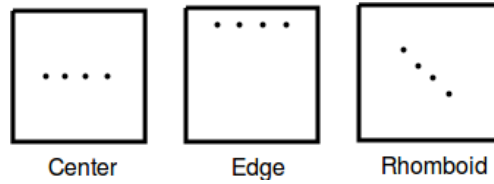
Figure 3.15: Different measuring configurations of electrode position.

Position	R [mΩ]
Center	11.1(2)
Rhomboid	11.0(2)
Edge	14.1(2)

Table 3.2: Dependence of measured resistance on electrode position.

Next, we tested the size of the sample for three different sizes, which can be seen in Figure 3.16. Our chosen size of the sample for all measurements was a rectangle with a side $a = 2.5$ cm. The results from repeated measurements for the various sample sizes can be seen in Table 3.3. As one would expect, larger samples have lower resistance. The difference in measurement between $A = 6.25$ cm^2 and $A = 4$ cm^2 is not explainable by the Equation 2.5 within the error of measurement, however we can see that the measurement is robust to preparation of the sample done by scissors and a measuring tape, as the difference is quite small. For the smallest sample, the Equation 2.5 doesn't hold.
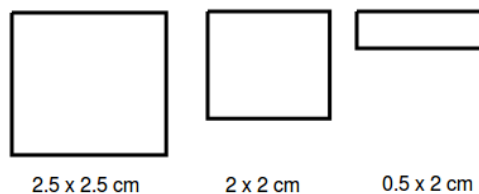
Figure 3.16: Measured sizes of sample.

3.7 Review

The construction of the humidity chamber was a success. We have shown that an autoclave chamber can be utilized into a humidity chamber, that can serve as

A [cm²]	R [mΩ]
6.25	11.1(2)
4	11.5(2)
1	24.2(3)

Table 3.3: Dependence of resistance on sample area.

a basis for a HCPEIS system. Let's start with the review of the requirements we had of the chamber before construction, described at the end of Chapter 3.2.

Temperature and RH levels are stable for the duration of EIS measurement. The system needs up to 1.5 h to achieve a balance depending on the desired temperature inside and then stays very stable. This has been the advantage of the larger volume of the chamber - all of the heatings, at bubbler and at the chamber, have a sawtooth pattern. They raise temperature until they hit a certain temperature deemed by the main regulator to be high enough. This inherently produces fluctuations in the system, however, thanks to the size of the system, these differences were not observed in sample temperature and were below the error of measurement for relative humidity.

The size of the system however had several disadvantages. First one was the long start-up time for high temperature measurements already mentioned. Another was a hysteresis of the system. If a change has been made to the measuring procedure, this could result in different conditions inside despite the same operating parameters as before the change.

An example of this is the refilling of water into the bubbler. This would mean rapid cooling down of the bubbler and thus lower relative humidity of the exiting nitrogen. Heating of this colder water takes time and the system may seem to be in balance. If the experimenter had not known, they might measure wrong values due to the hysteresis of the system. It is for these reasons that the system performs best if extra time is given to it to re-achieve equilibrium of all the heatings inside between measurements at certain temperature.

Condensation of water has been a great concern during the construction of the system. It is of utmost importance to prevent the gas carrying water droplets into the chamber. Several countermeasures were introduced into our system, which have made this issue non-existent. We were not able to prevent the condensation inside due to temperature differences of the inner surface of the chamber. Critical areas were around the lid of the chamber, where insulation is difficult. After the measurement, water droplets could be found at these areas of the chamber. Despite this, stable levels of relative humidity inside the chamber were achievable up to 90 %RH. Above this level, the stability of RH was dependent on other factors, but mostly on temperature. Again, the size of the system prevented the droplets from disturbing the balance inside the system.

Regarding the speed of measurement, it can be seen in Figure 3.12, that water absorption of the membrane takes more time than achieving equilibrium when following the measuring protocols. There is much longer time spent before the measurement to allow the system to establish an equilibrium. Despite this, once the measuring starts, the absorption of water is the most time consuming process and thus we have marked this requirement also as passed.

Since drying out of membranes was measured as more time consuming, we have demanded no overshoot. This would also be important when measuring Nafion at the end of the temperature range and low humidity, as drastic drying out of the membrane could damage it. The main control unit, consisting of PID regulators, has had a hard limit to not to overshoot the operating parameters. Again, the size of the system makes it resistant to sudden spikes of heatings. Overshooting of either temperature or RH levels has never been a problem during measurements.

When it comes to reproducibility, the chosen semi-spherical probes did not tear the membrane. Constant pressure applied to the membrane is inherent in the design of the sample holder. Choosing the same operating parameters led to the same conditions inside upon repeated measurement.

An improvement of the system would be to decrease the temperature gradient inside. At the current size, a fan enforcing gas circulation inside might be an improvement. Another approach might be construction of heat conducting scaffolding inside. A smaller chamber might eliminate the need for such improvements, losing less heat and making it easier for commercially available heaters to heat it uniformly.

4. Membrane conductivity

After completion and testing of the humidity chamber, the goal was to measure in-plane EIS measurements of etched membranes. We have first tested the measuring process with a standard screw design holder with 4 Pt wires on Nafion 115, as it was the configuration best comparable with the available literature. These measurements have served as a confirmation of a successful completion of the measuring system and were followed by measurements with our sample holder on Nafion 211 and Nafion 212 as a test of the new sample holder and electrodes. The final part were the measurements of etched Nafion 212 under the same conditions as it's untreated counterpart and a comparison of their performance.

4.1   Nafion 115

We first start with the testing of Nafion 115 inside the completed chamber with the standard sample holder setup that can be found in the literature: the screw design as seen in Figure 3.4. As electrodes, 4 Pt wires with the diameter of $1\,mm$ have been used with $1\,cm$ of the wires in contact with the membrane. The purpose of this experiment was to achieve comparable results as found in the literature.

We have compared our measurement of Nyquist plot of Nafion 115 with the results obtained by Xie et al. [2006], shown in Figure 4.1. They measured Nafion at full humidification and room temperature with different electrode distances. The series are marked $4P$ for 4-probe method and $0.4\,S$, $1.6\,S$, and $2.7\,S$, where S denotes using platinum strips and the number denotes the distance between electrodes in cm. We have recreated this measurement in Figure 4.2, measuring Nafion 115 at $T = 25.5\,°C$ and $RH = 96\,\%$. The high frequency part of the plot was not measured due to unavailability of a potentiostat at the time that could achieve these high frequencies.

The distance of electrodes in our sample holder was $L = 1.27\,cm$. This can be compared to the $1.6\,S$ series the best. Their result can be estimated from the graph to be roughly $R = 1500\,\Omega$. We have extrapolated our result to be $R_{measured} = 1900\,\Omega$. If we use equation 2.6, we can normalize our measurement to arrive at $R_{norm} = R_{measured}/\frac{1.6}{1.27} \approx 1508\,\Omega$. This is well within the error caused by guessing the value measured by Xie and their group from their figure and guessing their sample size. Thus we have concluded that our setup works well when compared to results found in literature.

4.2   Nafion 211

We have shown that the measuring yields results comparable with literature when using the standard measuring set-up. It has been our target however to test measurement using our design. Since we wanted to measure etched Nafion 212, Nafion 211 has been chosen as our comparison to Nafion 212. It has the advantage of having the same structure, but half the thickness (according to DuPont 1 mil or $25.4\,\mu m$ for Nafion 211 and 2 mil or $50.8\,\mu m$ for Nafion 212).

Example of these measured spectra can be seen in Figure 4.3. It is visible
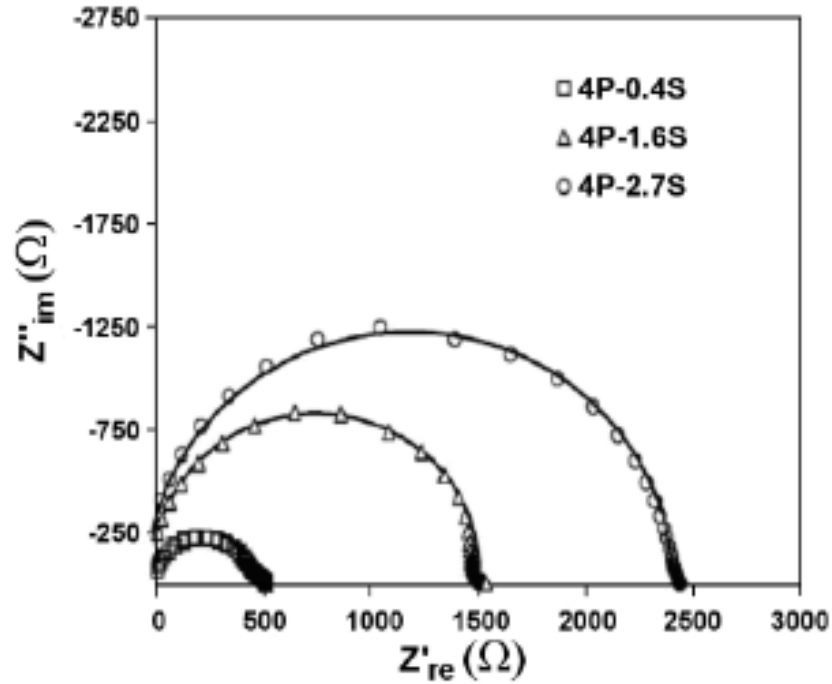
Figure 4.1: Nafion 115 EIS measurement at full humidification and room temperature by Xie et al. [2006].
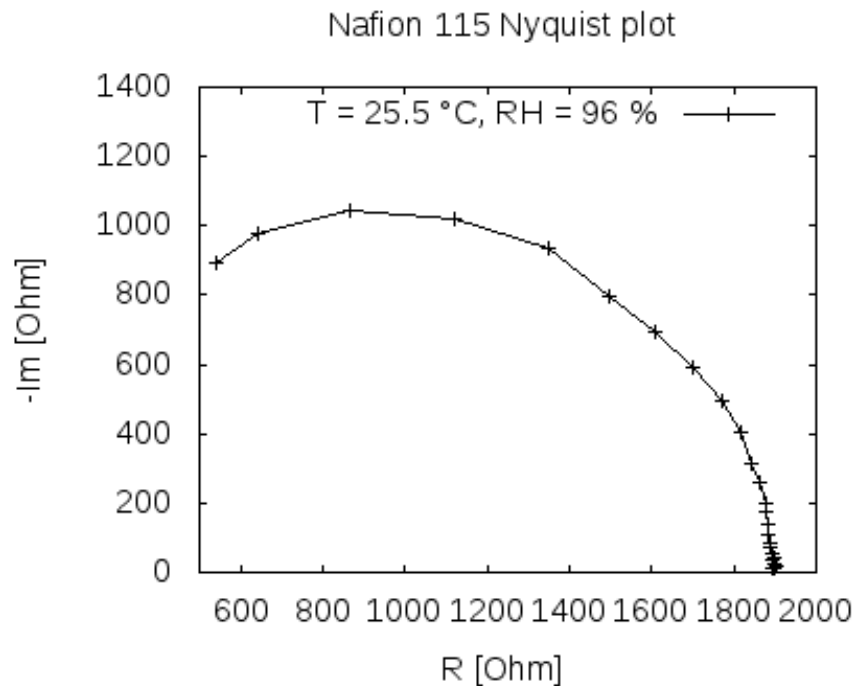
Figure 4.2: Our measurement of Nafion 115 at $RH = 96\,\%$ and $T = 25.5\,°\text{C}$.

that measuring Nafion 211 with the new electrodes yields good measuring results in terms of the shape of the curve. There is however one visible fault - negative resistance. The reason why and how it impacts measured results is discussed in detail in Chapter 4.5. The resistance value of these measurements was taken in the same way as for the regular measurements - the low frequency intercept. De-

spite these surprising results, the measured conductivity dependence on RH was very well exponential as expected, as can be seen in Figure 4.4. When compared to Nafion 212 measured under the same conditions, we have found the results very well comparable. The values measured for Nafion 211 were comparable to literature such as Peron et al. [2010] or Li et al. [2010]. The higher performance of the thinner Nafion 211 is also in accordance with theory, as has been experimentally demonstrated by Liu et al. [2012]. Based on these findings, we have decided to continue with the measurements with these electrodes.
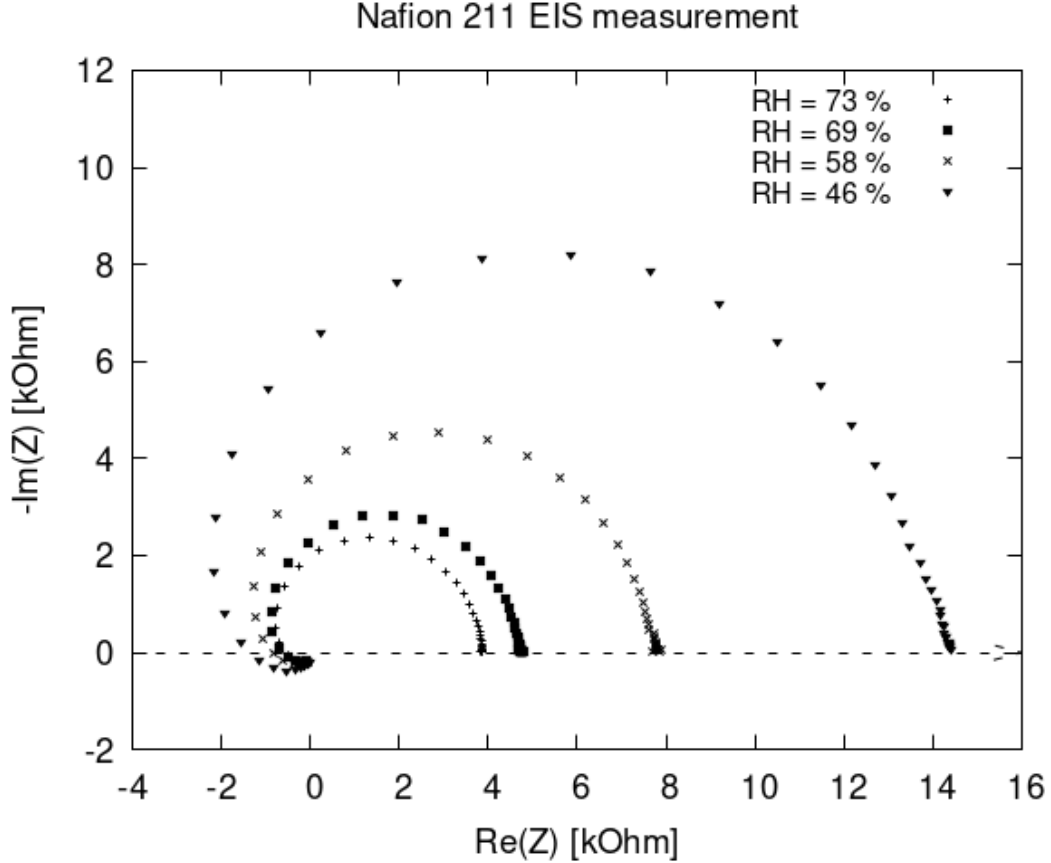
Figure 4.3: Nafion 211 Nyquist spectra at $T = 40\,°\text{C}$.

It is also of note, that the linear fits have comparable trend lines (for linear fit $ax + b$ Nafion 211 has a trend-line with slope $a_{211} = 0.0127$ and Nafion 212 has $a_{212} = 0.0114$, meaning the slopes are within $9\,\%$ error of each other). Before we continued, we also compared the Nafion 212 measured values with literature. For our temperature range, the best described measurement of Nafion 212 conductivity dependence on RH we have found were done by Feng et al. [2018]. Their graph can be seen in Figure 4.5. It has been measured at various temperatures, with the green line with square points at $30\,°\text{C}$ being most comparable to our data. We can see that the values of conductivity measured by Feng et al. [2018] in Figure 4.5 around $RH = 70\,\%$ are $\approx 10.5\,\text{mS}\,\text{cm}^{-1}$, which matches our results well.

It is of note, that it is possible to find Nafion 212 conductivity values measured in literature with quite different results when compared to ours, such as Wang et al. [2012a] which can be seen in Figure 4.6, where Nafion 212 conductivity
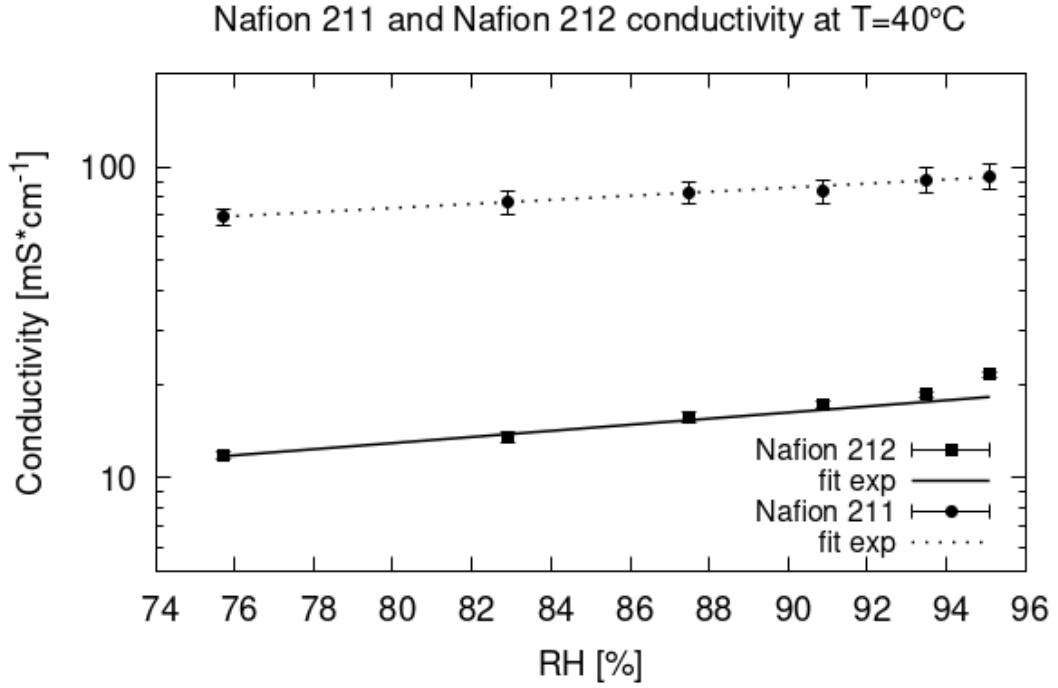
Figure 4.4: Nafion 211 and Nafion 212 conductivity at $T = 40\,°\mathrm{C}$.
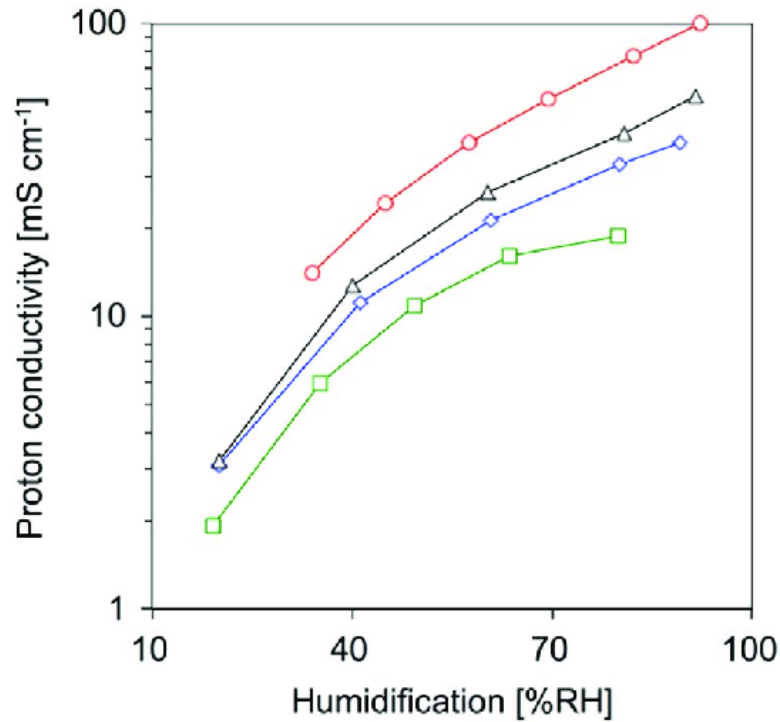
Figure 4.5: Nafion 212 conductivity at different temperatures, measured by Feng et al. [2018]. $\square : T = 30\,°\mathrm{C}$, $\diamond : T = 60\,°\mathrm{C}$, $\triangle : T = 80\,°\mathrm{C}$, $\circ : T = 120\,°\mathrm{C}$.

is roughly one order of magnitude larger than ours. The methods are well described in this article, with the authors using 4-probe method and calculating the conductivity using the same equation (Equation 2.6) as us. Due to the in-depth description, these results are the best comparison to our work. An explanation of

the difference of conductivity magnitude in these measurements will be examined in the following chapters.
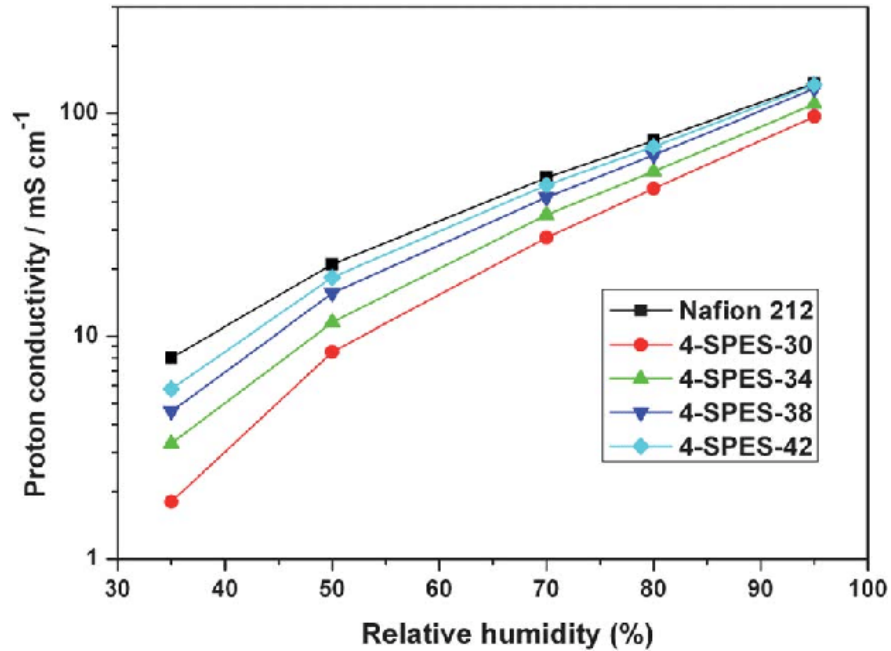
Figure 4.6: Nafion 212 conductivity at $T = 80\,°C$ measured by Wang et al. [2012b].

4.3 Review of etched membranes

We have proved that the system is able to measure the conductivity of Nafion 212 in the previous section. The reason for the construction of this system was however to try and measure in-plane conductivity of etched membranes created at our department. Firstly, let's investigate the motivation for etching membranes.

As mentioned in the beginning of this work, one of the obstacles to widespread usage of fuel cells is their price. One of the most expensive parts of a fuel cell is the catalyst, for which typically platinum is used. Since platinum is very expensive, researchers try to create a catalyst with comparable performance, but lower amount of platinum. A common approach is to use carbon supported Pt nanoparticles. The many possibilities of creating low Pt catalyst layers are summarised very well in Yakovlev et al. [2019]. In this work, magnetron is used to sputter very thin layers of platinum with high active surface area (shown by Tian et al. [2011]).

The proposed solution is to use magnetron to etch the membrane, creating large active surface area. The etching is controlled by depositing CeO_2, which acts as a mask, protecting areas with deposited cerium oxide from etching. CeO_2 also increases chemical stability and durability of the membrane, as shown by Wang et al. [2013]. The membrane is then sputtered with Pt, completing the process. Sputtering the catalyst layer directly on the membrane decreases ohmic losses and eliminates the need to introduce carbon as a support to the system. SEM images of the surface structure of an etched membrane can be seen in Figure 4.7.
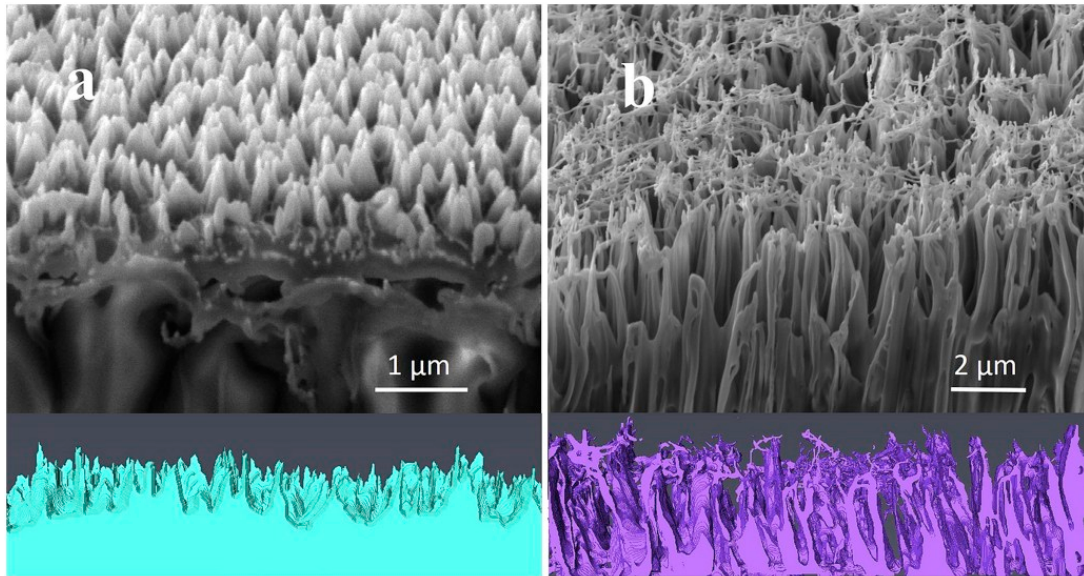
Figure 4.7: SEM micrographs of the cross-sectional morphology of Nafion 212 after CeO$_2$ treatment in Ar + O$_2$ atmosphere and in-scale 3D models: 7 min (a) and 70 min (b). Figure taken from Yakovlev et al. [2019].

Etching has been shown to chemically change the surface of the membrane. Proton conductivity reduction has been reported by Lue et al. [2007], using Nafion 117 and other PFSA membranes. Alongside with conductivity reduction after treatment, lowering of surface hydrophobicity of the etched surface has been reported, both by Lue et al. [2007] and Ramdutt et al. [2007]. This loss of hydrophobicity is thought to arise from reduction of fluorine on surface of the membrane. Both Lue et al. [2007] and Ramdutt et al. [2007] reported dependence of proton conductivity of the treated membrane is highly dependent on the magnetron power and the length of treatment, with higher power or longer treatment leading to lower proton conductivity.

It is interesting to note that Bae et al. [2006] also reported slight increase in proton conductivity after short, low power treatment of a membrane, attributed to higher surface hydrophilicity due to oxygen deposition and resulting chemical change of the surface. The decrease of conductivity performance after long, high magnetron power treatment was attributed by the authors to the loss of content of sulfonic groups and cross-linking between the polymer backbones of Nafion. The authors have also shown that etching of the membrane doesn't change structure or chemical properties of the membrane's bulk, however the surface changes still lead to drastic changes in conductivity.

Ramdutt et al. [2007] also reported weak adhesion to electrodes of treated membranes, resulting in poor conductivity measurement performance. They also found some bonding taking place between the membrane and electrodes, which has been found to take place only when using plasma treated membrane. This bonding has been described as drastically decreasing performance.

4.4 Measurement of etched membranes

All of the measured etched membranes in this work were Nafion 212. Because of this, Nafion 212 was measured for comparison of the changed performance. The measurement for all membranes was done at three temperatures of the sample ($T_1 = 40\,°\mathrm{C}$, $T_2 = 55\,°\mathrm{C}$, and $T_3 = 70\,°\mathrm{C}$), while changing the bubbler temperature. The step of bubbler temperature was $T_{step} = 5\,°\mathrm{C}$, resulting in changing RH levels inside the chamber. All RH levels achievable by the chamber were measured, starting from $T_{bub} = 30\,°\mathrm{C}$ and being limited by the power of the heating at $T_{bubmax} = 85\,°\mathrm{C}$.

Upon setting new temperatures of the heatings, the membrane was left for 20 min to achieve equilibrium with the surrounding humidified nitrogen. After this time, EIS measurements were performed within 5 min intervals. If three consecutive measurements were within the error of EIS measurement, the value was noted and new bubbler heating temperature was set. Additional water was filled into the bubbler between changing inside temperature of the chamber in order to not disturb the RH balance inside. The raising of temperature inside the chamber and cooling of the bubbler took up to 1 h.

We have started with the measurements of Nafion 212 membranes etched in CeO_2 atmosphere for 70 min, as described in Yakovlev et al. [2019]. First, the etched side up (in contact with electrodes) was measured at $T_7 = 40\,°\mathrm{C}$, yielding the Nyquist plot visible in Figure 4.8. Orientation up means that the etched side was in contact with the electrodes, orientation down would be the non-etched backside of the membrane in contact with the electrodes. It is clear that this measurement is non-interpretable. Repeated measurements of the membrane etched with cerium oxide yielded no better results. To the contrary, the more measurements were done, the less interpretable the Nyquist plots got. The sample was then remeasured at RH levels up to $RH = 95\,\%$ with no better results.

We then measured the non-etched side of the membrane, again, yielding no interpretable results. Only other partially successful measurement was achieved using 2-probe method. The measured Nyquist plot is shown in Figure 4.9. The resistance was in the order of mega ohms, despite the system being at $RH > 70\,\%$. From this graph we can however see, that the measured values seem to resemble the semicircle characteristic of membrane EIS measurement with heavy noise. The noise seems to have oscillatory, non-harmonious behaviour. These oscillations turned out to be random and mostly in the range of $-50\,\mathrm{mV}$ to $50\,\mathrm{mV}$. The oscillations rarely achieved higher values.

The only viable explanation for this behaviour found by us was that due to chemical reactions between the etched Nafion and the electrodes, small galvanic potential was created. This could be caused by the electrodes being gold-plated copper and brass, with humidified Nafion acting as electrolyte. Upon further inspection, we have found that the probes have degraded, which we will described in the following section. The measurements of Nafion 212 etched in cerium oxide have not yielded any successful results, despite repeated attempts.
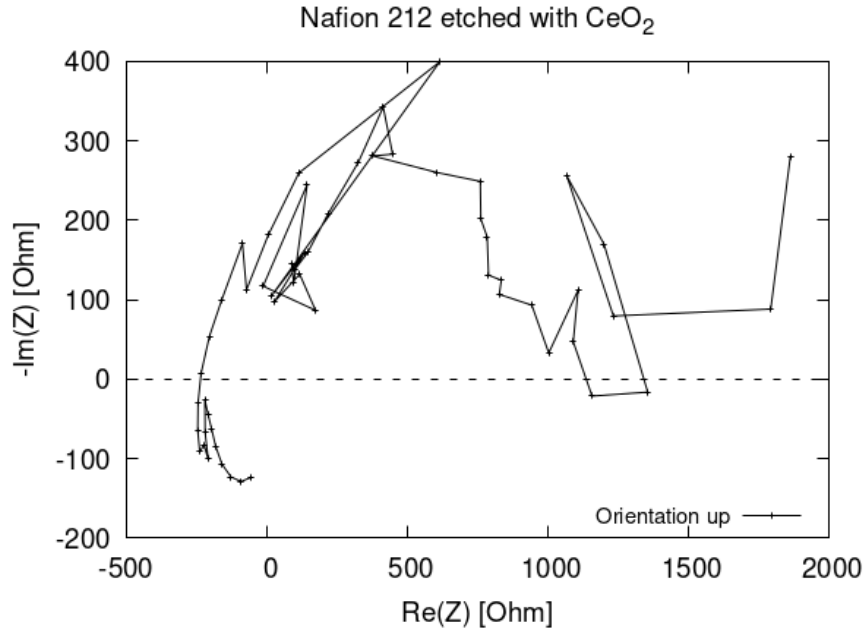
Figure 4.8: Nyquist plot of the first measurement of etched Nafion 212 at $T = 40\,°C$.
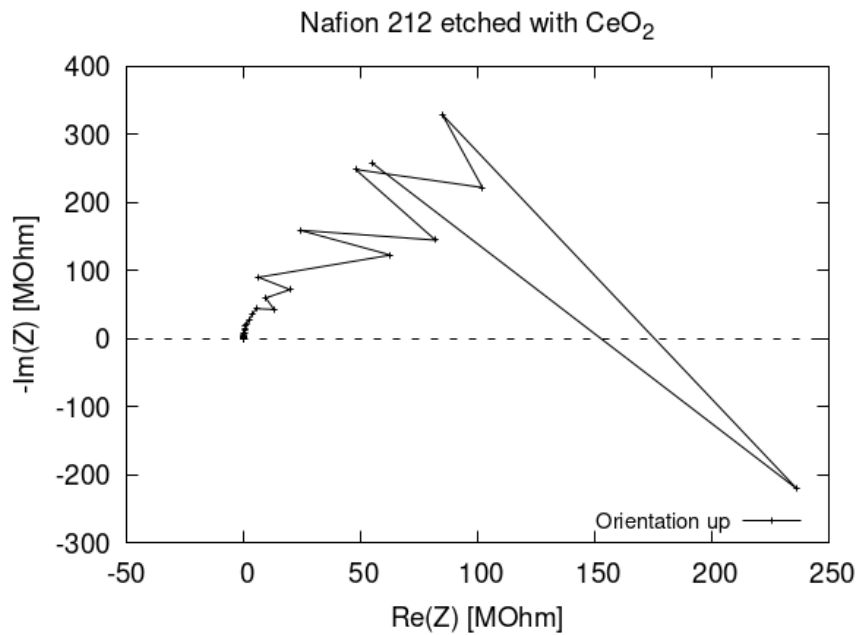
Figure 4.9: Nyquist plot of etched Nafion 212 at $T = 40\,°C$ using 2-probe method.

4.5 Electrodes decomposition

When changing samples after measurement, we have noticed leftover material on the Nafion membrane. We have used optical microscope with 32x magnification, to look at the material in more detail. The membrane after measurement can be see in Figure 4.10, where the probes have left marks on the membrane. Near the right mark, a piece of what visually appears to be gold can be seen.

The electrodes themselves were visibly degraded, as is shown in Figure 4.13.
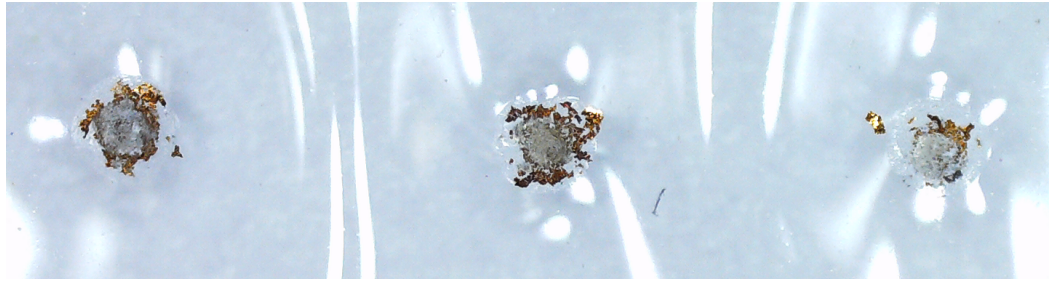
Figure 4.10: Etched Nafion 212 after measurement showing signs of residual material from the electrode.
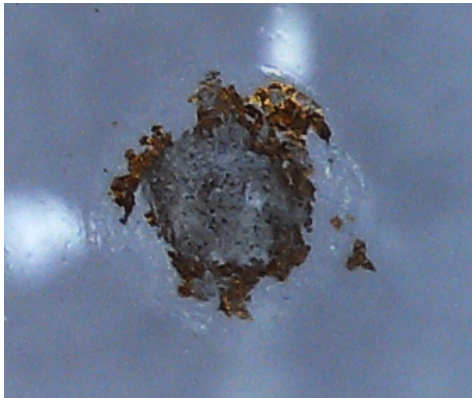
Figure 4.11: Detail of the left mark.
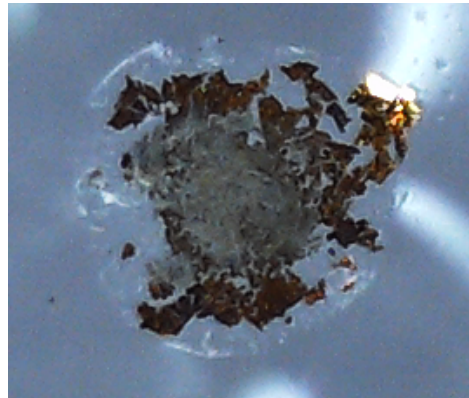
Figure 4.12: Detail of the center mark.

The gold plating has degraded and chipped off onto the membrane, exposing the copper underneath. Red and bluish grey material can be seen with the eye, indicating copper oxides creation (Richardson [2000]). Creation of copper hydroxides is also possible. All of these compounds are either semi-conductive or non-conductive, which would explain poor EIS performance. The probes were further investigated using SEM, which can be seen in Figure 4.14. Here we can see the area where the copper was exposed and that some material is attached to the tip of the probe. From the backscattering image on the right side of Figure 4.14, we can see that this attached material is lighter than both the copper and gold.
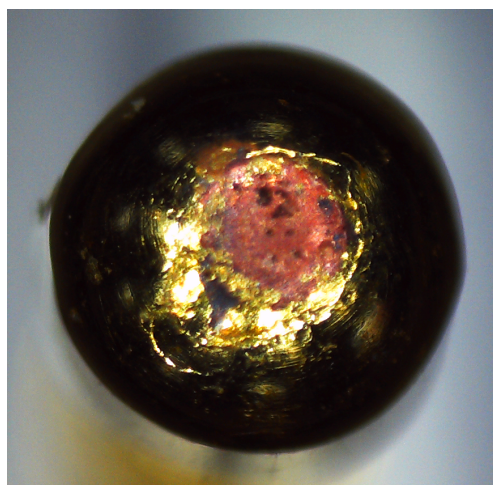
Figure 4.13: Detail of the electrode after measurement of Nafion 212 etched in CeO$_2$.

SEM HV: 10.0 kV

WD: 13.96 mm

View field: 1.80 mm

Det: SE, BSE

1 mm

SEM MAG: 231 x

Peter Kus

MIRA3 TESCAN

Performance in nanospace
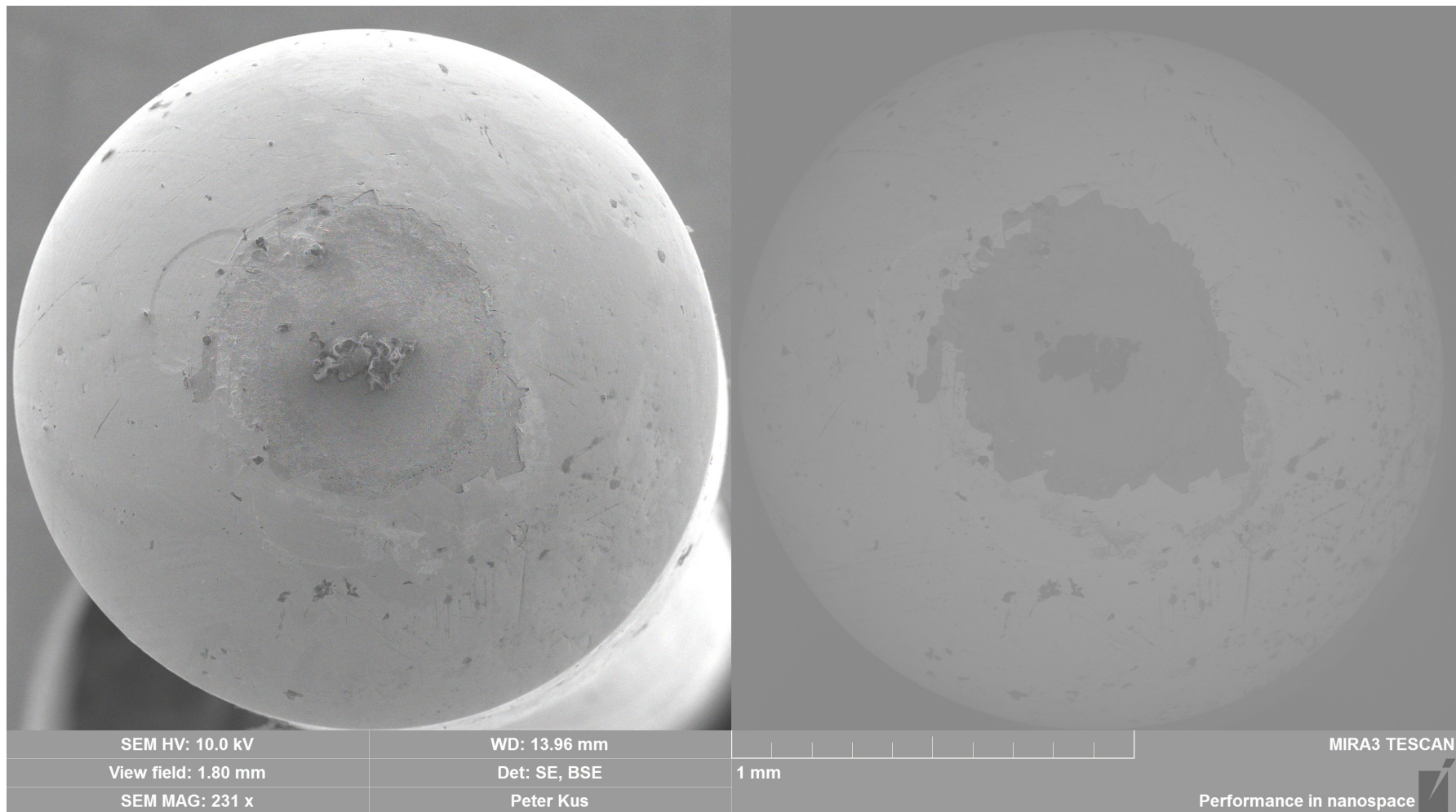
Figure 4.14: Detail of electrode after measurement of Nafion 212 etched in CeO$_2$ in SEM. SE image on the left, BSE image on the right.

The electrode was further investigated using EDX. The results of the measurements can be seen in figure 4.15. The probe consisted of copper and gold, as would be expected. We have also found peaks corresponding to sulfur, carbon, and fluorine. These indicate that the material attached to the tip is Nafion. This is supported by EDX mapping shown in Figure 4.16, where the exposed copper is very well visible, as well as large concentration of carbon at the position of the attached material.
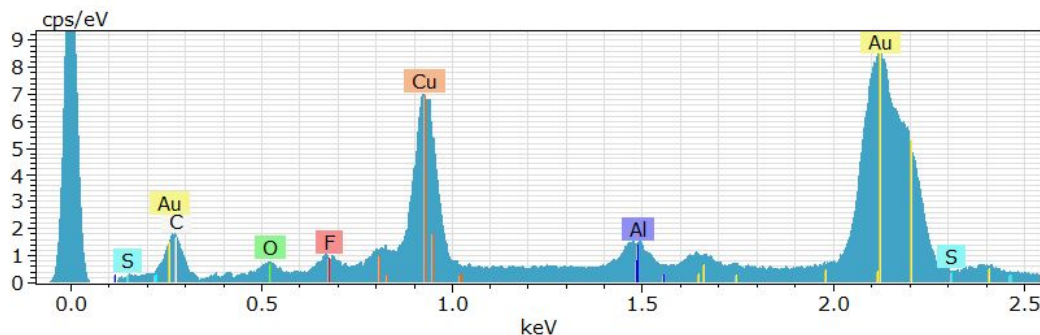
Figure 4.15: Probe composition after measurement.

In Figure 4.17 we can see SEM image of the surface of the Nafion 212 etched in CeO_2. A change of the surface can be seen in the area where the tip was in contact with membrane, as well as pieces of gold plating and other material from the probe that fell onto the membrane. In the same way we have then used the probes to measure non-etched Nafion 212, which can be seen in Figure 4.18. Here, the surface change of Nafion was not as drastic, however, the residual material from the probe is also visible here.

Our findings are comparable with those of Ramdutt et al. [2007], who have also used gold plated copper probes. We have demonstrated that on etched membranes, the gold plating of the probes degrades and the subsequent creation of non-conductive oxides on the surface of the probe leads to bad contact between the probe and the membrane, eventually rendering EIS measurement impossible. We have also found indications of structural changes of the surface of the membranes. Drastic performance decrease as reported in Ramdutt et al. [2007] was also in line with our findings.

The attached material on the electrodes and the surface formation of the non conductive compounds has disallowed measurement of etched membranes even on their non-etched side. For the measurement of etched membranes, pure platinum probes would be probably a better choice. We have also found better performance of 2-probe measurement with the etched membrane, despite it having worse performance than 4-probe method for all our other measurements.

As to the reason of degradation, our theory is that the electrode degradation is due to chemical reactions with radicals formed at the membrane. Nafion membranes form radicals even as they degrade during runtime in fuel cells, as described in Frühwirt et al. [2020]. Etching of the membrane has a very drastic influence on the chemical structure, leading to breaking of chemical bonds, as shown by Schulze et al. [1999], and can be likened to a more rapid degradation. We hypothesize that these broken bonds lead to creating radicals, that cause the subsequent degradation of the electrodes. We have, however, no way to further
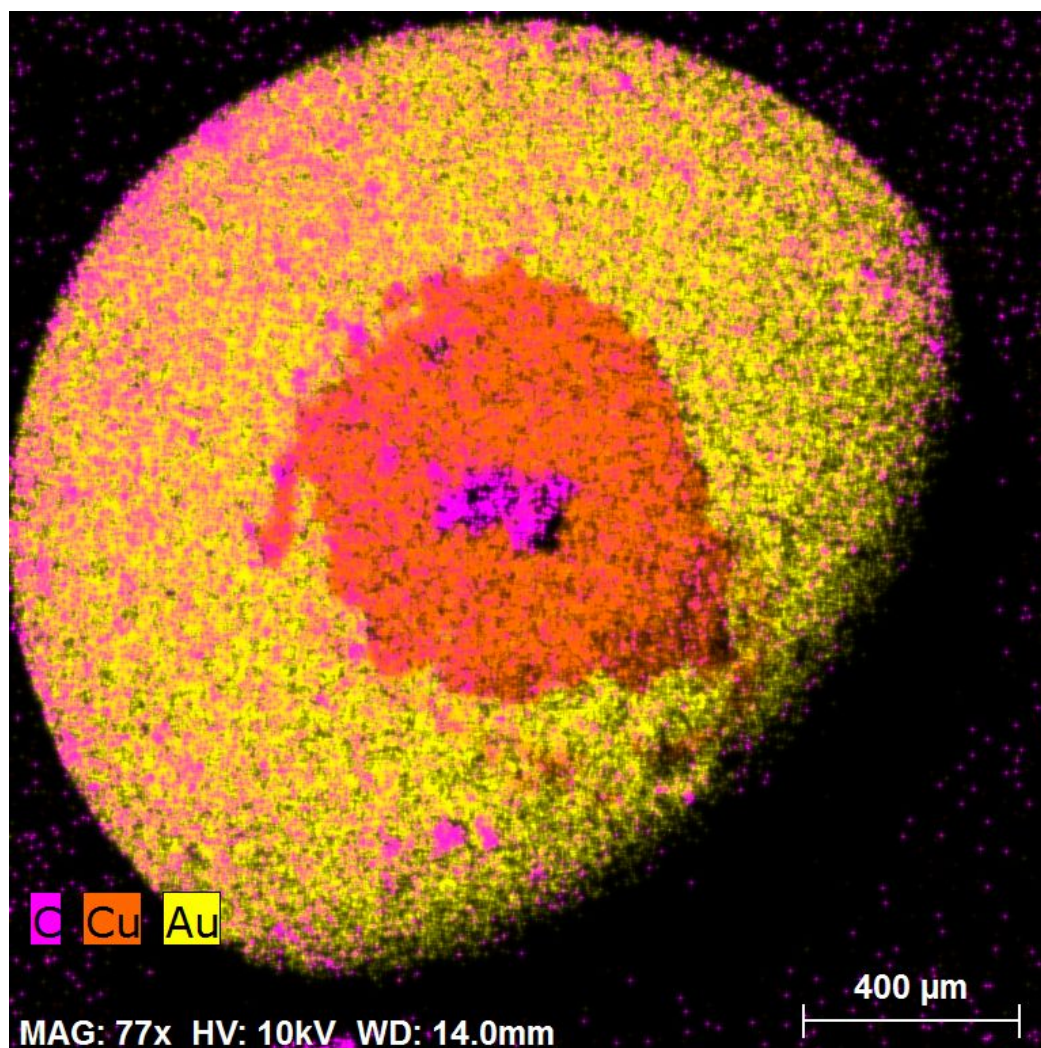
Figure 4.16: EDX map of probe after measurement.

investigate this.

4.6 Measurement of etched membranes with Pt

As was described in the review section, the membrane etched in cerium oxide is then sputtered with Pt, which should promote surface conductivity. The membranes were etched the same way as in the previous section - 70 min etching in CeO$_2$ as described in Yakovlev et al. [2019]. 5 nm of Pt were then sputtered onto the etched membrane.

The probes have been exchanged for new ones, although of the same type for the measurement. In the up orientation, the Nyquist plots were, yet again, non-interpretable. An example of the measured Nyquist plots can be seen in Figure 4.19. Despite the fact that the curves were not of the proper semicircular shapes, the overall resistance was very low - indicating that the platinum on surface may have contributed towards higher conductivity.

In the down orientation however, the measurements yielded good Nyquist plots. Nafion 212 etched in CeO$_2$ with 5 nm Pt will be in this work from now on called etched Nafion 212 to make it easier to write out. The etched Nafion

SEM HV: 10.0 kV	WD: 15.07 mm
View field: 1000 µm	Det: SE, BSE
SEM MAG: 415 x	Peter Kus
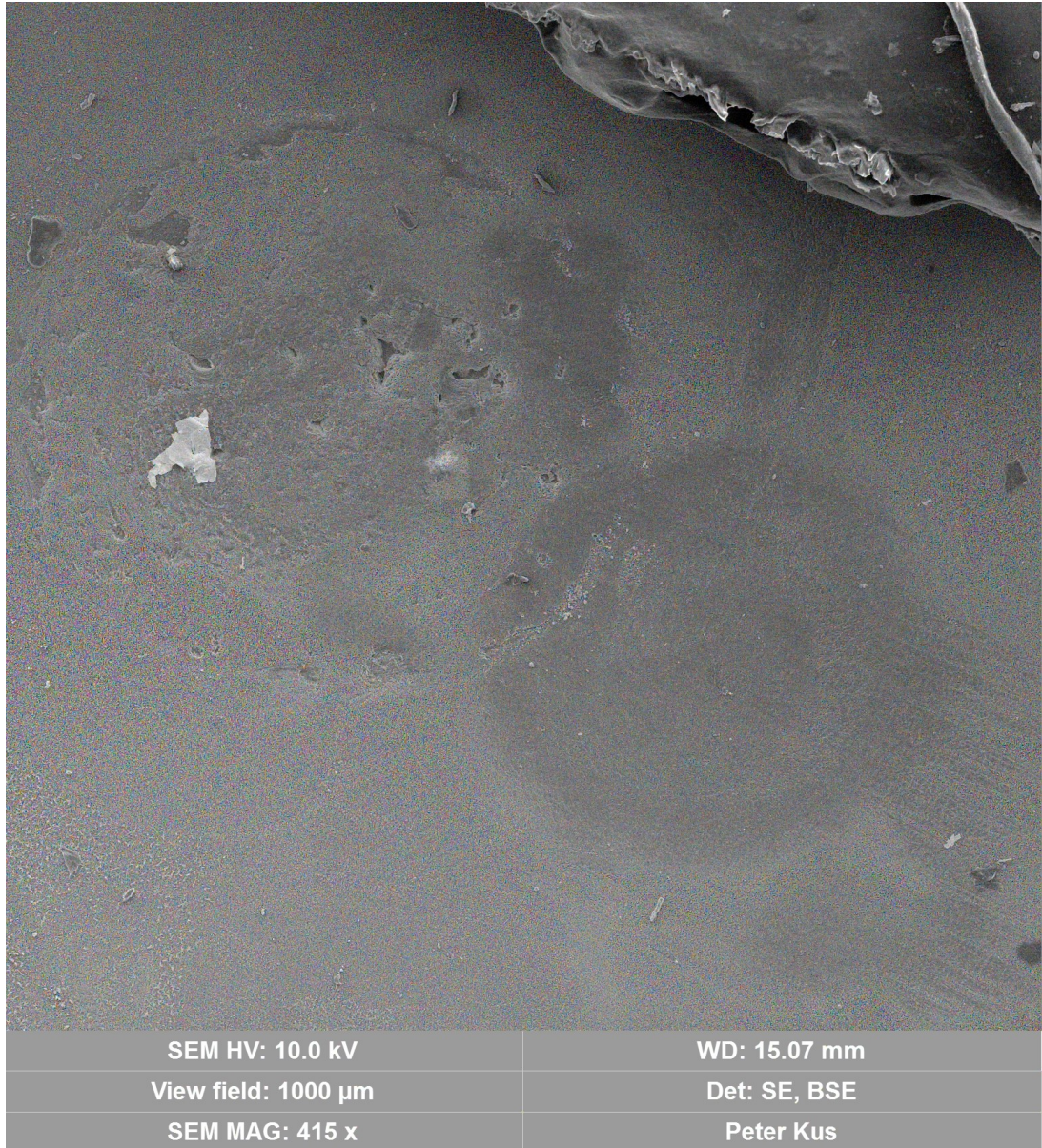
Figure 4.17: SEM imaging of etched membrane after measurement.

SEM HV: 10.0 kV	WD: 14.92 mm
View field: 1000 μm	Det: SE, BSE
SEM MAG: 415 x	Peter Kus
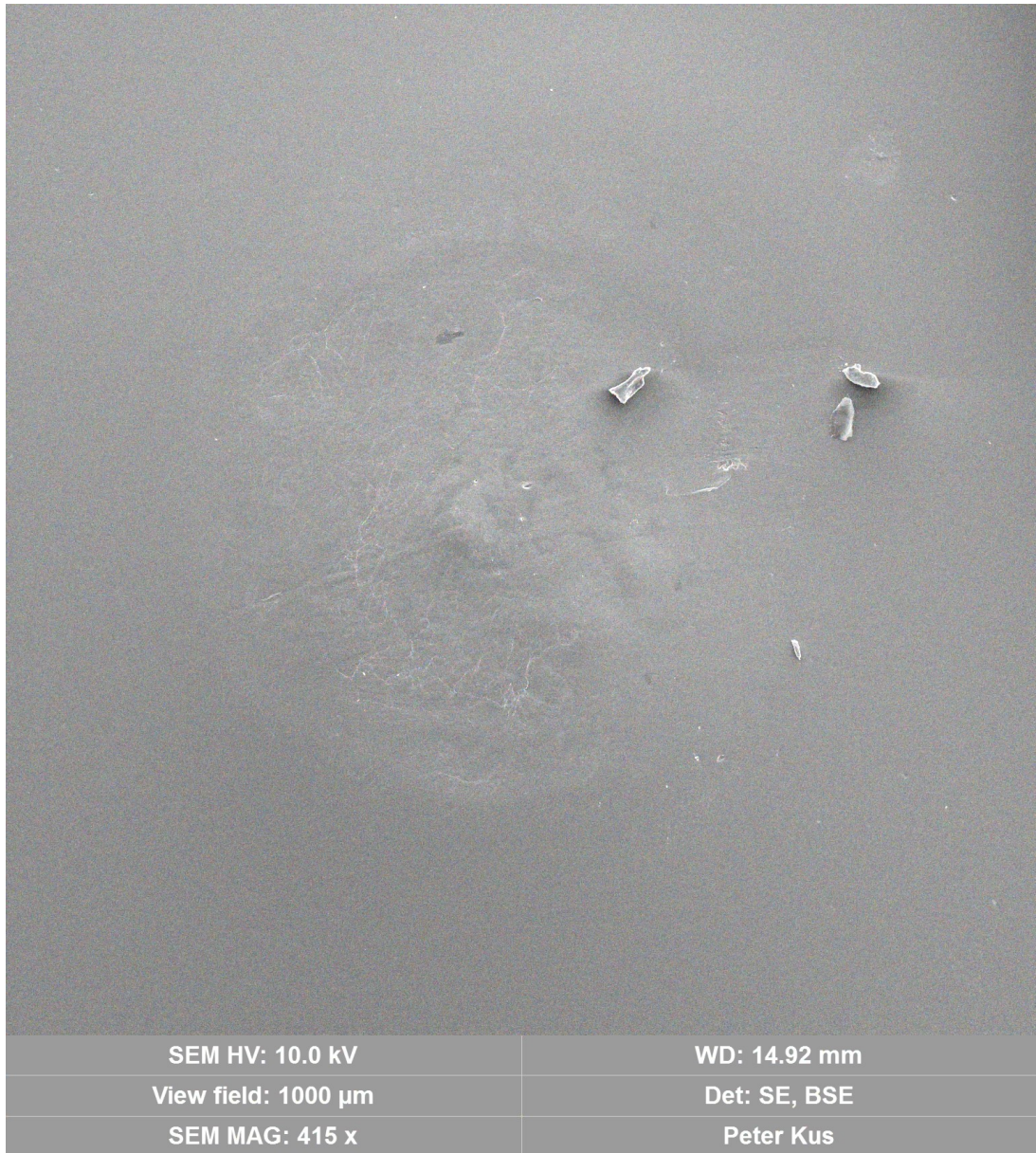
Figure 4.18: SEM imaging of Nafion 212 after measurement.
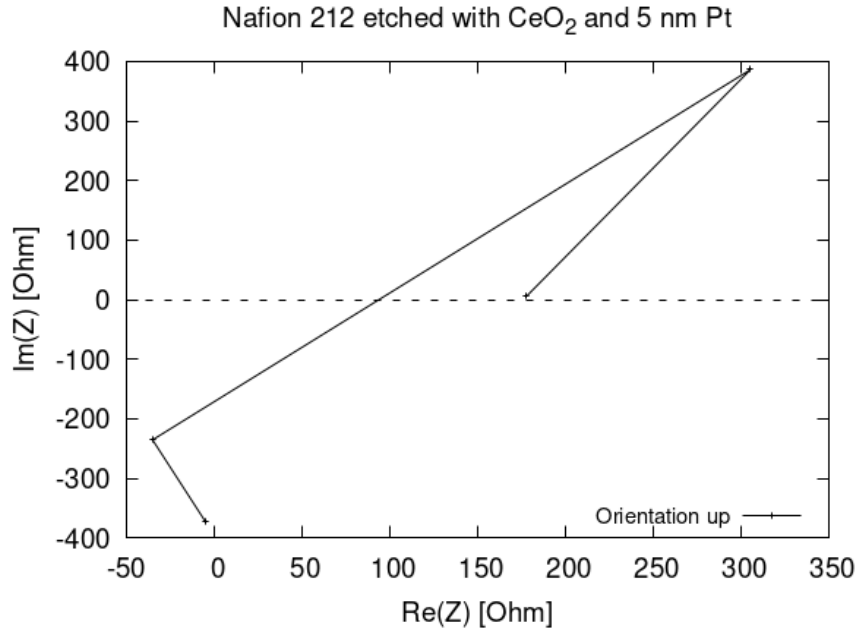
Figure 4.19: Our measurement of Nafion 212 etched with CeO_2 and $5\,nm$ Pt at $T = 40\,°C$.

212 could not be measured at $T_7 = 40\,°C$, however, at higher temperatures, the measurement in the down orientation yielded good Nyquist plots, such as in Figure 4.20.

Before we get to the etched Nafion 212 measurements, let's shortly review the baseline measurements of Nafion 212. The high RH region at low temperature inside the chamber is shown in Figure 4.21. We can see that the behaviour is very well described by the exponential fit apart from the high RH region.

The measurement of Nafion 212 at $T_7 = 55\,°C$ and $T_7 = 70\,°C$ can be seen in Figure 4.22. The conductivity is yet again well described by an exponential fit, with the exception of the low RH region, where conductivity drops off. The higher temperature conductivity has overall lower value, but rises faster with rising RH. In Figure 4.23 we can see the equivalent of this graph for etched Nafion 212. It is clear that etched Nafion 212 has higher overall conductivity and very similar behaviour when it comes to the difference between $T_7 = 55\,°C$ and $T_7 = 70\,°C$ curves, as well as the slope of the exponential fit.

In Figure 4.24 we can see the comparison between etched and non etched Nafion 212 at $T_7 = 55\,°C$, with the etched Nafion 212 clearly having higher performance conductivity wise. The same situation can be seen in Figure 4.25 at $T_7 = 70\,°C$.

For comparison purposes, the values at $T_7 = 55\,°C$ for the non-etched Nafion 212 can be seen in Table 4.1 and for etched Nafion 212 in Table 4.2.
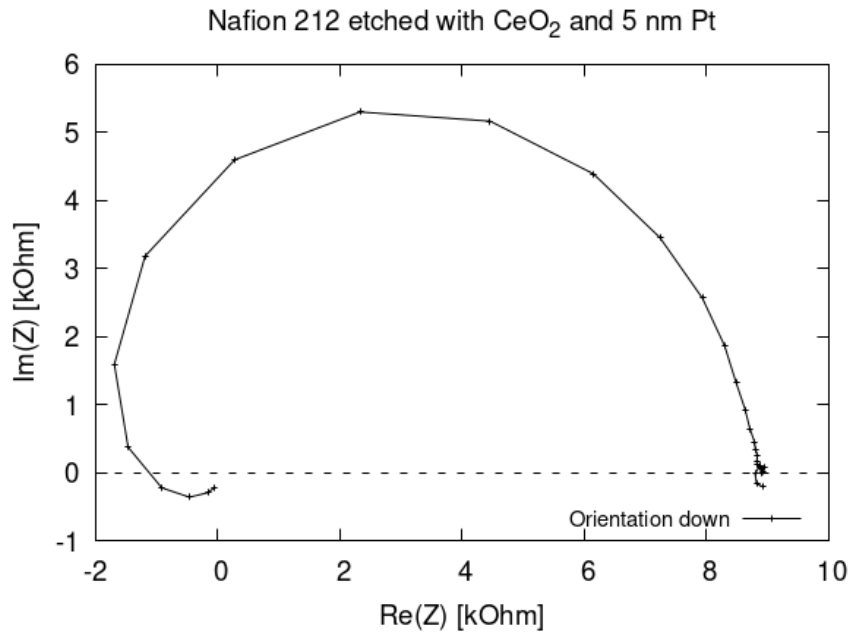
Figure 4.20: Our measurement of Nafion 212 etched with CeO_2 and $5\,nm$ Pt at $T = 70\,°C$.
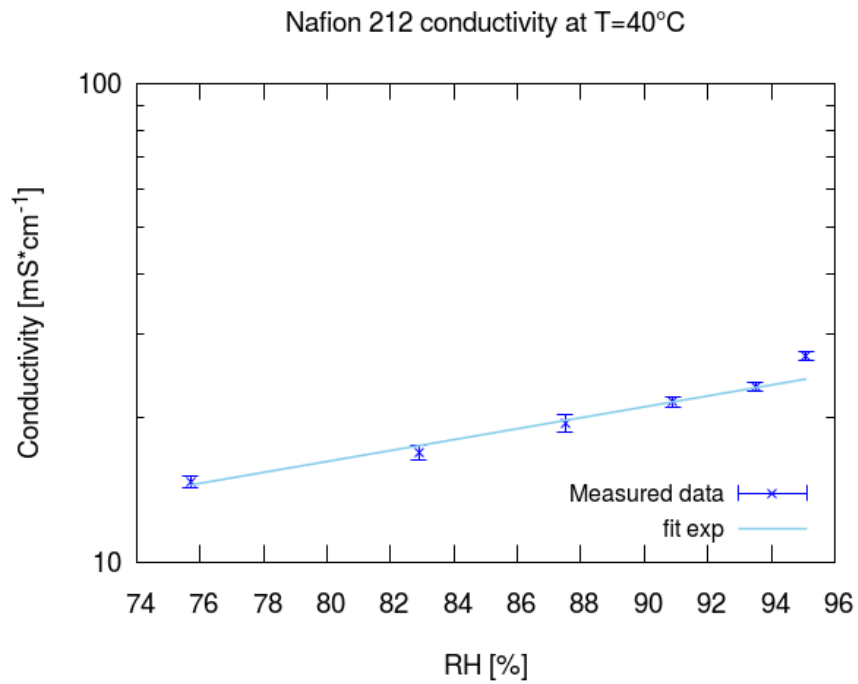
Figure 4.21: Our measurement of Nafion 212 at $T = 40\,°C$.
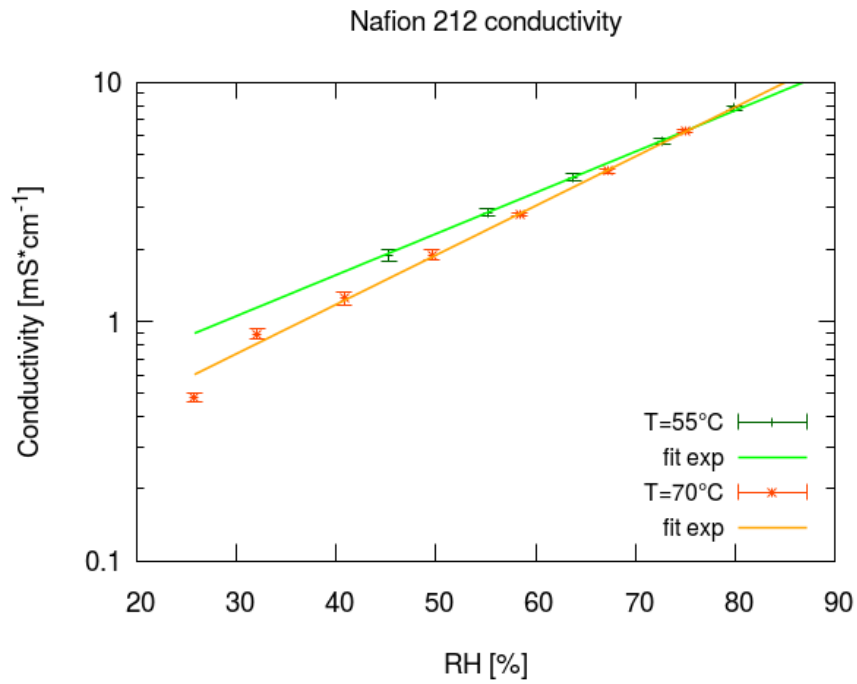
Figure 4.22: Our measurement of Nafion 212 at $T = 55\,°\text{C}$ and $T = 70\,°\text{C}$.
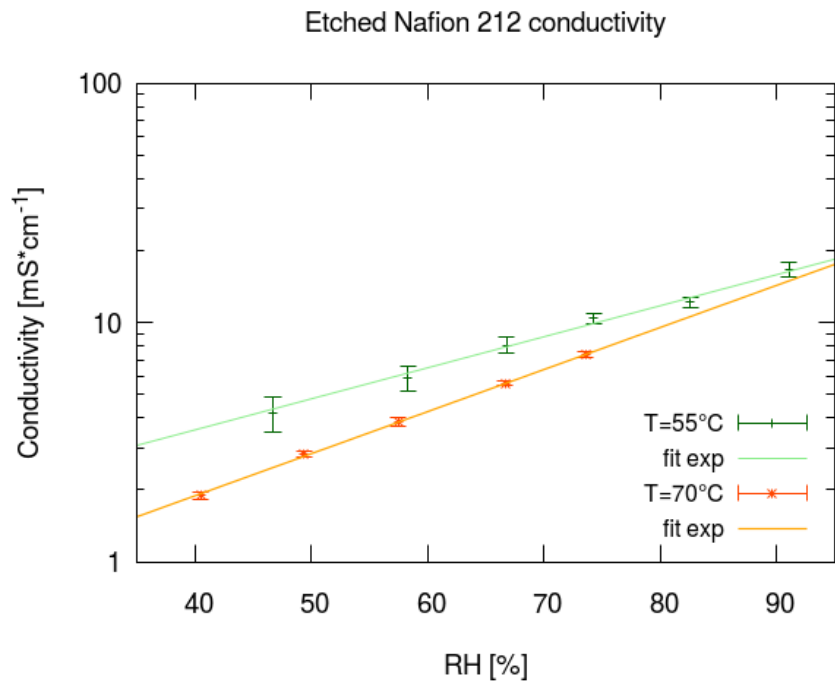
Figure 4.23: Our measurement of etched Nafion 212 at $T = 55\,°\text{C}$ and $T = 70\,°\text{C}$.
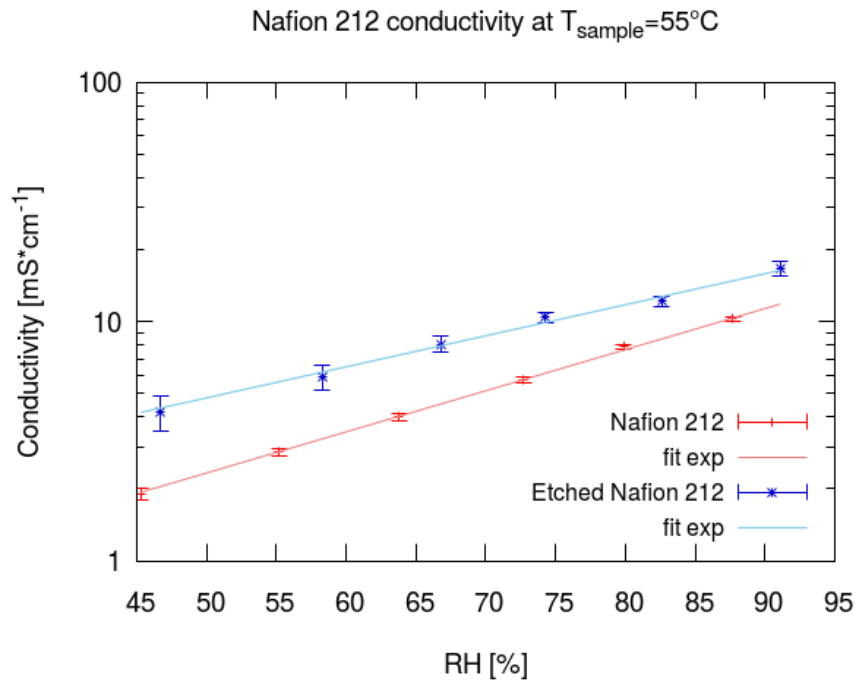
Figure 4.24: Comparison of Nafion 212 and etched Nafion at $T = 55\,°\text{C}$.
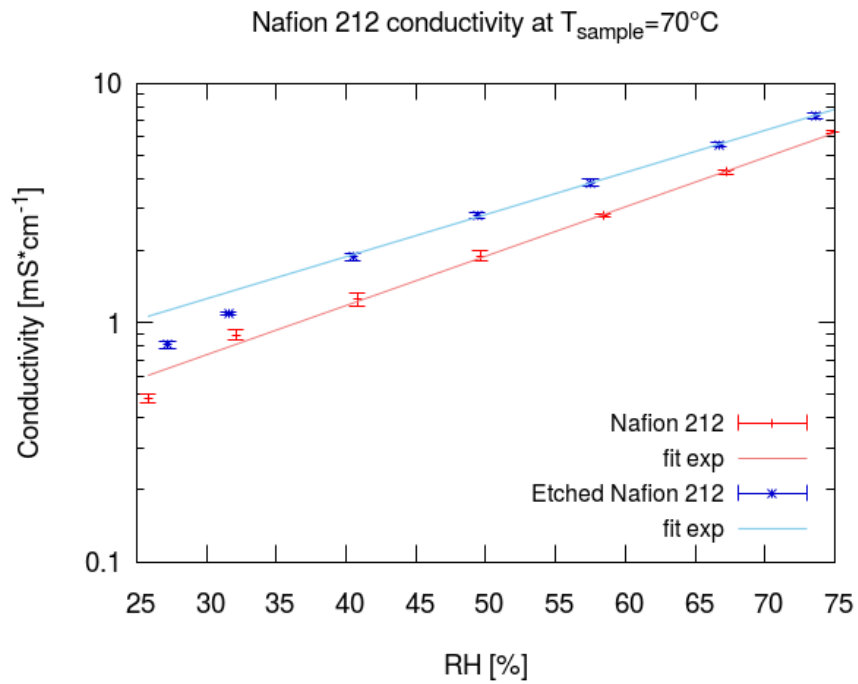
Figure 4.25: Comparison of Nafion 212 and etched Nafion at $T = 70\,°\text{C}$.

RH [%]	T_{bub} [K]	σ [mS cm^{-1}]	$\Delta\sigma$ [mS cm^{-1}]
45.3	40	1.90	0.09
55.2	45	2.86	0.10
63.8	50	4.00	0.08
72.7	55	5.71	0.08
79.9	60	7.84	0.15
87.7	65	10.26	0.13

Table 4.1: Conductivity of Nafion 212 at $T_{sample} = 55\,°C$.

RH [%]	T_{bub} [K]	σ [mS cm^{-1}]	$\Delta\sigma$ [mS cm^{-1}]
46.7	40	4.17	0.69
58.3	45	5.88	0.69
66.8	50	8.06	0.65
74.3	55	10.42	0.54
82.6	60	12.20	0.62
91.1	65	16.67	1.11

Table 4.2: Conductivity of etched Nafion 212 with CeO_2 and Pt at $T_{sample} = 55\,°C$.

4.7 Review

We can see from the figures comparing the performance of Nafion 212 and Nafion 212 etched with CeO_2 and $5\,nm$ Pt, that there is a significant difference in performance. The conductivity of etched Nafion 212 was roughly $1.9\times$ larger for $T_7 = 55\,°C$ and roughly $1.4\times$ larger for $T_7 = 70\,°C$. It is important to reiterate here the fact that the etched membrane could be measured only from the non-etched side, making this vast performance increase suspicious, as etched membrane usually have worse performance than their pristine counterparts. The thinning of these etched membranes has been approximated to be equal to $6\,\%$, which could not account for the performance increase.

The reason for these results is the degradation of the electrodes. The Nafion 212 measurements were done before these measurement of etched Nafion 212. Despite the use of new electrodes, the degradation took place after measuring the etched membranes, resulting in higher resistance when these electrodes were used to measure the pristine Nafion. There was a notable difference between measuring Nafion 212 before the electrode degradation and after the electrode degradation. The conductivity before was approximately $2.5\times$ larger than after electrode degradation, as measured from 5 values. The reason for low number of comparable measurements was that the measuring protocol was re-established after the measurement of etched membranes to accommodate for their behaviour. This difference was more remarkable for lower RH values. It is also important to note that there was no notable degradation of the electrodes when measuring pristine Nafion.

We can however see, that the slopes of the figures comparing pristine and etched Nafion 212 are comparable and their difference is also roughly comparable to that of the remeasuring of pristine Nafion 212. From these graphs we can

see that these values, if multiplied by the before mentioned factor of 2.5× would then make the values of etched and non-etched conductivity comparable. In order to draw any conclusion however, this would have to be investigated further in following works.

It is important to note, that the degradation of the electrodes took place only after measurement of etched membranes, indicating that etched membranes cause degradation of gold-plated copper alloy electrodes. The degradation after measuring Nafion etched in CeO_2 only was more drastic than after measuring Nafion etched in CeO_2 and sputtered with 5 nm Pt. If our theory about radicals created by etching being the reason behind the electrode degradation is true, then it could be that sputtering the surface with platinum leads to lower amount of surface active radicals.

This degradation of gold-plated electrodes has not yet been reported in detail in any articles we could find, except for Ramdutt et al. [2007] mentioning worsened EIS performance after measuring etched membranes. It is the conclusion of this chapter that gold plated copper alloy electrodes are not suitable for EIS measurement of etched Nafion membranes, with platinum probes being a better alternative.

5. Conclusion

In order to investigate performance of proton exchange membranes under well defined conditions, a humidity chamber electrochemical impedance spectroscopy measuring system was constructed. A novel sample holder design more suitable for future automation has been devised. The humidity chamber was able to achieve a wide range of temperature and RH levels, which were stable enough for precise EIS measurements. For futures improvement, smaller size of the chamber has been proposed to alleviate the problem of temperature gradient. Nafion 115 has been measured to test the system, showing good accordance with results found in literature. Overall the construction of the HCPEIS system has been successful, allowing for precise measurements of membranes.

Along with pristine Nafion membranes, membranes etched in CeO_2 atmosphere were measured. These membranes have been found to degrade the gold plated copper alloy electrodes. Such electrodes are usually used in EIS measurements and we have found no investigative study of this behaviour in literature. The degradation has been further investigated, showing stripping of the gold layer and subsequent creation of non-conductive copper oxides on the surface of the electrode in contact with the etched membrane. Only etched membranes have demonstrated this electrode degrading behaviour, which has been attributed to radicals created by surface etching of the membrane. Platinum electrodes may therefore be preferable for the measurements of etched membranes.

Bibliography

A. Ajanovic and R. Haas. Economic and environmental prospects for battery electric- and fuel cell vehicles: A review. *Fuel Cells*, 19(5):515–529, 2019. doi: 10.1002/fuce.201800171. URL https://onlinelibrary.wiley.com/doi/abs/10.1002/fuce.201800171.

Ghada Al-Madani, Mohammad H Kailani, and Mahmoud Al-hussein. Test System For Through-Plane Conductivity Measurements of Hydrogen Proton Exchange Membranes. 10:6465–6474, 2015.

J.M. Andújar and F. Segura. Fuel cells: History and updating. a walk along two centuries. *Renewable and Sustainable Energy Reviews*, 13(9):2309 – 2322, 2009. ISSN 1364-0321. doi: https://doi.org/10.1016/j.rser.2009.03.015. URL http://www.sciencedirect.com/science/article/pii/S1364032109001336.

Byungchan Bae, D.H Kim, Hyoung-Juhn Kim, Tae-Hoon Lim, In-Hwan Oh, and Heung Yong Ha. Surface characterization of argon-plasma-modified perfluorosulfonic acid membranes. *The journal of physical chemistry. B*, 110:4240–6, 04 2006. doi: 10.1021/jp055159i.

S.G.S. Beirão, Maria Lourenco, Fernando Santos, and Carlos Nieto de Castro. Thermal conductivity of humid air. *International Journal of Thermophysics*, 33, 09 2012. doi: 10.1007/s10765-012-1254-5.

Albert Bruix, Yaroslava Lykhach, Iva Matolínová, Armin Neitzel, Tomáš Skála, Nataliya Tsud, Mykhailo Vorokhta, Vitalii Stetsovych, Klára Ševčíková, Josef Mysliveček, Roman Fiala, Michal Václavů, Kevin C. Prince, Stéphanie Bruyère, Valérie Potin, Francesc Illas, Vladimír Matolín, Jörg Libuda, and Konstantin M. Neyman. Maximum noble-metal efficiency in catalytic materials: Atomically dispersed surface platinum. *Angewandte Chemie International Edition*, 53(39):10525–10530, 2014. doi: 10.1002/anie.201402342. URL https://onlinelibrary.wiley.com/doi/abs/10.1002/anie.201402342.

Arden L. Buck. New Equations for Computing Vapor Pressure and Enhancement Factor. *Journal of Applied Meteorology*, 20(12):1527–1532, December 1981. doi: 10.1175/1520-0450(1981)020⟨1527:NEFCVP⟩2.0.CO;2.

Jean-Marc Le Canut, Rami M. Abouatallah, and David A. Harrington. Detection of membrane drying, fuel cell flooding, and anode catalyst poisoning on PEMFC stacks by electrochemical impedance spectroscopy. *Journal of The Electrochemical Society*, 153(5):A857, 2006. doi: 10.1149/1.2179200. URL https://doi.org/10.1149%2F1.2179200.

Marcelo Carmo and Detlef Stolten. Chapter 4 - energy storage using hydrogen produced from excess renewable electricity: Power to hydrogen. In Paulo Emilio V. [de Miranda], editor, *Science and Engineering of Hydrogen-Based Energy Technologies*, pages 165 – 199. Academic Press, 2019. ISBN 978-0-12-814251-6. doi: https://doi.org/10.1016/B978-0-12-814251-6.00004-6. URL http://www.sciencedirect.com/science/article/pii/B9780128142516000046.

Kevin Cooper. Characterizing through-plane and in-plane ionic conductivity of polymer electrolyte membranes. *ECS Transactions*, 41, 01 2011. doi: 10.1149/1.3635668.

John Dalton. *Essay II. On the Force of Steam or Vapour from Water and Various other Liquids, both is a Vacuum and in Air.* Number v. 5, pt. 2. Literary and Philosophical Society of Manchester, 1802.

Michael A. Danzer and Eberhard P. Hofer. Analysis of the electrochemical behaviour of polymer electrolyte fuel cells using simple impedance models. *Journal of Power Sources*, 190(1):25 – 33, 2009. ISSN 0378-7753. doi: https://doi.org/10.1016/j.jpowsour.2008.10.003. URL `http://www.sciencedirect.com/science/article/pii/S0378775308019010`. Selected Papers presented at the 11th ULM ElectroChemical Days.

DuPont. Dupont™ nafion® pfsa membranes nr-211 and nr-212 datasheet. URL `https://www.fuelcellstore.com/spec-sheets/nafion-211-212-spec-sheet.pdf`.

Filip Dvořák, Matteo Camellone, Andrii Tovt, Nguyen-Dung Tran, Fabio Negreiros, Mykhailo Vorokhta, Tomáš Skála, Iva Matolínová, Josef Mysliveček, Vladimir Matolin, and Stefano Fabris. Creating single-atom pt-ceria catalysts by surface step decoration. *Nature Communications*, 7:10801, 02 2016. doi: 10.1038/ncomms10801.

M. Eikerling, A. A. Kornyshev, A. M. Kuznetsov, J. Ulstrup, and S. Walbran. Mechanisms of proton conductance in polymer electrolyte membranes. *Journal of Physical Chemistry B*, 105(17):3646–3662, 2002. ISSN 10895647. doi: 10.1021/jp003182s.

Natasha Erdman, David C. Bell, and Rudolf Reichelt. Scanning electron microscopy. In *Springer Handbook of Microscopy*, pages 2–2. Springer International Publishing, 2019. doi: 10.1007/978-3-030-00069-1_5. URL `https://doi.org/10.1007/978-3-030-00069-1_5`.

Shiyan Feng, Shoichi Kondo, Takahiro Kaseyama, Taichi Nakazawa, Takamasa Kikuchi, Roman Selyanchyn, Shigenori Fujikawa, Liana Christiani, Kazunari Sasaki, and Masamichi Nishihara. Characterization of polymer-polymer type charge-transfer (ct) blend membranes for fuel cell application. *Data in Brief*, 18, 02 2018. doi: 10.1016/j.dib.2018.02.031.

Philipp Frühwirt, Ambrož Kregar, Jens T. Törring, Tomaž Katrašnik, and Georg Gescheidt. Holistic approach to chemical degradation of nafion membranes in fuel cells: modelling and predictions. *Phys. Chem. Chem. Phys.*, 22:5647–5666, 2020. doi: 10.1039/C9CP04986J. URL `http://dx.doi.org/10.1039/C9CP04986J`.

I D Gimba, A S Abdulkareem, A Jimoh, and A S Afolabi. Theoretical Energy and Exergy Analyses of Proton Exchange Membrane Fuel Cell by Computer Simulation. *Journal of Applied Chemistry*, 2016:2684919, 2016. ISSN 2356-7171. doi: 10.1155/2016/2684919. URL `https://doi.org/10.1155/2016/2684919`.

Óscar González, T.J. Leo, and Emilio Navarro. Fuel cells: A real option for unmanned aerial vehicles propulsion. *TheScientificWorldJournal*, 2014:497642, 01 2014. doi: 10.1155/2014/497642.

Oliver Gröger, Hubert Gasteiger, and Peter Suchsland. Review—electromobility: Batteries or fuel cells? *Journal of The Electrochemical Society*, 162:A2605–A2622, 01 2015. doi: 10.1149/2.0211514jes.

P. Horowitz and W. Hill. *The Art of Electronics*. Cambridge University Press, 2015. ISBN 9780521809269. URL `https://books.google.cz/books?id=LAiWPwAACAAJ`.

G. James, D. Witten, T. Hastie, and R. Tibshirani. *An Introduction to Statistical Learning: with Applications in R*. Springer Texts in Statistics. Springer New York, 2013. ISBN 9781461471387. URL `https://books.google.cz/books?id=qcI_AAAAQBAJ`.

Pourak Kahroba, I Mirzaee, and Hassan Shirvani. The influence of membrane thickness on the pem fuel cell operation. 10 2009.

K D Kreuer. On the complexity of proton conduction phenomena K.D. Kreuer * Max-Planck-Institut fur Festkorperforschung, Heisenbergstr.1, D-70569 Stuttgart, Germany Abstract. *Solid State Ionics*, 137:1–12, 2000. ISSN 01672738. doi: 10.1016/S0167-2738(00)00301-5. URL `papers2://publication/uuid/02046F85-7C85-4FDC-A70E-FBEB9310D4A2`.

Klaus-Dieter Kreuer, Albrecht Rabenau, and Werner Weppner. Vehicle mechanism, a new model for the interpretation of the conductivity of fast proton conductors. *Angewandte Chemie International Edition in English*, 21(3):208–209, 1982. doi: 10.1002/anie.198202082. URL `https://onlinelibrary.wiley.com/doi/abs/10.1002/anie.198202082`.

Guangchun Li and Peter G. Pickup. Ionic conductivity of PEMFC electrodes. *Journal of The Electrochemical Society*, 150(11):C745, 2003. doi: 10.1149/1.1611493. URL `https://doi.org/10.1149%2F1.1611493`.

Junsheng Li, Xi Yang, Haolin Tang, and Mu Pan. Durable and high performance nafion membrane prepared through high-temperature annealing methodology. *Journal of Membrane Science*, 361(1):38 – 42, 2010. ISSN 0376-7388. doi: https://doi.org/10.1016/j.memsci.2010.06.016. URL `http://www.sciencedirect.com/science/article/pii/S0376738810004692`.

David R. Lide. *CRC Handbook of chemistry and physics*. CRC Press, 84th edition, 2003. ISBN 0849304849,9780849304842.

Lunyang Liu, Wenduo Chen, and Yunqi Li. An overview of the proton conductivity of nafion membranes through a statistical analysis. *Journal of Membrane Science*, 504:1 – 9, 2016. ISSN 0376-7388. doi: https://doi.org/10.1016/j.memsci.2015.12.065. URL `http://www.sciencedirect.com/science/article/pii/S0376738815304105`.

Wenming Liu, Yun Xie, Jianguo Liu, Xiao Jie, Jun Gu, and Zhigang Zou. Experimental study of proton exchange membrane fuel cells using nafion 212 and nafion 211 for portable application at ambient pressure and temperature conditions. *International Journal of Hydrogen Energy*, 37(5):4673 – 4677, 2012. ISSN 0360-3199. doi: https://doi.org/10.1016/j.ijhydene.2011.04.233. URL `http://www.sciencedirect.com/science/article/pii/S0360319911014182`. Portable Fuel Cells – Fundamental and Applications (ISPFC2010).

Shingjiang Jessie Lue, Shiang-Yiaw Hsiaw, and Ta-Chin Wei. Surface modification of perfluorosulfonic acid membranes with perfluoroheptane (c7f16)/argon plasma. *Journal of Membrane Science*, 305(1):226 – 237, 2007. ISSN 0376-7388. doi: https://doi.org/10.1016/j.memsci.2007.08.006. URL `http://www.sciencedirect.com/science/article/pii/S0376738807005492`.

Dzmitry Malevich, Ela Halliop, Brant Peppley, Jon Pharoah, and Kunal Karan. Effect of relative humidity on electrochemical active area and impedance response of PEM fuel cell. *ECS Transactions*, 16(2):1763–1774, dec 2019. doi: 10.1149/1.2982017. URL `https://doi.org/10.1149%2F1.2982017`.

Bruno R. Matos, Cleverson A. Goulart, Elisabete I. Santiago, R. Muccillo, and Fabio C. Fonseca. Proton conductivity of perfluorosulfonate ionomers at high temperature and high relative humidity. *Applied Physics Letters*, 104(9), 2014. ISSN 00036951. doi: 10.1063/1.4867351.

S.D. Mikhailenko, M.D. Guiver, and S. Kaliaguine. Measurements of pem conductivity by impedance spectroscopy. *Solid State Ionics*, 179(17):619 – 624, 2008. ISSN 0167-2738. doi: https://doi.org/10.1016/j.ssi.2008.04.020. URL `http://www.sciencedirect.com/science/article/pii/S0167273808003548`.

Vilem Nedela, Eva Tihlaříková, and Jiří Hřib. The low-temperature method for study of coniferous tissues in the environmental scanning electron microscope. *Microscopy Research and Technique*, 78, 01 2015. doi: 10.1002/jemt.22439.

Ryan O'Hayre, Suk-Won Cha, Whitney Colella, and Fritz B. Prinz. *Fuel Cell Fundamentals*. John Wiley & Sons, Inc, Hoboken, NJ, USA, may 2016. ISBN 9781119191766. doi: 10.1002/9781119191766. URL `http://doi.wiley.com/10.1002/9781119191766`.

Jennifer Peron, Ana Mani, Xinsheng Zhao, Dave Edwards, Makoto Adachi, Tatyana Soboleva, Ken Shi, Zhong Xie, Titichai Navessin, and Steven Holdcroft. Properties of nafion® nr-211 membranes for pemfcs. *Journal of Membrane Science*, 356:44–51, 07 2010. doi: 10.1016/j.memsci.2010.03.025.

Z Qi. *Proton Exchange Membrane Fuel Cells*. Electrochemical Energy Storage and Conversion. CRC Press, 2013. ISBN 9781466513716. URL `https://books.google.cz/books?id=iT{_}SBQAAQBAJ`.

Devin Ramdutt, Christine Charles, Jessica Hudspeth, Bradley Ladewig, Thomas Gengenbach, Rod Boswell, Andrew Dicks, and Pascal Brault. Low energy plasma treatment of nafion® membranes for pem fuel cells. *Journal of*

Power Sources, 165(1):41 – 48, 2007. ISSN 0378-7753. doi: https://doi.org/10.1016/j.jpowsour.2006.11.078. URL `http://www.sciencedirect.com/science/article/pii/S0378775306024256`.

H. Wayne Richardson. *Copper Compounds*. American Cancer Society, 2000. ISBN 9783527306732. doi: 10.1002/14356007.a07_567. URL `https://onlinelibrary.wiley.com/doi/abs/10.1002/14356007.a07_567`.

Rotronic. The rotronic humidity handbook, Dec 2005.

Wolfgang Schmittinger and Ardalan Vahidi. A review of the main parameters influencing long-term performance and durability of pem fuel cells. *Journal of Power Sources*, 180(1):1 – 14, 2008. ISSN 0378-7753. doi: https://doi.org/10.1016/j.jpowsour.2008.01.070. URL `http://www.sciencedirect.com/science/article/pii/S0378775308001924`.

M. Schulze, M. Lorenz, N. Wagner, and E. Gülzow. XPS analysis of the degradation of nafion. *Fresenius' Journal of Analytical Chemistry*, 365(1-3):106–113, September 1999. doi: 10.1007/s002160051454. URL `https://doi.org/10.1007/s002160051454`.

Shouwen Shi, Adam Weber, and Ahmet Kusoglu. Structure/property relationship of nafion xl composite membranes. *Journal of Membrane Science*, 516, 06 2016. doi: 10.1016/j.memsci.2016.06.004.

Yadunath Singh. Electrical resistivity measurements: A review. *International Journal of Modern Physics: Conference Series*, 22:745–756, 2013. doi: 10.1142/S2010194513010970. URL `https://doi.org/10.1142/S2010194513010970`.

F. M. Smits. Measurement of sheet resistivities with the four-point probe. *The Bell System Technical Journal*, 37(3):711–718, 1958.

Tatyana Soboleva, Zhong Xie, Zhiqing Shi, Emily Tsang, Titichai Navessin, and Steven Holdcroft. Investigation of the through-plane impedance technique for evaluation of anisotropy of proton conducting polymer membranes. *Journal of Electroanalytical Chemistry*, 622(2):145 – 152, 2008. ISSN 1572-6657. doi: https://doi.org/10.1016/j.jelechem.2008.05.017. URL `http://www.sciencedirect.com/science/article/pii/S0022072808002301`.

Yoshitsugu Sone. Proton conductivity of nafion 117 as measured by a four-electrode AC impedance method. *Journal of The Electrochemical Society*, 143(4):1254, 1996. doi: 10.1149/1.1836625. URL `https://doi.org/10.1149%2F1.1836625`.

Sune Thorsteinsson, Fei Wang, Dirch Petersen, Torben Hansen, Daniel Kjær, Rong Lin, Jang Kim, Peter Nielsen, and Ole Hansen. Accurate microfour-point probe sheet resistance measurements on small samples. *Review of Scientific Instruments*, 80:053902 – 053902, 06 2009. doi: 10.1063/1.3125050.

Zhi Qun Tian, San Hua Lim, Chee Kok Poh, Zhe Tang, Zetao Xia, Zhiqiang Luo, Pei Kang Shen, Daniel Chua, Yuan Ping Feng, Zexiang Shen, and Jianyi Lin. A highly order-structured membrane electrode assembly with vertically

aligned carbon nanotubes for ultra-low pt loading pem fuel cells. *Advanced Energy Materials*, 1(6):1205–1214, 2011. doi: 10.1002/aenm.201100371. URL `https://onlinelibrary.wiley.com/doi/abs/10.1002/aenm.201100371`.

Vaisala, 2019. URL `https://www.vaisala.com/sites/default/files/documents/HMT330-Series-Datasheet-B210951EN.pdf`.

Chenyi Wang, Dongwon Shin, So Lee, Na Kang, Gilles Robertson, Young Moo Lee, and Michael Guiver. A clustered sulfonated poly(ether sulfone) based on a new fluorene-based bisphenol monomer. *J. Mater. Chem.*, 22:25093–25101, 11 2012a. doi: 10.1039/C2JM34414A.

Haijiang Henry. Wang, Xiao-Zi. Yuan, and Hui Li. *PEM fuel cell durability handbook. PEM fuel cell diagnostic tools.* CRC Press/Taylor & Francis, 2012b. ISBN 9781439839218.

Liang Wang, Suresh G. Advani, and Ajay K. Prasad. Degradation reduction of polymer electrolyte membranes using ceo2 as a free-radical scavenger in catalyst layer. *Electrochimica Acta*, 109:775 – 780, 2013. ISSN 0013-4686. doi: https://doi.org/10.1016/j.electacta.2013.07.189. URL `http://www.sciencedirect.com/science/article/pii/S0013468613014746`.

W. Wang, X. Wei, D. Choi, X. Lu, G. Yang, and C. Sun. Chapter 1 - electrochemical cells for medium- and large-scale energy storage: fundamentals. In Chris Menictas, Maria Skyllas-Kazacos, and Tuti Mariana Lim, editors, *Advances in Batteries for Medium and Large-Scale Energy Storage*, Woodhead Publishing Series in Energy, pages 3 – 28. Woodhead Publishing, 2015. ISBN 978-1-78242-013-2. doi: https://doi.org/10.1016/B978-1-78242-013-2.00001-7. URL `http://www.sciencedirect.com/science/article/pii/B9781782420132000017`.

Dianne Wiley and Gustavo Fimbres Weihs. *Electroosmotic Drag in Membranes*, pages 1–3. Springer Berlin Heidelberg, Berlin, Heidelberg, 2015. ISBN 978-3-642-40872-4. doi: 10.1007/978-3-642-40872-4_2078-1. URL `https://doi.org/10.1007/978-3-642-40872-4_2078-1`.

Zhong Xie, Chaojie Song, Bernhard Andreaus, Titichai Navessin, Zhiqing Shi, Jiujun Zhang, and Steven Holdcroft. Discrepancies in the measurement of ionic conductivity of PEMs using two- and four-probe AC impedance spectroscopy. *Journal of The Electrochemical Society*, 153(10):E173, 2006. doi: 10.1149/1.2258091. URL `https://doi.org/10.1149%2F1.2258091`.

Rameshwar Yadav and Peter S. Fedkiw. Analysis of EIS technique and nafion 117 conductivity as a function of temperature and relative humidity. *Journal of the Electrochemical Society*, 159(3):340–346, 2012. ISSN 00134651. doi: 10.1149/2.104203jes.

Yurii Yakovlev, J. Nováková, Peter Kúš, T.N. Dinhová, Iva Matolínová, and Vladimir Matolin. Highly developed nanostructuring of polymer-electrolyte membrane supported catalysts for hydrogen fuel cell application. *Journal of Power Sources*, 439:227084, 11 2019. doi: 10.1016/j.jpowsour.2019.227084.

Xiao Zi Yuan, Chaojie Song, Haijiang Wang, and Jiujun Zhang. *Electrochemical impedance spectroscopy in PEM fuel cells: Fundamentals and applications.* Springer London, 2010. ISBN 9781848828452. doi: 10.1007/978-1-84882-846-9.

Zicheng Zuo, Yongzhu Fu, and Arumugam Manthiram. Novel blend membranes based on acid-base interactions for fuel cells. *Polymers*, 4(4):1627–1644, 2012. ISSN 20734360. doi: 10.3390/polym4041627.

List of Figures

List of Tables

List of Abbreviations

EDX . . . . energy-dispersive X-ray spectroscopy
EDL . . . . electric double layer
EW . . . . equivalent weight
EIS . . . . electrochemical impedance spectroscopy
GDL . . . . gas diffusion layer
HC . . . . humidity chamber
HCPEIS . . . . . . humidity   chamber   potentiostatic   electrochemical
            impedance spectroscopy
HC . . . . humidity chamber
HHV . . . . higher heating value
HOR . . . . hydrogen oxidation reaction
LHV . . . . lower heating value
MEA . . . . membrane electrode assembly
OCV . . . . open circuit voltage
ORR . . . . oxygen reduction reaction
PEM . . . . proton exchange membrane
PFSA . . . . perfluorosulfonic acid membranes
PID . . . . proportional–integral–derivative (regulator)
PEMFC . . . . . . proton exchange membrane fuel cell
RH . . . . relative humidity
SEM . . . . scanning electron microscopy